crystals

Crystal Structures of Compounds Containing Ions Selenite

Edited by
Claudia Graiff

Printed Edition of the Special Issue Published in *Crystals*

www.mdpi.com/journal/crystals

MDPI

Crystal Structures of Compounds Containing Ions Selenite

Crystal Structures of Compounds Containing Ions Selenite

Special Issue Editor

Claudia Graiff

MDPI • Basel • Beijing • Wuhan • Barcelona • Belgrade

Special Issue Editor
Claudia Graiff
Università di Parma
Italy

Editorial Office
MDPI
St. Alban-Anlage 66
4052 Basel, Switzerland

This is a reprint of articles from the Special Issue published online in the open access journal *Crystals* (ISSN 2073-4352) in 2018 (available at: https://www.mdpi.com/journal/crystals/special_issues/Ions_Selenite)

For citation purposes, cite each article independently as indicated on the article page online and as indicated below:

LastName, A.A.; LastName, B.B.; LastName, C.C. Article Title. *Journal Name* **Year**, *Article Number*, Page Range.

ISBN 978-3-03897-517-5 (Pbk)
ISBN 978-3-03897-518-2 (PDF)

Contents

About the Special Issue Editor

Claudia Graiff received her Ph.D. in Chemistry in 1998 (University of Parma, Italy). After several stays working with Prof. Carmona (Spain) and Prof. Braunstein (France) respectively, she obtained the position of Assistant Professor at the University of Parma in 1999. In 2004 she received the Bonati Junior prize for young researchers in organometallic chemistry. Since 2006 she has been a Professor of Chemistry at the Engineering Faculty of the University of Parma and in 2012 she obtained the National Scientific Qualification for Full Professors. She is the author of over 140 papers in international journals. She is a founding member of "HMI High materials innovation", a spin off company dealing with the development, control and sale of innovative materials and surface treatments. One of her main research fields is the systematic study of the crystal and molecular structure of compounds containing interesting building blocks able to form novel structural architectures. Moreover, her research activity deals with the synthesis and characterization of nanostructured functional materials, useful to preserve, strengthen and protect artifacts against biotic and abiotic degradation. These materials include (i) hybrid polyamido amines differently functionalized, (ii) Se-doped TiO_2 with enhanced photocatalytic activity, (iii) crystalline nanocellulose dispersed in water for the preservation and protection of lignocellulosic materials.

Preface to "Crystal Structures of Compounds Containing Ions Selenite"

The chemistry of materials containing Se oxyanions in the +4 oxidation state, such as selenite, hydrogenselenite, and oxoselenate, are of increasing interest in the research community for several reasons. First, the lone pair on the selenium atom can behave as structure-directing agent towards the formation of materials characterized by the presence of hollows or channels in their intimate structures, moreover, the weakly coordinative capability of the Se(IV) electron lone pairs could give rise to interesting supramolecular interactions, and finally, it is known that the incorporation of selenite anions can lead to non-centrosymmetric structures and, consequently, to materials displaying remarkable physicochemical properties.

The most important feature is that the full comprehension of the properties of this type of materials cannot be exhaustively understood unless the complete solid state crystal structure is available. In this Special Issue, entitled "Crystal Structures of Compounds Containing Ions Selenite", a series of new selenite-containing compounds synthesized by different methodologies and fully caracterized in the solid state is reported. Moreover the fundamental role of detailed structural analysis in understanding the interactions in the solid state that are responsible for the peculiar chemical–physical properties of such materials is discussed.

Claudia Graiff
Special Issue Editor

crystals

MDPI

Article

Mild Synthesis and Structural Characterization of a Novel Vanadyl Selenite-Hydrogen Selenite Phase, $Na[VO(SeO_3)(HSeO_3)]\cdot 1{,}5H_2O$

Stefano Canossa [1], Giovanni Predieri [1,2] and Claudia Graiff [1,2,*]

[1] Department of Chemistry, Life Sciences and Environmental Sustainability, University of Parma, Parco Area delle Scienze 17/A, 43124 Parma, Italy; stefano.canossa@studenti.unipr.it (S.C.); giovanni.predieri@unipr.it (G.P.)

[2] Consorzio Interuniversitario Reattività Chimica e Catalisi (C.I.R.C.C.), Via Celsio Ulpiani 27, 70126 Bari, Italy

* Correspondence: claudia.graiff@unipr.it; Tel.: +39-0521-905428

Received: 16 March 2018; Accepted: 13 May 2018; Published: 15 May 2018

Abstract: Single crystals of $Na[VO(SeO_3)(HSeO_3)]\cdot 1{,}5H_2O$ have been prepared by solvent slow evaporation from an equimolar aqueous mixture of sodium selenite and vanadyl sulfate. The overall arrangement consists of VO_6 octahedra, $[SeO_3]^{2-}$ and $[HSeO_3]^-$ anions forming a strong backbone with channel-like voids, while sodium cations participate in the framework, ensuring the overall charge balance. The crystal packing of the material features channels with a star-shaped section showing a mean aperture of 6.10 Å with the oxygen atoms of the V=O moieties pointing towards the interior of the cavities. Their dimensions are the narrowest reported until now in vanadium selenite compounds. Disordered sodium cations with occupancy factor of 0.5 are found in the star-shaped section cavities together with disordered water molecules, interacting with each other via hydrogen bonds.

Keywords: vanadyl selenite; vanadyl hydrogen selenite; crystal structure; crystal packing; layered structure; channels

1. Introduction

Compounds containing selenite or hydrogen selenite anions are of great interest within the scientific community, from synthetic, structural and chemical points of view.

The bridging properties of selenites for connecting to transition metal cations allow magnetic exchange between paramagnetic centers in oligonuclear transition metal selenite complexes [1]. Recently, the weakly coordinative capability of the Se(IV) electron lone pair has been found to give rise to supramolecular interactions, as observed for the polyoxoselenitepalladate anions $[Pd_{15}(\mu_3\text{-}SeO_3)_{10}(\mu_3\text{-}O)_{10}Na]^{9-}$ in the solid state [2]. Regarding the chemistry of extended solids, the stereochemically active lone pair of electrons in Se(IV) may cause the inorganic selenites to crystallize into non-centrosymmetric structures exhibiting interesting physical properties such as nonlinear optical second harmonic generation (SHG) [3,4]. Moreover, it has been observed that some selenites show a highly robust 3D open framework structure, which is retained upon the removal of guests or coordinated small molecules. Selenite and hydrogen selenite anions allow the formation of solid-state structures characterized by the presence of open channels and/or cavities able to house the selenium electron pair [5]. The porous structures of selenite derivatives open the possibility of using such compounds for the synthesis of Metal-Organic Frameworks (MOFs) or Porous Coordination Polymers (PCPs). The formation of either open-framework or non-centrosymmetric materials has been the focus of intense research for many years, since the combination of both an open-framework and non-centrosymmetry within a single compound is especially attractive. Templated vanadium

selenites are considered interesting systems owing to the presence of multiple asymmetric building units. This includes the possibility of using chiral organic amines, out-of-center octahedral distortions on vanadium cations, and stereoactive lone pairs on the Se(IV) centers [6–9].

Hydrothermal techniques have been applied to metal selenite systems in order to obtain different crystal phases [6,9]. These reaction conditions are especially attractive for exploratory work because they promote the growth of large single crystals and can be tuned to accommodate nearly any metal center [10]. Metal oxides have been widely used, owing to their structural diversity and technologically advantageous properties [11].

Pursuing our interest in the chemistry of selenite transition metal complexes to be used as precursor for the preparation of the corresponding metal selenides, we reacted sodium selenite with transition metal salts in water solution at room temperature. In the case of the reaction between vanadyl sulfate and sodium selenite in acidic conditions, we observed the formation of a microcrystalline powder. This was unambiguously identified as $Na[VO(SeO_3)(HSeO_3)]\cdot 1{,}5H_2O$. Its crystal structure is here discussed and compared with selenite and hydrogen selenite vanadyl phases reported in the literature.

2. Materials and Methods

2.1. General Techniques

All manipulations were carried out at room temperature in the air; vanadyl sulfate (97% purity), sodium selenite (98% purity), and solvents (Analytical Grade) were purchased and used as received (Aldrich, St. Louis, MO, USA). FTIR spectra (4000–400 cm^{-1}) were recorded on a Nicolet Nexus spectrophotometer equipped with a Smart Orbit HATR accessory (diamond).

2.2. X-ray Data Collection, Structure Solution, and Refinement

The intensity data of the compound were collected on a Bruker APEX II single crystal diffractometer [12,13] equipped with an area detector using a graphite monochromated Mo Kα radiation (λ = 0.71073 Å). Crystallographic and experimental details of the reported structure are summarized in Table 1. The structure was solved by direct methods and refined by full-matrix least-squares procedures (based on F_o^2) using SHELXL-2014/7 (version 2014/7) [14,15], first with isotropic thermal parameters and then with anisotropic thermal parameters in the last cycles of refinement for all the non-hydrogen atoms. The hydrogen atom of the hydrogen selenite anion was introduced into the geometrically calculated position. The sodium cation was found disordered in two positions with occupancy factor of 0.69 and 0.40 respectively. The structure has been deposited in the Inorganic Crystal Structure Database (ICSD) with CSD number 434385.

2.3. Preparation of $Na[VO(SeO_3)(HSeO_3)]\cdot 1{,}5H_2O$

A water solution (10 mL) of Na_2SeO_3 (0.706 g, 4.1 mmol) was prepared and acidified by adding an equimolar amount of a sulfuric acid solution (96%) [d = 1.84 g/mL]. A pale blue water solution (15 mL) containing $VOSO_4$ (0.665 g, 4.1 mmol) was added dropwise to the first solution at room temperature. The clear blue solution was stirred for 20 min. Then the solvent was left to evaporate, and small amount of deep green crystals suitable for X-ray analysis were obtained. FTIR (Diamond crystal HATR): ν (SeO_3^{2-}) = 693 cm^{-1}, ν (VO^{2+}) = 958 cm^{-1}.

Table 1. Summary of crystallographic data for $Na[VO(SeO_3)(HSeO_3)]\cdot 1{,}5H_2O$.

	$Na[VO(SeO_3)(HSeO_3)]\cdot 1{,}5H_2O$
Formula	$H_4NaO_{8,5}Se_2V$
FW	371.88
crystal system	Monoclinic
space group	$C2/c$
a, Å	18.5779(16)
b, Å	7.5662(7)
c, Å	12.5844(11)
β, deg	111.612(1)
V, Å^3	1644.6(3)
Z	8
T(K)	298
D_{calcd}, g cm^{-3}	3.004
$F(000)$	1352.0
μ, cm^{-1}	10.125
rflns collected	9710
rflns unique	1697
rflns observed [$I > 2\sigma(I)$]	1365 [$R_{int} = 0.0618$]
Parameters	134
R indices [$I > 2\sigma(I)$]	$R1 = 0.0382$; $wR2 = 0.1001$
R indices (all data)	$R1 = 0.0504$; $wR2 = 0.1064$

$R1 = \Sigma\,||F_o| - |F_c||/\Sigma|F_o|$. $wR2 = [\Sigma[w(F_o^2 - F_c^2)^2]/\Sigma[w(F_o^2)^2]]$.

3. Results and Discussion

3.1. Chemistry and Crystal Growth

The exchange reaction between Na_2SeO_3 and $VOSO_4$ salts in water solution and at room temperature led to the formation of a vanadyl selenite hydrogen selenite phase, whose crystalline structure was fully elucidated by means of X-ray diffraction analysis on suitable single crystals obtained by slow evaporation of the solvent. A relatively small number of vanadium selenite compounds with analogous arrangement are present in the literature, although their syntheses have been carried out in hydrothermal conditions. In the phase here reported, the overall charge balance of the extended $[VO(SeO_3)(HSeO_3)]$ network is ensured by sodium cations. According to the study by Olshansky et al., the acidic pH environment is necessary for the attainment of similar phases, and this can be extended also to the present case [16]. The overall chemical reaction equation is reported in Scheme 1.

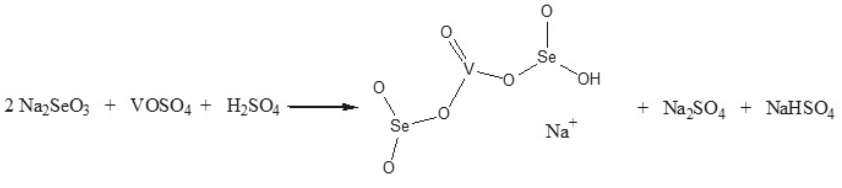

Scheme 1. Chemical reaction equation.

3.2. Crystal Structure Description

The asymmetric unit of $Na[VO(SeO_3)(HSeO_3)]\cdot 1{,}5H_2O$ consists of 11 non-hydrogen atoms, among them one vanadium and two crystallographically independent Se atoms, namely Se1 and Se2, as shown in Figure 1. A list of the most important bond distances and angles is reported in the caption of the figure. A sodium atom is also present, disordered in two positions (Na1 and Na2) with occupancy factor of 0.5.

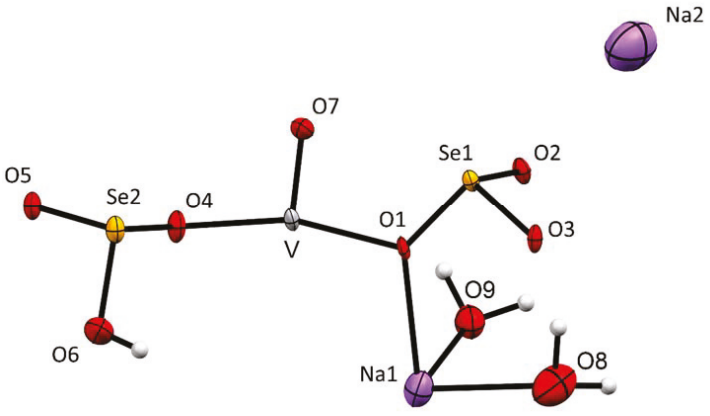

Figure 1. ORTEP view of the asymmetric unit of $Na[VO(SeO_3)(HSeO_3)]\cdot 1{,}5H_2O$. Ellipsoids are depicted at their 30% probability level. List of the most important bond distances [Å] and angles [deg]: Se1-O1 1.712(4), Se1-O3 1.698(4), Se1-O2 1.695(4), Se2-O5 1.656(4), Se2-O4 1.687(4), Se2-O6 1.7560(7), V-O1 1.993(4), V-O4 1.990(5), V-O7 1.596(5); O3-Se1-O1 99.3(2), O2-Se1-O1 100.5(2), O2-Se1-O3 97.6(2), O5-Se2-O4 100.5(2), O5-Se2-O6 97.08(17), O4-Se2-O6 98.83(19), O4-V-O1 162.2(2), O7-V-O1 97.2(2), O7V-O4 100.5(2), Se1-O1-V 120.4(2), Se2-O4-V 123.9(3).

The vanadium atom lies in a distorted octahedral environment with six oxygen atoms: the terminal V=O, two make V-O-Se2 linkages, and the remaining three form V-O-Se1 linkages. The short V=O distance of 1.596(5) Å and the V-O bond distances ranging from 1.982(4) to 2.209(5) Å are in agreement with the mean values observed in similar moieties reported in the Crystallographic Data Bank [17]. In particular, as reported in Figure 2, the distorted octahedron presents the shortest and the longest V-O distances in *trans* to one another, with the remaining four V-O bond lengths on the equatorial plane. Moreover, the vanadium atom is out of the mean plane defined by the equatorial bonded oxygen atoms of 0.297(5) Å.

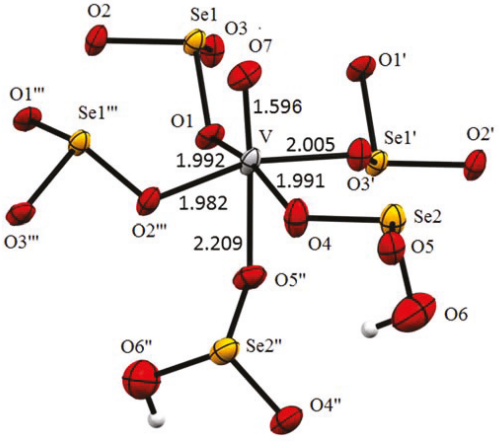

Figure 2. ORTEP diagram of the distorted vanadium octahedron, bond distances are reported in Å. Ellipsoids are depicted at their 30% probability level. Symmetry codes for atoms: ' = 2 − x, 2 − y, 1 − z; '' = 2.5 − x, −0.5 + y, 1.5 − z; ''' = 2 − x, y, 1.5 − z.

The two Se atoms exhibit a trigonal pyramidal geometry with a stereoactive lone pair. The three oxygen atoms around Se1 are connected to the neighboring VO_6 octahedra with bond angles of 120.4(2), 120.3(2) and 122.7(3)° (mean value 121.1(2)°). The selenium lone pair occupies the tetrahedral site. In the case of Se2; however, only two of the oxygen atoms form such linkages, while the third is protonated. The V-O-Se2 bond angles involving the non-protonated oxygen atom are 115.8(2) and 123.9(2)°. The presence of a longer Se2-O6 bond distance of 1.756(1) Å and the absence of interactions of this oxygen with the vanadium atom are coherent the presence of a terminal OH group.

3.3. Analysis of Molecular Packing

The overall framework structure of the compound is built up of VO_6, SeO_3, and $HSeO_3$ units. All three oxygen atoms of SeO_3 are shared by three neighboring vanadium-oxygen octahedra in such a manner as to form a ladder developing along the *c*-axis, consisting of edge-shared eight membered rings, each ring composed of two Se and two V atoms and four bridging oxygen atoms, as shown in Figure 3.

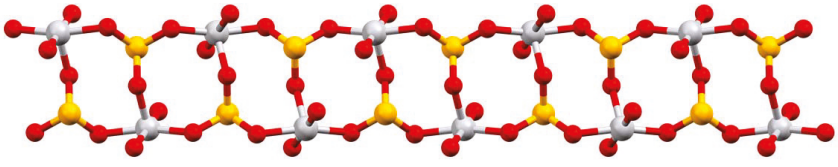

Figure 3. Partial framework structure of $Na[VO(SeO_3)(HSeO_3)]\cdot 1{,}5H_2O$ evidencing the formation of a ladder developing along the *c*-axis consisting of edge-shared eight membered rings.

These ladders are connected to one another by $HSeO_3$ groups along the *a*-axis to form a layer in the *ac*-plane as shown in Figure 4. This connectivity leads to the formation of a sixteen-membered bifurcated aperture with the dimensions 8.664 Å and 9.058 Å (vanadium to vanadium distance). The Se-O-H pendant moiety dandling above and below the aperture.

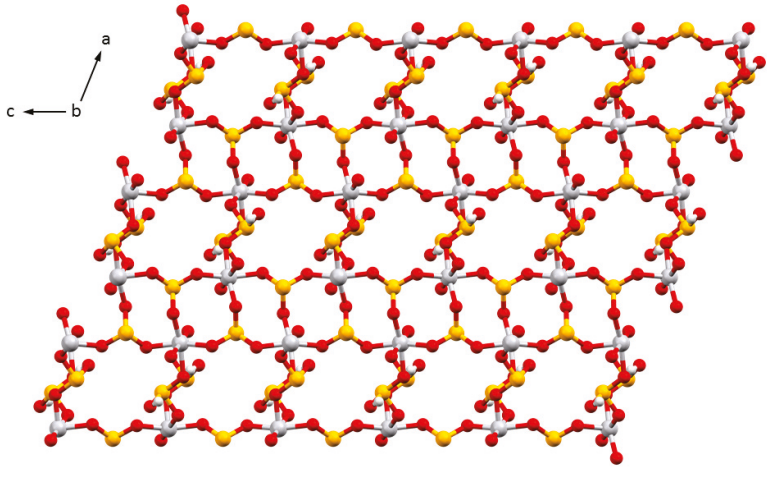

Figure 4. Extension of the ladders in $Na[VO(SeO_3)(HSeO_3)]\cdot 1{,}5H_2O$ along the *a*-axis to form a layer in the *ac*-plane. Sodium atoms and water molecules have been omitted for clarity.

3.4. Crystal Packing of Disordered Na^+ Cation in the Channels

The chain and layer motif observed in compound $Na[VO(SeO_3)(HSeO_3)]\cdot 1{,}5H_2O$ is similar to that in earlier reported vanadium selenite compounds organically templated with nitrogen containing cations and is considered to be a building unit in the vanadium selenite, whose progressive building up process, from the one-dimensional structure to two and three-dimensional complex structures has been demonstrated [6,9].

Viewing the crystal packing along the *c*-axis, as depicted in Figure 5, it is evident to observe the formation of channels with a star-shaped section with a mean aperture of 6.10 Å (O to O distance), with the oxygen atoms of the V=O moieties pointing towards the interior of the cavities.

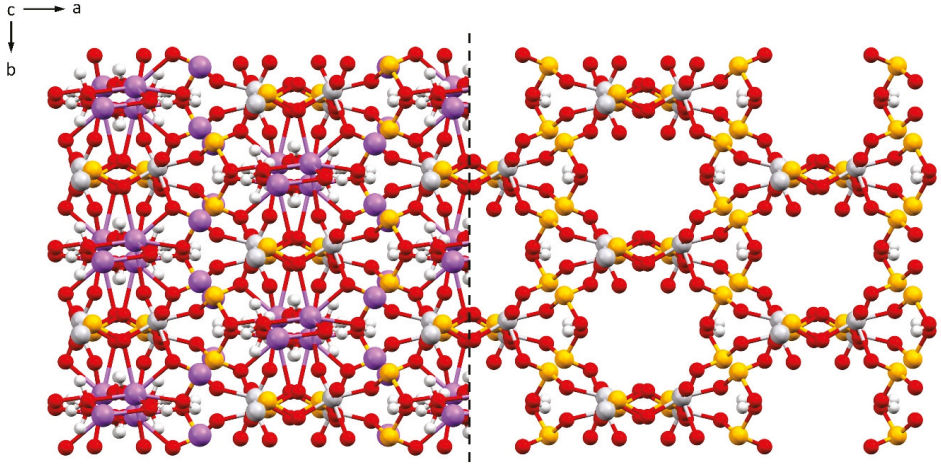

Figure 5. Crystal packing viewed along the *c*-axis, evidencing the formation of channels with a star-shaped section in which disordered Na^+ cations (purple) and water molecules can insert.

Both the V and Se atoms are in the +4 oxidation state, so that the framework charge is −1, $[(VO)(HSeO_3)(SeO_3)]^-$ balanced by metal cations. In fact, disordered sodium cations are found in the star-shaped section cavities (Figure 5) together with water molecules, interacting each other via hydrogen bonds.

As far as the 16-member star-shaped apertures are concerned, similar types of channels are also observed in reported vanadium selenite compounds organically templated with nitrogen-containing cations [7–9,16].

The mean dimension of the diameter of the cavities can vary depending on the size of the cationic moiety located into the channel and the presence of crystallization solvent molecules. Figure 6 shows the crystal packing of structures containing vanadium selenite hydrogen selenite compounds reported in the literature, in which channels developing along one of the crystallographic axes are present.

The dimensions of the mean diameter of the channels are reported in Table 2. All deposited structures present a dimension greater than the one observed in the case of $Na[VO(SeO_3)(HSeO_3)]\cdot 1{,}5H_2O$. This is due to the greater hindrance of the nitrogen-containing organic cations—sometimes cocrystallized together with solvent molecules—with respect to the dimension of the sodium atom. Moreover, the nitrogen-containing cations inserted into the channels reported in the literature are involved in a strong network of hydrogen bonds with the oxygen atoms of the selenite or hydrogen selenite anions.

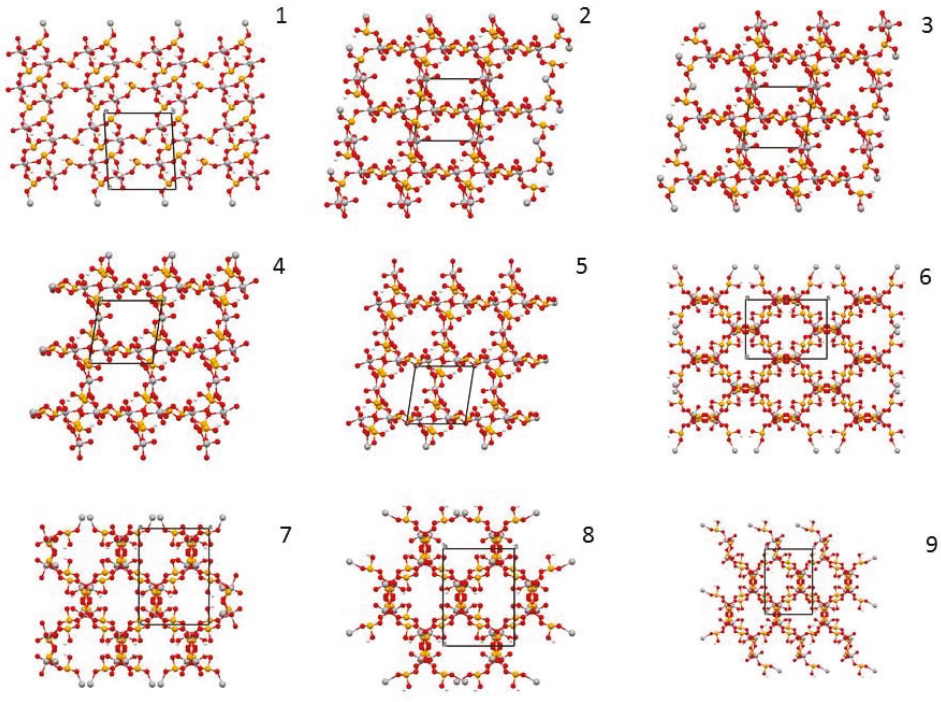

Figure 6. Channels developing in the crystal packing of reported vanadium selenite compounds organically templated with nitrogen containing cations.

Table 2. Mean diameter [Å] of the cavities found in the literature compared with the one observed in $Na[VO(SeO_3)(HSeO_3)]\cdot 1{,}5H_2O$.

$Na[VO(SeO_3)(HSeO_3)]\cdot 1{,}5H_2O$	1	2	3	4	5	6	7	8	9
6.10	6.50 [9]	7.83 [16]	7.38 [16]	7.89 [16]	7.95 [16]	7.83 [7]	8.27 [7]	7.57 [7]	6.40 [7]

In the crystallographic data bank of inorganic compounds, the crystal structures of the $K[VO(SeO_3)(HSeO_3)]$ [18] and of $NH_4[VO(SeO_3)(HSeO_3)]$ [19] are described. In those cases, the crystal structure and the morphology, shape and dimensions of the channels are very different from those of the presented phase. In fact, in both potassium and ammonium containing structures, very similar to one another, the overall crystal packing is composed of chains built up by VO_5 square pyramids pointing up and down alternatingly with respect to the direction of the chains and SeO_3 trigonal pyramid units. These chains are connected to one another by very strong hydrogen bonds. Moreover, each VO_5 interacts with adjacent VO_5 through the long V···O interaction. In the crystal packing of $[NH_4][H(VO)(SeO_3)_2]$ and $[K][H(VO)(SeO_3)_2]$, narrow channels with an average diameter of 4.35 Å are formed, and the potassium atom or NH_4^+ cations, with analogous steric hindrance, can insert. Both cations strongly interact with the oxygen atoms of the selenite and hydrogen selenite anions by hydrogen bonds.

4. Conclusions

Carrying out a reaction between vanadyl sulfate and sodium selenite with a water solvent at room temperature and under acidic conditions, a novel selenite hydrogen selenite phase was formed. The formula is $Na[VO(SeO_3)(HSeO_3)]\cdot 1{,}5H_2O$, and its structure is composed of chain and

layer crystallographic motifs, similar to those observed in previously reported vanadium selenite compounds organically templated with nitrogen-containing cations. The crystal packing of the material features channels with a star-shaped section with a mean aperture of 6.10 Å. The dimension of the cavities is, to our knowledge, the narrowest that has been reported until now for vanadium selenite compounds. Other selenite phases containing simple inorganic cations have been reported in the literature, such as with potassium or ammonium. In the present case, the overall crystal network is more similar to the one observed in reported organically templated vanadium selenite compounds than to the potassium- or ammonium-containing selenite structures. We suggest that the dimensions of the sodium cations, which are remarkably smaller than those of ammonium or potassium cations, makes it possible to keep the formation of main channels, as observed in reported vanadium selenite compounds, available to host disordered sodium cations together with disordered solvent molecules. This size effect can be exploited to obtain open framework compounds, where the structural presence of the cations does not prevent the accessibility of the cavities.

Author Contributions: S.C., G.P. and C.G. contributed equally to the research and writing of the present paper.

Acknowledgments: University of Parma is gratefully acknowledged for financial support.

Conflicts of Interest: The authors declare no conflict of interest.

References

1. Delferro, M.; Graiff, C.; Marchiò, L.; Elviri, L.; Mazzani, M.; Riccò, M.; Predieri, G. Synthesis, Structural characterization, and magnetic properties of the heteroleptic dinuclear nickel selenite complex [{Ni(TMEDA)SeO_3}$_2$]. *Eur. J. Inorg. Chem.* **2011**, 3327–3333. [CrossRef]
2. Delferro, M.; Graiff, C.; Elviri, L.; Predieri, G. Self-assembly of polyoxoselenitopalladate nanostars [$Pd_{15}(\mu_3$-$SeO_3)_{10}(\mu_3$-$O)_{10}Na]^{9-}$ and their supramolecular pairing in the solid state. *Dalton Trans.* **2010**, *39*, 4479–4481. [CrossRef] [PubMed]
3. Ok, K.-M.; Halasyamani, P.S. Asymmetric cationic coordination environments in new oxide materials: Synthesis and characterization of $Pb_4Te_6M_{10}O_{41}$ (M = Nb^{5+} or Ta^{5+}). *Inorg. Chem.* **2004**, *43*, 4248–4253. [CrossRef] [PubMed]
4. Halasyamani, P.S.; Poeppelmier, K.R. Noncentrosymmetric Oxides. *Chem. Mater.* **1998**, *10*, 2753–2769. [CrossRef]
5. Wontcheu, J.; Schleid, T. $Tb_3O_2Cl[SeO_3]_2$ and $Tb_5O_4Cl_3[SeO_3]_2$: Oxide Chloride Oxoselenates(IV) of Trivalent terbium with "lone-pair" channel or layer structures. *Z. Anorg. Allg. Chem.* **2005**, *631*, 309–315. [CrossRef]
6. Dai, Z.; Shi, A.; Li, G.; Chen, X.; Lu, X.; Xu, Y.; Feng, S. Hydrothermal syntheses and structures of two novel vanadium selenites, {[VO(OH)(H_2O)](SeO_3)}$_4$·2H_2O and ($H_3NCH_2CH_2NH_3$)[(VO)(SeO_3)$_2$]. *J. Solid State Chem.* **2003**, *172*, 205–211. [CrossRef]
7. Olshansky, J.H.; Tran, T.T.; Hernandez, K.J.; Zeller, M.; Shiv Halasyamani, P.; Schrier, J.; Norquist, A.J. Role of hydrogen-bonding in the formation of polar achiral and nonpolar chiral vanadium selenite frameworks. *Inorg. Chem.* **2012**, *51*, 11040–11048. [CrossRef] [PubMed]
8. Pasha, I.; Choudhury, A.; Rao, C.N.R. Organically templated vanadyl selenites with layered structures. *Inorg. Chem.* **2003**, *42*, 409–415. [CrossRef] [PubMed]
9. Dai, Z.; Li, G.; Shi, Z.; Liu, X.; Feng, S. Hydrothermal synthesis and structural characterization of a new layered vanadium selenite: ($C_4N_2H_{12}$)$_{0.5}$[(VO)$_2$(H_2O)$_2$(SeO_3)$_2$($HSeO_3$)]. *Inorg. Chem. Commun.* **2005**, *8*, 890–893. [CrossRef]
10. Rabenau, A. The role of hydrothermal synthesis in preparative chemistry. *Angew. Chem. Int. Ed. Engl.* **1985**, *24*, 1026–1040. [CrossRef]
11. Rao, C.N.R.; Behera, J.N.; Dan, M. Organically-templated metal sulfates, selenites and selenates. *Chem. Soc. Rev.* **2006**, *35*, 375–387. [CrossRef] [PubMed]
12. Bruker-Nonius. *SAINT, Version 7.06a*; Bruker AXS Inc.: Madison, WI, USA, 2004.
13. Sheldrick, G.M. *SADABS—Bruker Nonius Area Detector Scaling and Absorption Correction—V2016/2*; Bruker AXS Inc.: Madison, WI, USA, 2016.
14. Sheldrick, G.M. *SHELX97, Version Release 97–2*; University of Göttingen: Göttingen, Germany, 1998.

15. Sheldrick, G.M. A short history of SHELX. *Acta Cryst.* **2008**, *64*, 112–122. [CrossRef] [PubMed]
16. Olshansky, J.H.; Wiener, K.J.; Smith, M.D.; Nourmahnad, A.; Charles, M.J.; Zeller, M.; Schrier, J.; Norquist, A.J. Formation principles for vanadium selenites: The role of pH on product composition. *Inorg. Chem.* **2014**, *53*, 12027–12035. [CrossRef] [PubMed]
17. Halasyamani, P.S.; O'Hare, D. A new three-dimensional vanadium selenite, $(VO)_2(SeO_3)_3$, with isolated and edge-shared VO_6 octahedra. *Inorg. Chem.* **1997**, *36*, 6409–6412. [CrossRef]
18. Kim, Y.H.; Lee, K.-S.; Kwon, Y.-U.; Han, O.H. $K(VO)(SeO_3)_2H$: A new one-dimensional compound with strong hydrogen bonding. *Inorg. Chem.* **1996**, *35*, 7394–7398. [CrossRef] [PubMed]
19. Emirdag-Eanes, M.; Ibers, J.A. Synthesis and characterization of two vanadium chalcogenides, $[NH_4][H(VO)(SeO_3)_2]$ and $Cs_4[(VOS_2)_2(\mu\text{-}O)]$, prepared solvothermally. *J. Alloys Compd.* **2003**, *361*, 66–70. [CrossRef]

crystals

MDPI

Article

Se–Cl Interactions in Selenite Chlorides: A Theoretical Study

Sergey V. Krivovichev [1,2,*] and Liudmila A. Gorelova [2]

[1] Nanomaterials Research Centre, Kola Science Centre, Russian Academy of Sciences, Fersman str. 14, 184209 Apatity, Russia

[2] Department of Crystallography, Institute of Earth Sciences, St. Petersburg State University, University Emb. 7/9, 199034 St. Petersburg, Russia; gorelova.ljudmila@gmail.com

* Correspondence: s.krivovichev@spbu.ru; Tel.: +7-81555-75-350

Received: 29 March 2018; Accepted: 25 April 2018; Published: 29 April 2018

Abstract: The Se–Cl interactions in five selenite chlorides (α,β-$Zn_2(SeO_3)Cl_2$ (sofiite and its polymorph), α,β-$Cu_5O_2(SeO_3)_2Cl_2$ (georgbokiite and parageorgbokiite), and $KCdCu_7O_2(SeO_3)_2Cl_9$ (burnsite)) have been investigated by means of the analysis of their theoretical electron density distributions. The analysis reveals the existence in the structures of two basic types of interactions: intermediate interactions with essential covalent contribution and closed-shell interactions. In $Zn_2(SeO_3)Cl_2$ polymorphs and burnsite, all metal-oxide and metal-chloride interactions are of the first type, whereas in georgbokiite and parageorgbokiite, the Jahn–Teller distortion results in the elongation of some of the Cu–*X* bonds and their transition to the closed-shell type. All anion–anion interactions are of the closed-shell type. The energy of the closed-shell Se–Cl interactions can be estimated as 1.4–2.6 kcal·mol^{-1}, which is comparable to weak hydrogen bonds. Despite their weakness, these interactions provide additional stabilization of structural architectures. The Se^{4+}–Cl^- configurations are localized inside framework channels or cavities, which can be therefore be viewed as regions of weak and soft interactions in the structure.

Keywords: selenite; chloride; crystal structure; copper; zinc; electron density; closed-shell interactions; halogen bond; sophiite; georgbokiite

1. Introduction

According to the last version of the Inorganic Crystal Structure Database (ICSD) [1], there are about 130 structurally characterized inorganic compounds containing Se, O, and Cl, and more than 95 of them are selenite chlorides, i.e., the compounds containing both $(Se^{4+}O_3)^{2-}$ and Cl^- anions. No selenate chlorides have been reported in the literature to the present date. The high affinity of selenite and chloride anions is obvious and requires a chemically reasonable explanation. The problem is also important from the viewpoint of interesting physical properties of transitional metal selenite chlorides [1–11] and their mineralogical occurrences [12–23]. Indeed, many transitional metal selenite chlorides display diverse magnetic properties, due to the presence in their structures of low-dimensional arrays of magnetic ions such as Cu^{2+}, Ni^{2+}, Co^{2+}, and Fe^{2+} [11]. The eruption of Tolbachik volcano (Kamchatka peninsula, Russia) in 1975–1976 was followed by the extensive fumarolic activity, which was accompanied, in particular, by the formation of selenite chloride mineral associations dominated by Cu^{2+}-containing species [12,14–16,18–20,22,23].

Johnsson et al. [24] noted that the tendency of lone-electron pair cations such as Se^{4+} and Te^{4+} to associate with halide ions results in the agglomeration of halides and lone pairs into separate regions in the crystal structure, which act as 'chemical scissors', subdiving the structure space into relatively hard and covalently bonded metal-oxide parts and relatively soft halide-lone-pair parts. However, the chemical nature of the halide-lone-pair association remained unclear. The aim of the present paper

is to investigate interactions between Se^{4+} and Cl^{-} ions in selenite chlorides from a theoretical point of view, using the 'Atoms-in-Molecules' (AIM) theory [25] in order to shed some light on the existence of these compounds and their abundance compared to selenate chlorides.

2. Materials and Methods

According to this approach, the presence of a (3, −1) bond critical point (bcp) along the interatomic line (bond path) in the electron-density distribution, $\rho(\mathbf{r})$, unambiguously manifests the existence of a bonding interaction between the respective pair of atoms. The properties of the bcps provide a unique set of descriptors that can be used to understand the nature of interatomic interactions [26]. In particular, the following parameters are of importance: (1) electron density at the bcp, $\rho(\mathbf{r_c})$ (here and in the following $\mathbf{r_c}$ is a radius vector of the bcp); (2) Laplacian of the electron density, $\nabla^2\rho(\mathbf{r_c})$; (3) electron energy density, $H(\mathbf{r_c})$, which is defined as a sum $[G(\mathbf{r_c}) + V(\mathbf{r_c})]$ of kinetic ($G(\mathbf{r_c})$) and potential ($V(\mathbf{r_c})$) energy densities. All chemical interactions can be classified into different groups according to the values of these or derivative parameters. Herein we adopt the classification proposed by Espinosa et al. [27], which is based on the signs of the $\nabla^2\rho(\mathbf{r_c})$ and $H(\mathbf{r_c})$ parameters. According to this approach, chemical interactions can be classified as: (1) shared interactions with $\nabla^2\rho(\mathbf{r_c}) < 0$ and $H(\mathbf{r_c}) < 0$; (2) closed-shell interactions with $\nabla^2\rho(\mathbf{r_c}) > 0$ and $H(\mathbf{r_c}) > 0$; (3) intermediate or transit interactions with $\nabla^2\rho(\mathbf{r_c}) > 0$ and $H(\mathbf{r_c}) < 0$. It should be noted, however, that this classification was originally suggested for F ··· H interactions, and its transfer to other interactions is rather conditional.

The laplacian is related to the electron energy densities through the following equation:

$$\nabla^2\rho(\mathbf{r_c}) = 4\,[2G(\mathbf{r_c}) + V(\mathbf{r_c})], \quad (1)$$

which means that $\nabla^2\rho(\mathbf{r_c}) < 0$ only if $|V(\mathbf{r_c})|/G(\mathbf{r_c}) > 2$, since $G(\mathbf{r_c})$ is always positive, whereas $V(\mathbf{r_c})$ is always negative. Consequently, $|V(\mathbf{r_c})|/G(\mathbf{r_c}) > 2$ for shared interactions, $2 > |V(\mathbf{r_c})|/G(\mathbf{r_c}) > 1$ for intermediate interactions, and $|V(\mathbf{r_c})|/G(\mathbf{r_c}) < 1$ for closed-shell interactions.

Espinosa et al. [27] and Gatti [26] proposed to use the $H(\mathbf{r_c})/\rho(\mathbf{r_c})$ parameter or bond degree (BD) to measure the degree of covalency of a particular interaction. The lower the BD value, the higher is the covalency of an interaction. The BD value is negative for shared and intermediate interactions and positive for closed-shell interactions.

It has long been recognized that in some ionic crystals (such as LiI [28]), there exist specific anion–anion interactions that stabilize the structure. On the other hand, quantum-chemical calculations of some salts (such as AlX_3 (X = F, Cl, OH) [29]) revealed the presence of bcps along the Al ··· Al lines, implying the existence of weak cation-cation Al ··· Al interactions. At first glance, the stabilizing role of such interactions contradicts a traditional crystal-chemical intuition [30], however, the presence of bcps unequivocally indicates that there is a bond path between the corresponding pairs of atoms [31]. Nelyubina et al. [32] and Gibbs et al. [33] provided useful reviews on the subject of anion–anion interactions in various chemical compounds. In particular, Gibbs et al. [33] analyzed the O–O interactions along the shared edges of cation coordination polyhedra in silicates and demonstrated that these weak bonds indeed stabilize the structure, though the stabilizing effect might be considered as marginal relative to the metal–oxygen interactions.

In a series of papers, Gibbs et al. [34–36] investigated secondary van der Waals bonding in inorganic molecular crystals such as As_4S_n (n = 3, 4, 5) [36], arsenolite, As_2O_3 [34], and orpiment, As_2S_3 [35], and reported on the existence of intermolecular closed-shell As–X interactions (X = O, S). The As–X bonds are directed and are of the Lewis acid-base type, i.e., they link locally concentrated (nucleophilic, Lewis-base) electron density regions on the As atoms to locally depleted (electrophilic, Lewis-acid) electron density regions on the X atoms. In addition, in some structures, there are also As ··· As and O ··· O interactions.

For a long time, we have been interested in the crystal chemistry of inorganic oxysalts containing lone-electron-pair cations such as Pb^{2+} [37–40], Tl^{+} [41], and Se^{4+} [42,43]. In this report, we investigate

a number of zinc and copper selenite chlorides from the viewpoint of the analysis of their electron density distributions that may provide novel ideas to understand the role that weak Se–Cl closed-shell interactions play in the structural organization of these compounds.

Table 1 provides crystallographic information on the compounds that will be considered in the following. Among the seven compounds, three are naturally occurring selenite chlorides first discovered in the fumaroles of the Tolbachik volcano, Kamchatka, Russia. For the purpose of structure comparison, three pairs of polymorphic modifications have been selected, namely, two modifications of $Zn_2(SeO_3)Cl_2$, two modifications of $Cu_3(SeO_3)_2Cl_2$, and two modifications of $Cu_5O_2(SeO_3)_2Cl_2$.

Table 1. Crystallographic data for selected selenite chlorides analyzed using the atoms-in-molecules (AIM) theory.

#	Chemical Formula	Mineral Name	Space Group	*a*, Å/*α*, Deg.	*b*, Å/*β*, Deg.	*c*, Å/*γ*, Deg.	Ref.
1	α-$Zn_2(SeO_3)Cl_2$	sofiite	*Pccn*	10.251/90	15.223/90	7.666/90	[44]
2	β-$Zn_2(SeO_3)Cl_2$	-	$P2_1/c$	7.670/90	10.261/100.0	7.657/90	[45]
3	α-$Cu_5O_2(SeO_3)_2Cl_2$	georgbokiite	$P2_1/c$	6.030/90	13.744/95.8	5.562/90	[46]
4	β-$Cu_5O_2(SeO_3)_2Cl_2$	parageorgbokiite	$P2_1/c$	5.398/90	8.054/99.3	11.128/90	[47]
5	$KCdCu_7O_2(SeO_3)_2Cl_9$	burnsite	$P6_3/mmc$	8.781/90	8.781/90	15.521/120	[48]

The CRYSTAL14 software package was used to perform the solid-state DFT calculations [49]. The Peintinger−Oliveira−Bredow split-valence triple-ζ (pob-TZVP) basis sets [50] were used for all atoms, except Cd in burnsite [51], along with the hybrid Becke-3−Lee−Yang−Parr (B3LYP) functional. The electron-density distribution function was calculated using experimentally observed geometries for each structure and analyzed using the *TOPOND14* software [52,53] with respect to the properties of the bond critical points in electron density distributions and scalar fields of the electron-density Laplacian [53].

3. Results and Discussion

3.1. $Zn_2(SeO_3)Cl_2$ Polymorphs

Sophiite, α-$Zn_2(SeO_3)Cl_2$, was first discovered in fumaroles of the Tolbachik volcano, Kamchatka peninsula, Russia [12]. Its β-polymorph was synthesized by chemical transport reactions [45], which has repeatedly been used for simulation of fumarolic mineralization [54]. It is noteworthy that both polymorphs of $Zn_2(SeO_3)Cl_2$ are highly hygroscopic. Their crystal structures are very close to each other and both are based upon the same type of electroneutral $[Zn_2(SeO_3)Cl_2]^0$ layers formed by (ZnO_2Cl_2) tetrahedra, (ZnO_4Cl_2) octahedra, and (SeO_3) trigonal pyramids (Figure 1a). The (ZnO_4Cl_2) octahedra share common O corners to form chains running parallel to *c* in both polymorphs. Each octahedron shares one O–Cl edge with an adjacent (ZnO_2Cl_2) tetrahedron and one O–O edge with (SeO_3) pyramid, which provide linkage of the chains into two-dimensional layers. The layers are parallel to (010) in sofiite (Figure 1b) and to (100) in the β-polymorph (Figure 1c). The structures of both modifications may be considered as polytypes, since they are based upon the same type of layers. According to the modern nomenclature, sofiite as α-$Zn_2(SeO_3)Cl_2$ should be regarded as 2*O*-polytype (orthorhombic structure with two layers per unit cell), whereas β-$Zn_2(SeO_3)Cl_2$ should be considered as 1*M*-polytype (monoclinic structure with one layer per unit cell). Since the layers in the structures of both polytypes are electroneutral, the linkage between the layers is achieved through the secondary bonds that involve Cl^- anions and Se^{4+} cations (Figure 1).

The lists of bcps found for sofiite and β-$Zn_2(SeO_3)Cl_2$ are given in Tables 2 and 3, respectively. It can be clearly seen that the interatomic interactions in the two structures can be subdivided into two groups: interactions with $H(\mathbf{r_c}) < 0$ and interactions with $H(\mathbf{r_c}) > 0$. The first kind of interactions is observed for the Se–O, Zn–O, and Zn–Cl bonds. These interactions correspond to the intralayer bonding and can be characterized as belonging to the intermediate type (since $\nabla^2\rho(\mathbf{r_c}) > 0$ for all

interactions in the two structures). According to the $\rho(\mathbf{r_c})$ values, these bonds can be separated into Se–O bonds ($\rho(\mathbf{r_c})$ = 0.18–0.20 a.u.) and Zn–X bonds ($\rho(\mathbf{r_c})$ = 0.02–0.08 a.u.).

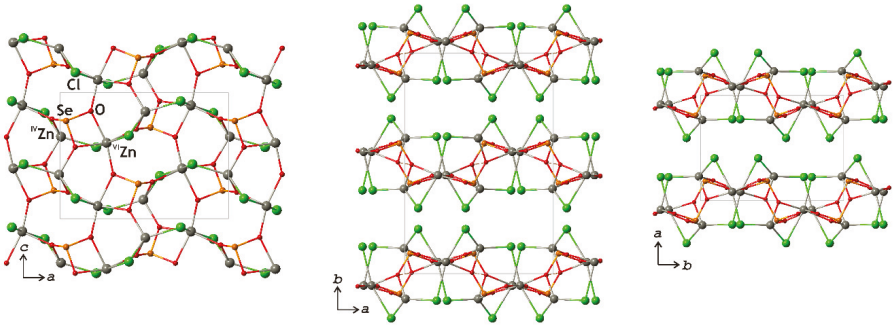

(**a**) (**b**) (**c**)

Figure 1. The crystal structures of the $Zn_2(SeO_3)Cl_2$ polymorphs: (**a**) the structure of the $[Zn_2(SeO_3)Cl_2]^0$ layer in sofiite; (**b**) the projection of the structure of sofiite parallel to the *c* axis; (**c**) the projection of the structure of β-$Zn_2(SeO_3)Cl_2$ parallel to the *c* axis. Legend: Zn, Se, Cl, and O atoms are shown as gray, orange, green, and red spheres, respectively.

The most interesting are the bcps, for which $\nabla^2\rho(\mathbf{r_c}) > 0$ and $H(\mathbf{r_c}) > 0$. These bond paths correspond to the Se–Cl, Cl–Cl, and O–O closed-shell interactions, which we shall analyse in more detail. The geometrical environments around the atoms participating in weak closed-shell interactions in sofiite are shown in Figure 2. There are three Se–Cl interactions (Figure 2a), from which two interactions (Se–Cl1 and Se–Cl2) are intralayer and one Se–Cl2 interaction is interlayer. The same situation is also observed in β-$Zn_2(SeO_3)Cl_2$ (Figure 3a). In sofiite, the interlayer interaction corresponds to the shortest Se–Cl distance of 3.317 Å, whereas, in β-$Zn_2(SeO_3)Cl_2$, the respective Se–Cl distance is the longest among three Se–Cl contacts with its length equal to 3.514 Å. Taking into account weak interactions, the coordination of Se atom in both polymorphs can be considered as a distorted trigonal (SeO_3Cl_3) prism with the O_3 and Cl_3 triangular bases. The Se–O interactions are more than one order stronger than the Se–Cl interactions. The number of Cl–Cl interactions in the two $Zn_2(SeO_3)Cl_2$ is notably different, despite the fact that the number of symmetrically independent bcps is the same (Tables 2 and 3). The point is that two Cl–Cl bcps in sofiite are located on the twofold axes, whereas similar bcps in β-$Zn_2(SeO_3)Cl_2$ are in general positions. In general, the structure of β-$Zn_2(SeO_3)Cl_2$ contains 12 Cl–Cl bcps per interlayer, whereas the structure of sofiite contains only 8. The difference results in different coordinations of the Cl atoms in the structures of the two polymorphs.

The Cl1 atom (Figure 2b) is linked to two Zn atoms and participates in three Cl–Cl and one Se–Cl interactions. The overall coordination of the Cl1 atom can be described as distorted octahedral. From four weak closed-shell interactions, only one Cl–Cl interaction has an interlayer character. In β-$Zn_2(SeO_3)Cl_2$, the analogue of the Cl1 position in sofiite is the Cl2 site (Figure 3c). Its intralayer coordination (by two Zn, one Se, and two Cl atoms) is very similar to that observed in sofiite. However, there are two interlayer Cl–Cl interactions versus one in sofiite. Thus, the total coordination of the Cl2 site in the β-polymorph is sevenfold. The coordination of the Cl2 site in sofiite is shown in Figure 2c. There are two intralayer Cl–Zn bonds and one intralayer Cl–Se interaction. The interlayer interactions are characterized by one Cl–Se and one Cl–Cl bond paths. The situation in β-$Zn_2(SeO_3)Cl_2$ is again different (Figure 3b). The number of intralayer interactions is the same as in sofiite, but there are three interlayer interactions, one Cl–Se and two Cl–Cl. In total, the coordination of the Cl1 site in the β-polymorph is sixfold versus fivefold in sofiite.

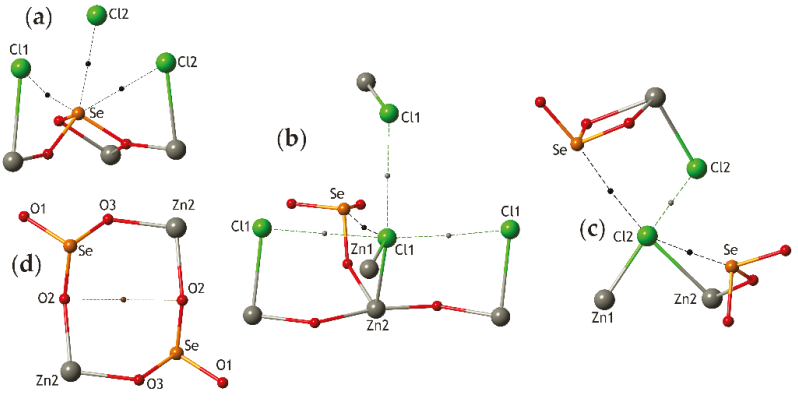

Figure 2. Geometrical environment of bond critical points of weak closed-shell interactions in sofiite, α-$Zn_2(SeO_3)Cl_2$: (**a**) the bcps around the Se site; (**b**) the bcps around the Cl1 site; (**c**) the bcps around the Cl2 site; (**d**) bcp between the O2 and O2 atoms. Legend as in Figure 1.

Table 2. Bond critical points in the crystal structure of sofiite, α-$Zn_2(SeO_3)Cl_2$, and their properties.

A_1	A_2	d [Å]	$\rho(r_c)$	$\nabla^2\rho(r_c)$	$G(r_c)$	$V(r_c)$	$H(r_c)$	BD
Se–O and Zn–X bonds (X = O, Cl)								
Se	O1	1.688	0.1940	0.4591	0.2357	−0.3566	−0.1209	−0.624
Se	O3	1.697	0.1922	0.4144	0.2247	−0.3458	−0.1211	−0.630
Se	O2	1.701	0.1883	0.4108	0.2196	−0.3364	−0.1168	−0.620
Zn1	O1	1.993	0.0758	0.3908	0.1109	−0.1242	−0.0133	−0.175
Zn1	O2	2.057	0.0667	0.3232	0.0908	−0.1007	−0.0099	−0.148
Zn1	Cl2	2.205	0.0784	0.2664	0.0849	−0.1033	−0.0184	−0.235
Zn1	Cl1	2.244	0.0732	0.2346	0.0746	−0.0905	−0.0159	−0.217
Zn2	O1	1.993	0.0781	0.3984	0.1144	−0.1292	−0.0148	−0.190
Zn2	O2	2.115	0.0558	0.2667	0.0717	−0.0766	−0.0049	−0.088
Zn2	O3	1.955	0.0837	0.4391	0.1267	−0.1435	−0.0168	−0.201
Zn2	O3	2.147	0.0551	0.2511	0.0687	−0.0747	−0.0060	−0.109
Zn2	Cl2	2.685	0.0298	0.0783	0.0220	−0.0245	−0.0025	−0.084
Zn2	Cl1	2.753	0.0256	0.0652	0.0180	−0.0197	−0.0017	−0.066
Se–Cl, Cl–Cl, and O–O interactions								
Se	Cl2	3.317	0.0121	0.0349	0.0078	−0.0069	0.0009	0.074
Se	Cl2	3.444	0.0103	0.0312	0.0069	−0.0060	0.0009	0.087
Se	Cl1	3.533	0.0080	0.0268	0.0057	−0.0046	0.0011	0.138
Cl1	Cl1	3.898	0.0039	0.0143	0.0028	−0.0021	0.0007	0.179
Cl1	Cl1	3.955	0.0029	0.0115	0.0022	−0.0015	0.0007	0.241
Cl2	Cl2	3.567	0.0071	0.0208	0.0046	−0.0041	0.0005	0.070
O2	O2	3.362	0.0055	0.0181	0.0038	0.0030	0.0008	0.145

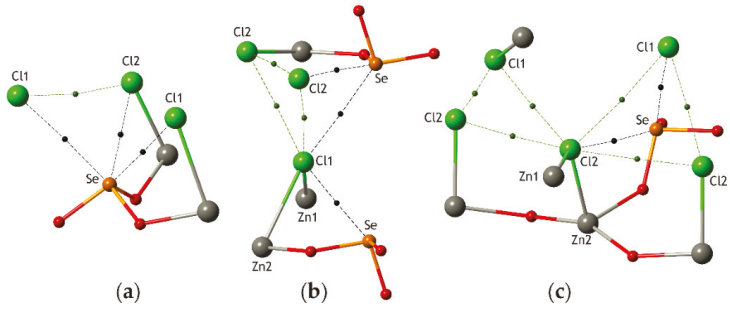

Figure 3. Geometrical environment of bond critical points of weak closed-shell interactions in β-$Zn_2(SeO_3)Cl_2$: (**a**) The bcps around the Se site; (**b**) The bcps around the Cl1 site; (**c**) The bcps around the Cl2 site. Legend as in Figure 1.

Table 3. Bond critical points in the crystal structure of β-$Zn_2(SeO_3)Cl_2$ and their properties.

A_1	A_2	d [Å]	$\rho(r_c)$	$\nabla^2\rho(r_c)$	$G(r_c)$	$V(r_c)$	$H(r_c)$	BD
Se–O and Zn–*X* bonds (*X* = O, Cl)								
Se1	O3	1.703	0.1901	0.3856	0.2163	−0.3361	−0.1198	−0.630
Se1	O1	1.707	0.1879	0.3797	0.2123	−0.3297	−0.1174	−0.625
Se1	O2	1.715	0.1836	0.3736	0.2065	−0.3196	−0.1131	−0.616
Zn2	O1	2.126	0.0574	0.2672	0.0733	−0.0798	−0.0065	−0.113
Zn1	O1	1.983	0.0779	0.4009	0.1147	−0.1291	−0.0144	−0.185
Zn1	O2	2.031	0.0702	0.3492	0.0984	−0.1096	−0.0112	−0.160
Zn1	Cl1	2.222	0.0761	0.2519	0.0801	−0.0972	−0.0171	−0.225
Zn1	Cl2	2.226	0.0751	0.2519	0.0795	−0.0961	−0.0166	−0.221
Zn2	O3	2.008	0.0737	0.3733	0.1056	−0.1178	−0.0122	−0.166
Zn2	O2	2.049	0.0663	0.3304	0.0914	−0.1002	−0.0088	−0.133
Zn2	O3	2.150	0.0546	0.2470	0.0676	−0.0735	−0.0059	−0.108
Zn2	Cl2	2.430	0.0487	0.1555	0.0445	−0.0501	−0.0056	−0.115
Zn2	Cl1	2.765	0.0250	0.0649	0.0179	−0.0196	−0.0017	−0.068
Se–Cl, Cl–Cl, and O–O interactions								
Se1	Cl2	3.382	0.0106	0.0343	0.0075	−0.0064	0.0009	0.085
Se1	Cl1	3.482	0.0096	0.0297	0.0065	−0.0055	0.0010	0.104
Se1	Cl1	3.514	0.0085	0.0252	0.0053	−0.0044	0.0009	0.106
Cl1	Cl2	3.534	0.0079	0.0225	0.0051	−0.0046	0.0005	0.063
Cl1	Cl2	3.956	0.0029	0.0113	0.0021	−0.0014	0.0007	0.241
Cl2	Cl2	3.869	0.0041	0.0151	0.0030	−0.0022	0.0008	0.195
O2	O2	3.470	0.0048	0.0155	0.0032	−0.0026	0.0006	0.125

In both polymorphs, there is a bcp between the two O atoms located in the middle of the eight-membered atomic ring (Figure 2d). This bcp is located in the inversion center and corresponds to a very weak closed-shell interaction.

The higher relative number of bcps in β-$Zn_2(SeO_3)Cl_2$ compared to sofiite might be related to the higher stability of the β-polymorph. Its physical density, 3.68 $g{\cdot}cm^{-3}$ is slightly higher than that of sofiite, 3.65 $g{\cdot}cm^{-3}$, which manifests the higher efficiency of layer packing, which, in turn, may lead to the formation of more interlayer interactions, thus stabilizing the β-polymorph. It is noteworthy that, among the closed-shell interactions in the two polymorphs, the Se–Cl interactions are stronger than others, pointing out their important role in the linkage of the $[Zn_2(SeO_3)Cl_2]^0$ in the structures. Nevertheless, the Cl–Cl interactions are also of importance, providing additional contributions to the structural stability.

3.2. $Cu_5O_2(SeO_3)_2Cl_2$ Polymorphs

In fact, α-$Cu_5O_2(SeO_3)_2Cl_2$ was the first selenite chloride reported by Galy et al. back in 1979 [55]. Its dark-brown crystals were prepared by the chemical vapor transport reactions method. In 1999, it was described by Vergasova et al. [16] as a natural mineral species from fumaroles of the Great fissure Tolbachik eruption (Kamchatka, Russia). In 2006, Vergasova et al. [20] described another natural polymorph of $Cu_5O_2(SeO_3)_2Cl_2$, which was named parageorgbokiite in order to recognize its chemical similarity to georgbokiite. It is noteworthy that, in contrast to georgbokiite, the crystals of parageorgbokiite are green and thus the two polymorphs can easily be distinguished. The crystal structures of georgbokiite and parageorgbokiite are closely related and the best way to understand these relations are to describe them in terms of structural units based upon oxocentered tetrahedra formed around 'additional' O atoms not bonded to Se^{4+} cations. This approach was first proposed in 1968 [56] and recently developed into a coherent crystal chemical theory (see [57,58] for reviews and historical remarks). In general, description of certain crystal structures in terms of anion-centered coordination polyhedra became more popular over the years, in part due to the recent reports on interesting structural and physical properties and mineralogical importance of antiperovskites, i.e., materials with structures based upon anion-centered octahedra [59–66].

In the crystal structures of both polymorphs of $Cu_5O_2(SeO_3)_2Cl_2$, there are additional O atoms not bonded to Se and tetrahedrally coordinated by four Cu atoms thus forming (OCu_4) oxocentered tetrahedra. In both structures, (OCu_4) tetrahedra share Cu–Cu edges and Cu corners to form [O_2Cu_5] chains shown in Figure 4a. The (SeO_3) groups are attached to (OCu_4) tetrahedra in a face-to-face fashion [67,68], which means that the triangular bases of both units are parallel to each other and have the same orientation. The complex 1-dimensional structural units with the composition $\{[O_2Cu_5](SeO_3)_2\}^{2+}$ shown in Figure 4b are the basic structural modules for both polymorphs and it is the mode of their combination that generates the structural difference.

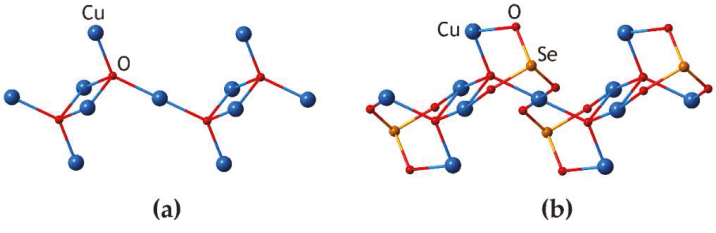

Figure 4. The basic structural module for the crystal structures of the $Cu_5O_2(SeO_3)_2Cl_2$ polymorphs (georgbokiite and parageorgbokiite): (**a**) the [O_2Cu_5] chain formed by alternating edge- and corner-sharing (OCu_4) tetrahedra; (**b**) the $\{[O_2Cu_5](SeO_3)_2\}$ 1-dimensional module formed by the face-to-face attachment of (SeO_3) groups to (OCu_4) tetrahedra.

Figure 5 shows a successive (step-by-step) construction of the crystal structure of georgbokiite, α-$Cu_5O_2(SeO_3)_2Cl_2$, if viewed in terms of anion-centered tetrahedra. The [O_2Cu_5] chains are running parallel to the *c* axis and grouped into layers parallel to the (100) plane (Figure 5a). The (SeO_3) groups are attached to the chains and are also responsible for the linkage of the $\{[O_2Cu_5](SeO_3)_2\}^{2+}$ in the (100) and (010) directions through the formation of the Cu–O bonds (Figure 5b). The metal-oxide bonding network based upon the Cu–O and Se–O bonds contains the strongest chemical bonds in the structure. It can be seen, however, that this network possesses 1-dimensional channels parallel to (001) (i.e., the direction of extension of the [O_2Cu_5] chains) and these channels are occupied by Cl^- anions (Figure 5c). These channels are also remarkable by the fact that they provide spatial localization of the weak closed-shell interactions in the crystal structure (Figure 5d).

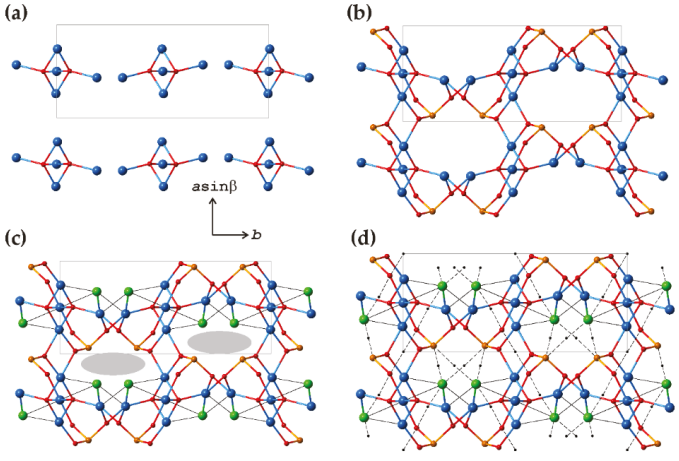

Figure 5. The scheme of successive (step-by-step) construction of the crystal structure of georgbokiite, α-$Cu_5O_2(SeO_3)_2Cl_2$: (**a**) the arrangement of the $[O_2Cu_5]$ chains of edge- and corner-sharing (OCu_4) tetrahedra; (**b**) the metal-oxide bonding network of the Cu–O and Se–O bonds; (**c**) the structure projection showing the positions of the Cl atoms and the location of extended channels parallel to [001] (shown in gray); (**d**) the location of bcps corresponding to weak closed-shell interactions. See text for details. Legend: Cu, Se, O, and Cl atoms are shown as blue, orange, red, and green spheres, respectively. Small black spheres indicate the positions of bcps.

The mode of linkage of the basic structural modules in the structure of parageorgbokiite, β-$Cu_5O_2(SeO_3)_2Cl_2$, is different, which is illustrated in Figure 6.

In contrast to georgbokiite, the $[O_2Cu_5]$ chains in parageorgbokiite have different relative orientations (Figure 6a) and are parallel to the *a* axis. Their linkage through (SeO_3) groups (attached to the (OCu_4) tetrahedra in the face-to-face fashion) results in the formation of a 3-dimensional framework of relatively strong bonds (Figure 6b) with channels occupied by Cl^- anions (Figure 6c) and hosting the bcps corresponding to weak closed-shell interactions (Figure 6d).

Tables 4 and 5 provide lists of bcps found for georgbokiite and parageorgbokiite, respectively. According to their properties, all interatomic interactions in the two minerals can be classified into three groups:

(1) the Cu–O, Cu–Cl and Se–O interactions with $\nabla^2\rho(\mathbf{r_c}) > 0$ and $H(\mathbf{r_c}) < 0$ (intermediate bonding interactions);
(2) the Cu–O and Cu–Cl interactions with $\nabla^2\rho(\mathbf{r_c}) > 0$ and $H(\mathbf{r_c}) > 0$ (closed-shell interactions); the Cu3–Cl interaction (2.739 Å) deserves special attention as this interaction lies exactly on the border between intermediate and closed-shell interactions ($H(\mathbf{r_c}) = 0$);
(3) the closed-shell Se–Cl, Cl–Cl, and Cl–O interactions with $\nabla^2\rho(\mathbf{r_c}) > 0$ and $H(\mathbf{r_c}) > 0$.

The appearance of the second group of interactions (which is absent in the $Zn_2(SeO_3)Cl_2$ polymorphs) is due to the Jahn–Teller distortion of Cu^{2+} coordination [69], which results in the splitting of Cu–*X* interactions (*X* = O, Cl) into short and long bonds. It is noteworthy that the empirical bond-valence theory [70] would make no distinction between the different long Cu–*X* bonds, whereas the data given in Tables 4 and 5 indicate that the AIM theory classifies them into closed-shell and intermediate interactions (taking into account the conditional character of the adopted classification (see Section 2)). In particular, for the Cu–Cl bonds, the border between the two types of interactions corresponds to the Cu–Cl distance of 2.739 Å. It is of interest that the $\rho(r_c)$ for the closed-shell Cu–*X* interactions is of the same order as for other closed-shell interactions in the two structures.

Table 4. Bond critical points in the crystal structure of α-$Cu_5O_2(SeO_3)_2Cl_2$ and their properties.

A_1	A_2	d [Å]	$\rho(r_c)$	$\nabla^2\rho(r_c)$	$G(r_c)$	$V(r_c)$	$H(r_c)$	BD
Cu1	O1	1.923	0.0979	0.3812	0.1339	−0.1725	−0.0386	−0.394
Cu1	O4	1.962	0.0855	0.3506	0.1189	−0.1501	−0.0312	−0.365
Cu1	O4	2.046	0.0694	0.2766	0.0922	−0.1153	−0.0231	−0.333
Cu1	Cl	2.282	0.0682	0.1701	0.0658	−0.0890	−0.0232	−0.340
Cu1	Cl	2.570	0.0371	0.1248	0.0352	−0.0392	−0.0040	−0.108
Cu2	O2	1.944	0.0877	0.3727	0.1248	−0.1564	−0.0316	−0.360
Cu2	O1	1.971	0.0857	0.3284	0.1144	−0.1467	−0.0323	−0.377
Cu2	Cl	2.954	0.0164	0.0608	0.0138	−0.0123	0.0015	0.091
Cu3	O2	1.989	0.0786	0.3254	0.1089	−0.1364	−0.0275	−0.350
Cu3	O1	1.956	0.0911	0.3433	0.1214	−0.1570	−0.0356	−0.391
Cu3	O1	1.952	0.0935	0.3464	0.1238	−0.1611	−0.0373	−0.399
Cu3	O3	2.024	0.0723	0.2917	0.0973	−0.1217	−0.0244	−0.337
Cu3	O2	2.430	0.0283	0.1314	0.0327	−0.0326	0.0001	0.004
Cu3	Cl	2.739	0.0254	0.0915	0.0229	−0.0229	0.0000	0.000
Se	O2	1.674	0.1998	0.4741	0.2453	−0.3721	−0.1268	−0.635
Se	O3	1.709	0.1870	0.3738	0.2105	−0.3275	−0.1170	−0.626
Se	O4	1.724	0.1820	0.3276	0.1952	−0.3084	−0.1132	−0.622
Se	Cl	3.310	0.0129	0.0378	0.0083	−0.0072	0.0011	0.085
Se	Cl	3.544	0.0086	0.0244	0.0053	−0.0045	0.0008	0.093
Cl	O2	3.216	0.0113	0.0358	0.0082	−0.0074	0.0008	0.071
O2	O2	3.972	0.0083	0.0297	0.0062	−0.0050	0.0012	0.145

Table 5. Bond critical points in the crystal structure of β-$Cu_5O_2(SeO_3)_2Cl_2$ and their properties.

A_1	A_2	d [Å]	$\rho(r_c)$	$\nabla^2\rho(r_c)$	$G(r_c)$	$V(r_c)$	$H(r_c)$	BD
Cu1	O1	1.919	0.0976	0.3890	0.1350	−0.1727	−0.0377	−0.386
Cu1	O2	1.966	0.0824	0.3500	0.1164	−0.1453	−0.0289	−0.351
Cu1	O3	1.969	0.0834	0.3406	0.1153	−0.1455	−0.0302	−0.362
Cu1	Cl	2.268	0.0706	0.1716	0.0676	−0.0923	−0.0247	−0.350
Cu1	O4	2.944	0.0096	0.0425	0.0081	−0.0056	0.0025	0.260
Cu1	Cl	3.185	0.0096	0.0392	0.0079	−0.0060	0.0019	0.198
Cu2	O1	1.929	0.0944	0.3815	0.1314	−0.1675	−0.0361	−0.382
Cu2	O4	1.974	0.0823	0.3329	0.1128	−0.1425	−0.0297	−0.361
Cu3	O1	1.945	0.0934	0.3585	0.1260	−0.1625	−0.0365	−0.391
Cu3	O2	1.961	0.0832	0.3576	0.1187	−0.1480	−0.0293	−0.352
Cu3	O1	1.975	0.0885	0.3237	0.1158	−0.1506	−0.0348	−0.393
Cu3	O3	2.057	0.0672	0.2650	0.0881	−0.1099	−0.0218	−0.324
Cu3	O4	2.399	0.0311	0.1409	0.0363	−0.0374	−0.0011	−0.035
Cu3	Cl	2.705	0.0283	0.0977	0.0254	−0.0264	−0.0010	−0.035
Se	O4	1.675	0.2000	0.4610	0.2428	−0.3704	−0.1276	−0.638
Se	O3	1.713	0.1850	0.3654	0.2061	−0.3208	−0.1147	−0.620
Se	O2	1.724	0.1813	0.3406	0.1971	−0.3091	−0.1120	−0.618
Se	Cl	3.300	0.0133	0.0408	0.0093	−0.0083	0.0010	0.075
Se	Cl	3.327	0.0123	0.0357	0.0078	−0.0067	0.0011	0.089
Cl	O2	3.321	0.0097	0.0278	0.0065	−0.0060	0.0005	0.052
Cl	Cl	3.501	0.0104	0.0284	0.0068	−0.0065	0.0003	0.029
Cl	Cl	3.810	0.0046	0.0158	0.0032	−0.0025	0.0007	0.152

The configuration of closed-shell interactions inside the channels in the crystal structures of the $Cu_5O_2(SeO_3)_2Cl_2$ polymorphs is shown in Figure 7. In georgbokiite (Figure 7a), the channels are more compact and have (SeO_3) groups on one side and Cl^- anions on another, each Se and each Cl atom participates in two Se–Cl interactions, and there are no Cl–Cl interactions. In contrast, in parageorgbokiite (Figure 7b), the channels are larger and have both (SeO_3) groups and Cl^- anions on both sides. Each Se atom participates in two Se–Cl interactions, whereas each Cl atom participates in two Se–Cl, two Cl–Cl and one Cl–O interactions. The structure of the channels in the two polymorphs

is therefore remarkably different, which can be explained by the different arrangements of basic structural modules.

The more open character of the crystal structure of parageorgbokiite compared to that of georgbokiite is reflected in the values of physical densities, which are equal to 4.88 and 4.69 $g \cdot cm^{-3}$ for the α- and β-polymorphs, respectively. According to Krivovichev et al. [47], parageorgbokiite is most likely a high-temperature modification of $Cu_5O_2(SeO_3)_2Cl_2$, however, the relative stabilities of the two minerals are unknown. It is of interest that, whereas georgbokiite can easily be synthesized by the chemical vapor transport reactions method [55,71], no synthetic analogue is known for parageorgbokiite.

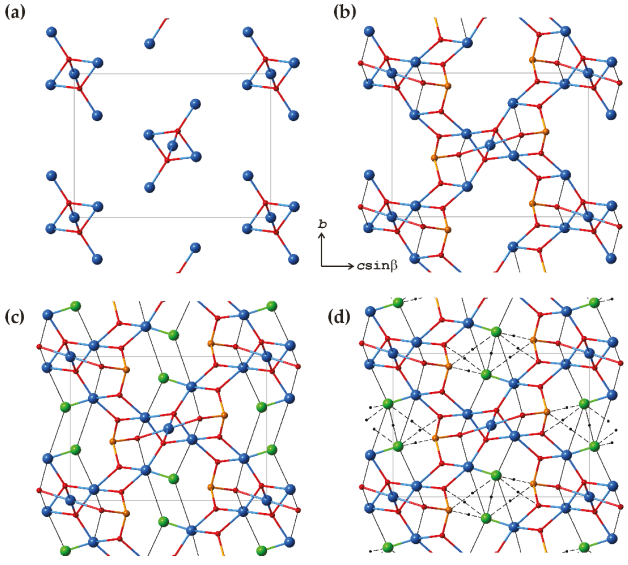

Figure 6. The scheme of successive (step-by-step) construction of the crystal structure of parageorgbokiite, β-$Cu_5O_2(SeO_3)_2Cl_2$: (**a**) the arrangement of the $[O_2Cu_5]$ chains of edge- and corner-sharing (OCu_4) tetrahedra; (**b**) the metal-oxide bonding network of the Cu–O and Se–O bonds; (**c**) the structure projection showing the positions of the Cl atoms; (**d**) the location of bcps corresponding to weak closed-shell interactions. See text for details. Legend as in Figure 5.

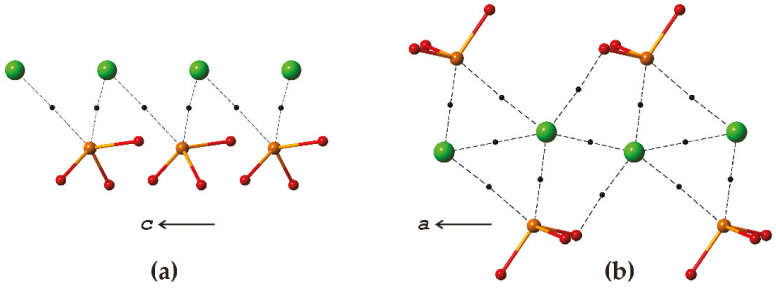

Figure 7. The arrangement of (SeO_3) groups and Cl atoms in the channels in the crystal structures of georgbokiite (**a**) and parageorgbokiite (**b**). Dashed lines indicate bond paths that correspond to weak closed-shell interactions. Legend as in Figure 5.

3.3. Burnsite, $KCdCu_7O_2(SeO_3)_2Cl_9$

Burnsite, $KCdCu_7O_2(SeO_3)_2Cl_9$, was discovered in Tolbachik fumaroles in 2002 [18]. By analogy with $Cu_5O_2(SeO_3)_2Cl_2$ polymorphs, its crystal structure contains additional O atoms tetrahedrally coordinated by four Cu atoms [48]. Two (OCu_4) tetrahedra share a common Cu atom to form a [O_2Cu_7] dimer (Figure 8a) similar to those recently observed in the crystal structure of $Na_2Cu_7O_2(SeO_3)_4Cl_4$ [72,73].

In the crystal structure of burnsite, the [O_2Cu_7] dimers are surrounded by two (SeO_3) groups each of them attached to the (OCu_4) tetrahedra in a face-to-face fashion (Figure 8b). The resulting {[O_2Cu_7](SeO_3)$_2$} groups are linked via Cu–O bonds into an open three-dimensional framework (Figure 9a) with large cavities occupied by Cd^{2+}, K^+, and Cl^- ions (Figure 9b).

Table 6 provides a list of bcps in the crystal structure of burnsite. It can be seen that most of the interatomic interactions can be described as belonging to the intermediate type with $\nabla^2\rho(r_c) > 0$ and $H(r_c) < 0$, except for the Se–Cl interactions that are of the closed-shell type ($\nabla^2\rho(r_c) > 0$ and $H(r_c) > 0$). Figure 8c shows the atomic configuration inside the cavity occupied by two (SeO_3) groups and three Cl^- ions.

Table 6. Bond critical points in the crystal structure of burnsite, $KCdCu_7O_2(SeO_3)_2Cl_9$, and their properties.

A_1	A_2	d [Å]	$\rho(r_c)$	$\nabla^2\rho(r_c)$	$G(r_c)$	$V(r_c)$	$H(r_c)$	BD
Cd	Cl1	2.614	0.0426	0.1420	0.0395	−0.0436	−0.0041	−0.096
Cu1	O1	1.899	0.1016	0.4263	0.1447	−0.1828	−0.0381	−0.375
Cu1	O2	1.916	0.0906	0.4215	0.1362	−0.1670	−0.0308	−0.340
Cu1	O2	2.127	0.0580	0.2304	0.0736	−0.0896	−0.0160	−0.276
Cu1	Cl2	2.555	0.0369	0.1152	0.0331	−0.0374	−0.0043	−0.117
Cu1	Cl1	2.612	0.0331	0.1101	0.0300	−0.0324	−0.0024	−0.073
Cu2	O1	1.914	0.0980	0.4169	0.1409	−0.1776	−0.0367	−0.374
Cu2	Cl2	2.451	0.0484	0.1460	0.0464	−0.0562	−0.0098	−0.202
Se	O2	1.687	0.1936	0.4591	0.2350	−0.3553	−0.1203	−0.621
Se	Cl2	3.532	0.0085	0.0270	0.0058	−0.0048	0.0010	0.118

Each (SeO_3) group forms participates in three Se–Cl interactions, so that the full coordination of Se^{4+} ions can be viewed as trigonal prismatic, similar to that observed in the crystal structures of the $Zn_2(SeO_3)Cl_2$ polymorphs (see above). Each Cl_2 atom participates in two Cl–Se closed-shell interactions.

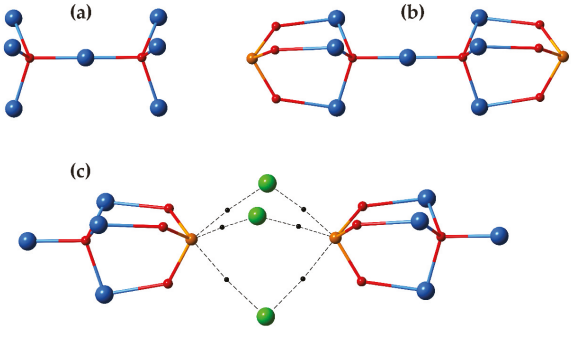

Figure 8. The [O_2Cu_7] dimer of two corner-sharing (OCu_4) tetrahedra in the crystal structure of burnsite (**a**) and its coordination by two (SeO_3) groups (**b**). The atomic configuration inside the metal-oxide framework cavity showing the orientation of Se–Cl closed-shell interactions. (**c**) Legend as in Figure 5.

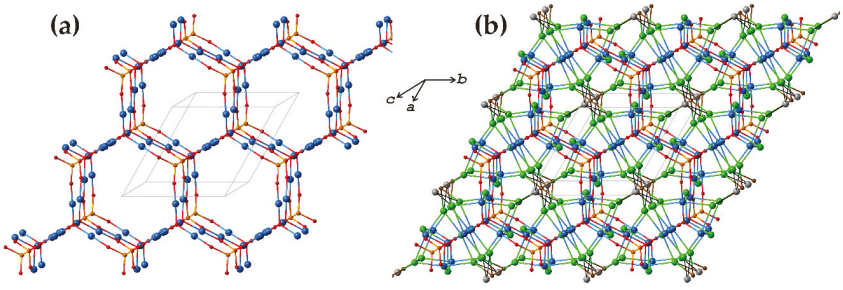

Figure 9. The open framework metal-oxide framework formed by $[O_2Cu_7]$ dimers and (SeO_3) groups in the crystal structure of burnsite (**a**) and the projection of the whole structure of burnsite featuring filling framework cavities by Cd^{2+}, K^+, and Cl^- ions (**b**). Legend: Cu, Se, O, Cl, K, and Cd atoms are shown as blue, orange, red, green, gray, and brown spheres, respectively.

4. Conclusions

The analysis of theoretical electron density distributions in selenite chlorides reveals the existence in their structures of two basic types of interactions: intermediate interactions with essential covalent contribution [$\nabla^2\rho(\mathbf{r_c}) > 0$ and $H(\mathbf{r_c}) < 0$] and closed-shell interactions [$\nabla^2\rho(\mathbf{r_c}) > 0$ and $H(\mathbf{r_c}) > 0$]. In the $Zn_2(SeO_3)Cl_2$ polymorphs and burnsite, all *Me*–*X* interactions are of the first type, whereas, in georgbokiite and parageorgbokiite, the Jahn–Teller distortion of the Cu^{2+} coordination geometry results in the elongation of some of the Cu–*X* bonds and their transition to the closed-shell type. All anion-anion (Cl–Cl and O–O) interactions are of the closed-shell type as well, quite comparable with the previous observations of anion–anion bonding in inorganic salts [32].

The nature of the Se–Cl interactions deserves special attention. The analysis of the bond-critical points of the Laplacian of the electron-density distribution indicates that, at least in selenite chlorides under consideration, it is different from that of the halogen or chalcogen bonds [74–76], i.e., it is not of the electron donor/electron acceptor type. The regions with concentrated and depleted regions of electron density around Se^{4+} and Cl^- ions do not correlate with each other and are not aligned with the Se–Cl bonding paths. However, the Se–Cl interaction corresponds to the overlap of van der Waals radii: the typical Se–Cl distance is selenite chlorides is in the range 3.30–3.55 Å, whereas the sum of the van der Waals radii (R^W) is equal to $R^W_{Se} + R^W_{Cl} = 1.9 + 1.8 = 3.7$ Å [77]. The energy of the Se–Cl closed-shell interactions, E_{int}, can be estimated using the equation proposed by Espinosa et al. [78]:

$$E_{int} = -313.754\ V(\mathbf{r_c}), \quad (2)$$

where $V(\mathbf{r_c})$ is the potential electron energy density at bcp expressed in atomic units (a.u.). Taking into account that the $V(\mathbf{r_c})$ value in selenite chlorides analyzed above varies from −0.0083 to −0.0044 a.u., the energy of the Se–Cl closed-shell interactions can be estimated as 1.4–2.6 kcal·mol^{-1}. This energy range is comparable to that observed for weak hydrogen bonds [79] or other weakly bonded configurations, e.g., weak I–O bonds in α-HIO_3 [80], and anion–anion and cation–cation interactions [81,82]. Despite their weakness, these interactions provide additional stabilization of structural architectures. However, it should be noted that the Equation (2) was originally proposed for hydrogen-bonded interactions and its applicability to closed-shell interactions is not fully justified. It is also of interest that the presence of the Se–Cl bonding interactions may at least in part explain the bond-valence deficiency frequently observed for Cl^- anions in natural selenite chlorides [22,42,47,48]. Our conclusion about the closed-shell nature of the Se–Cl interactions is also supported by the fact that the total net charges on Se atoms (calculated for sofiite and georgbokiite) are in the range of +6.05–6.07, which indicates that there is no correlation between these values and the number of Se–Cl interactions per Se^{4+} cation.

Thus, the existence of the large number of selenite chlorides and almost complete absence of selenate chlorides can be explained by the tendency of Se^{4+} cations possessing a lone electron pair to participate in attractive Se^{4+}–Cl^{-} interactions, which cannot be realized in Se^{6+} oxysalts. Though weak, these interactions seem to be of crucial importance for the stabilization of structural architectures with relatively hard intermediate metal–oxide interactions and relatively soft closed-shell interactions. The Se^{4+}–Cl^{-} configurations are localized inside framework channels or cavities, which can be therefore be viewed as regions of weak and soft interactions in the structure.

Author Contributions: Sergey V. Krivovichev conceived the idea of the manuscript; Sergey V. Krivovichev and Liudmila A. Gorelova performed the calculations and analyzed the data; Sergey V. Krivovichev wrote the paper.

Acknowledgments: We are grateful to three anonymous referees for very useful comments on the first version of this manuscript. This research was supported by the Russian Science Foundation (Grant 14–17-00071 to Sergey V. Krivovichev).

Conflicts of Interest: The authors declare no conflict of interest.

References

1. Hellenbrandt, M. The Inorganic Crystal Structure Database (ICSD)—Present and future. *Crystallogr. Rev.* **2004**, *10*, 17–22. [CrossRef]
2. Millet, P.; Bastide, B.; Pashchenko, V.; Gnatchenko, S.; Gapon, V.; Ksarid, Y.; Stepanov, A. Syntheses, crystal structures and magnetic properties of francisite compounds $Cu_3Bi(SeO_3)_2O_2X$ (X = Cl, Br and I). *J. Mater. Chem.* **2001**, *11*, 1152–1157. [CrossRef]
3. Shen, Y.-L.; Mao, J.-G.; Jiang, H.-L. Synthesis, crystal structure and magnetic property of a new nickel selenite chloride: $Ni_5(SeO_3)_4Cl_2$. *J. Solid State Chem.* **2005**, *178*, 2942–2946. [CrossRef]
4. Becker, R.; Prester, M.; Berger, H.; Lin, P.H.; Johnsson, M.; Drobac, D.; Zivkovic, I. Crystal structure and magnetic properties of two new cobalt selenite halides: $Co_5(SeO_3)_4X_2$ (X = Cl, Br). *J. Solid State Chem.* **2007**, *180*, 1051–1059. [CrossRef]
5. Zhang, D.; Berger, H.; Kremer, R.K.; Wulferding, D.; Lemmens, P.; Johnsson, M. Synthesis, crystal structure, and magnetic properties of the copper selenite chloride $Cu_5(SeO_3)_4Cl_2$. *Inorg. Chem.* **2010**, *49*, 9683–9688. [CrossRef] [PubMed]
6. Berdonosov, P.S.; Janson, O.; Olenev, A.V.; Krivovichev, S.V.; Rosner, H.; Dolgikh, V.A.; Tsirlin, A.A. Crystal structures and variable magnetism of $PbCu_2(XO_3)_2Cl_2$ with X = Se, Te. *Dalton Trans.* **2013**, *42*, 9547–9554. [CrossRef] [PubMed]
7. Berdonosov, P.S.; Kuznetsova, E.S.; Dolgikh, V.A.; Sobolev, A.V.; Presniakov, I.A.; Olenev, A.V.; Rahaman, B.; Saha-Dasgupta, T.; Zakharov, K.V.; Zvereva, E.A.; et al. Crystal structure, physical properties, and electronic and magnetic structure of the spin $S = 5/2$ zigzag chain compound $Bi_2Fe(SeO_3)_2OCl_3$. *Inorg. Chem.* **2014**, *53*, 5830–5838. [CrossRef] [PubMed]
8. Zakharov, K.V.; Zvereva, E.A.; Berdonosov, P.S.; Kuznetsova, E.S.; Dolgikh, V.A.; Clark, L.; Black, C.; Lightfoot, P.; Kockelmann, W.; Pchelkina, Z.V.; et al. Thermodynamic properties, electron spin resonance, and underlying spin model in $Cu_3Y(SeO_3)_2O_2Cl$. *Phys. Rev. B* **2014**, *90*, 214417. [CrossRef]
9. Markina, M.M.; Zakharov, K.V.; Zvereva, E.A.; Denisov, R.S.; Berdonosov, P.S.; Dolgikh, V.A.; Kuznetsova, E.S.; Olenev, A.V.; Vasiliev, A.N. Static and dynamic magnetic properties of two synthetic francisites $Cu_3La(SeO_3)_2O_2X$ (X = Br and Cl). *Phys. Chem. Miner.* **2017**, *44*, 277–285. [CrossRef]
10. Badrtdinov, D.I.; Kuznetsova, E.S.; Verchenko, V.Y.; Berdonosov, P.S.; Dolgikh, V.A.; Mazurenko, V.V.; Tsirlin, A.A. Magnetism of coupled spin tetrahedra in ilinskite-type $KCu_5O_2(SeO_3)_2Cl_3$. *Sci. Rep.* **2018**, *8*, 2379. [CrossRef] [PubMed]
11. Berdonosov, P.S.; Kuznetsova, E.S.; Dolgikh, V.A. Transition metal selenite halides: A fascinating family of magnetic compounds. *Crystals* **2018**, *8*, 159. [CrossRef]
12. Vergasova, L.P.; Filatov, S.K.; Semenova, T.F.; Filosofova, T.M. Sofiite $Zn_2(SeO_3)Cl_2$—A new mineral from volcanic sublimates. *Zap. Vses. Mineral. Obshch.* **1989**, *118*, 65–69. (In Russian)
13. Pring, A.; Gatehouse, B.M.; Birch, W.D. Francisite, $Cu_3Bi(SeO_3)_2O_2Cl$, new mineral from Iron Monarch, South Australia: Description and crystal structure. *Am. Mineral.* **1990**, *75*, 1421–1425.

14. Vergasova, L.P.; Semenova, T.F.; Shuvalov, R.R.; Filatov, S.K.; Anan'yev, V.V. Ilinskite $NaCu_5O_2(SeO_3)_2Cl_3$—A new mineral of volcanic exhalations. *Dokl. Akad. Nauk* **1997**, *353*, 641–644. (In Russian)
15. Vergasova, L.; Krivovichev, S.; Semenova, T.; Filatov, S.; Ananiev, V. Chloromenite, $Cu_9O_2(SeO_3)_4Cl_6$, a new mineral from the Tolbachik volcano, Kamchatka, Russia. *Eur. J. Mineral.* **1999**, *11*, 119–123. [CrossRef]
16. Vergasova, L.P.; Semenova, T.F.; Filatov, S.K.; Krivovichev, S.V.; Shuvalov, R.R.; Ananiev, V.V. Georgbokiite $Cu_5O_2(SeO_3)_2Cl_2$—A new mineral from volcanic sublimates. *Dokl. Akad. Nauk* **1999**, *364*, 527–531. (In Russian)
17. Campostrini, I.; Gramaccioli, C.M.; Demartin, F. Orlandiite, $Pb_3Cl_4(SeO_3)\cdot H_2O$, a new mineral species, and an associated lead-copper selenite chloride from the Baccu Locci mine, Sardinia, Italy. *Can. Mineral.* **1999**, *37*, 1493–1498.
18. Krivovichev, S.V.; Vergasova, L.P.; Starova, G.L.; Filatov, S.K.; Britvin, S.N.; Roberts, A.C.; Steele, I.M. Burnsite, $KCdCu_7O_2(SeO_3)_2Cl_9$, a new mineral species from the Tolbachik Volcano, Kamchatka Peninsula, Russia. *Can. Mineral.* **2002**, *40*, 1171–1175. [CrossRef]
19. Vergasova, L.P.; Krivovichev, S.V.; Britvin, S.N.; Filatov, S.K.; Burns, P.C.; Ananyev, V.V. Allochalcoselite, $Cu^+Cu^{2+}{}_5PbO_2(SeO_3)_2Cl_5$—A new mineral from volcanic exhalations (Kamchatka, Russia). *Zap. Ross. Mineral. Obshch.* **2005**, *134*, 70–74. (In Russian)
20. Vergasova, L.P.; Krivovichev, S.V.; Filatov, S.K.; Britvin, S.N.; Burns, P.C.; Ananyev, V.V. Parageorgbokiite, β-$Cu_5O_2(SeO_3)_2Cl_2$—A new mineral from volcanic exhalations (Kamchatka peninsula, Russia). *Zap. Ross. Mineral. Obshch.* **2006**, *135*, 24–28. [CrossRef]
21. Gemmi, M.; Campostrini, I.; Demartin, F.; Gorelik, T.E.; Gramaccioli, C.M. Structure of the new mineral sarrabusite, $Pb_5CuCl_4(SeO_3)_4$, solved by manual electron-diffraction tomography. *Acta Crystallogr.* **2012**, *B68*, 15–23. [CrossRef] [PubMed]
22. Shuvalov, R.R.; Vegasova, L.P.; Semenova, T.F.; Filatov, S.K.; Krivovichev, S.V.; Siidra, O.I.; Rudashevsky, N.S. Prewittite, KPb1.5Cu6Zn(SeO3)2O2Cl10, a new mineral from Tolbachik fumaroles, Kamchatka peninsula, Russia: Description and crystal structure. *Am. Mineral.* **2013**, *98*, 463–469. [CrossRef]
23. Vergasova, L.P.; Semenova, T.F.; Krivovichev, S.V.; Filatov, S.K.; Zolotarev, A.A., Jr.; Ananiev, V.V. Nicksobolevite, $Cu_7(SeO_3)_2O_2Cl_6$, a new complex copper oxoselenite chloride from Tolbachik fumaroles, Kamchatka peninsula, Russia. *Eur. J. Mineral.* **2014**, *26*, 439–449. [CrossRef]
24. Johnsson, M.; Tornroos, K.W.; Lemmens, P.; Millet, P. Crystal structure and magnetic properties of a new two-dimensional $S = 1$ quantum system $Ni_5(TeO_3)_3X_2$ (X = Cl, Br). *Chem. Mater.* **2003**, *15*, 68–73. [CrossRef]
25. Bader, R.F.W. *Atoms in Molecules*; Oxford Science Publications: Oxford, UK, 1990; ISBN 9780198558651.
26. Gatti, C. Chemical bonding in crystals: New directions. *Z. Kristallogr.* **2005**, *220*, 399–457. [CrossRef]
27. Espinosa, E.; Alkorta, I.; Elguero, J.; Molins, E. From weak to strong interactions: A comprehensive analysis of the topological and energetic properties of the electron density distribution involving X–H$\cdots$ F–Y systems. *J. Chem. Phys.* **2002**, *117*, 5529–5542. [CrossRef]
28. Pendás, A.M.; Costales, A.; Luaña, V. Ions in crystals: The topology of the electron density in ionic materials. I. Fundamentals. *Phys. Rev. B* **1997**, *55*, 4275. [CrossRef]
29. Vegas, A.; Santamaria-Perez, D.; Marques, M.; Florez, M.; Garcia-Baonza, V.; Recio, J.M. Anions in metallic matrices model: Application to the aluminium crystal chemistry. *Acta Crystallogr.* **2006**, *B62*, 220–227. [CrossRef] [PubMed]
30. Dunitz, J.D. Intermolecular atom-atom bonds in crystals? *IUCrJ* **2015**, *2*, 157–158. [CrossRef] [PubMed]
31. Lecomte, C.; Espinosa, E.; Matta, C.F. On atom-atom 'short contact' bonding interactions in crystals. *IUCrJ* **2015**, *2*, 161–163. [CrossRef] [PubMed]
32. Nelyubina, Y.V.; Antipin, M.Y.; Lyssenko, K.A. Anion–anion interactions: Their nature, energy and role in crystal formation. *Russ. Chem. Rev.* **2010**, *79*, 167–187. [CrossRef]
33. Gibbs, G.V.; Downs, R.T.; Cox, D.F.; Ross, N.L.; Boisen, M.B., Jr.; Rosso, K.M. Shared and closed-shell O–O interactions in silicates. *J. Phys. Chem. A* **2008**, *112*, 3693–3699. [CrossRef] [PubMed]
34. Gibbs, G.V.; Wallace, A.F.; Cox, D.F.; Dove, P.M.; Downs, R.T.; Ross, N.L.; Rosso, K.M. Role of directed van der Waals bonded interactions in the determination of the structures of molecular arsenate solids. *J. Phys. Chem. A* **2009**, *113*, 736–749. [CrossRef] [PubMed]
35. Gibbs, G.V.; Wallace, A.F.; Zallen, R.; Downs, R.T.; Ross, N.L.; Cox, D.F.; Rosso, K.M. Bond paths and van der Waals interactions in orpiment, As_2S_3. *J. Phys. Chem. A* **2010**, *114*, 6550–6557. [CrossRef] [PubMed]

36. Gibbs, G.V.; Wallace, A.F.; Downs, R.T.; Ross, N.L.; Cox, D.F.; Rosso, K.M. Thioarsenides: A case for long-range Lewis acid–base-directed van der Waals interactions. *Phys. Chem. Miner.* **2011**, *38*, 267–291. [CrossRef]
37. Krivovichev, S.V.; Burns, P.C. Crystal chemistry of lead oxide chlorides. I. Crystal structures of synthetic mendipite, $Pb_3O_2Cl_2$, and synthetic damaraite, $Pb_3O_2(OH)Cl$. *Eur. J. Mineral.* **2001**, *13*, 801–809. [CrossRef]
38. Krivovichev, S.V.; Armbruster, T.; Depmeier, W. Crystal structures of $Pb_8O_5(AsO_4)_2$ and $Pb_5O_4(CrO_4)$, and review of PbO-related structural units in inorganic compounds. *J. Solid State Chem.* **2004**, *177*, 1321–1332. [CrossRef]
39. Krivovichev, S.V.; Siidra, O.I.; Nazarchuk, E.V.; Burns, P.C.; Depmeier, W. Particular topological complexity of lead oxide blocks in $Pb_{31}O_{22}X_{18}$ (X = Br, Cl). *Inorg. Chem.* **2006**, *45*, 3846–3848. [CrossRef] [PubMed]
40. Krivovichev, S.V.; Armbruster, T.; Depmeier, W. One-dimensional lone electron pair micelles in the crystal structure of $Pb_5(SiO_4)(VO_4)_2$. *Mater. Res. Bull.* **2004**, *39*, 1717–1722. [CrossRef]
41. Krivovichev, S.V.; Burns, P.C. Crystal chemistry of uranyl molybdates. VIII. Crystal structures of $Na_3Tl_3[(UO_2)(MoO_4)_4]$, $Na1_3Tl_3[(UO_2)(MoO_4)_3]_4(H_2O)_5$, $Na_3Tl_5[(UO_2)(MoO_4)_3]_2(H_2O)_3$ and $Na_2[(UO_2)(MoO_4)_2](H_2O)_4$. *Can. Mineral.* **2003**, *41*, 707–719. [CrossRef]
42. Krivovichev, S.V.; Filatov, S.K.; Burns, P.C.; Vergasova, L.P. The crystal structure of allochalcoselite, $Cu^+Cu^{2+}{}_5PbO_2(SeO_3)_2Cl_5$, a mineral with well-defined Cu^+ and Cu^{2+} positions. *Can. Miner.* **2006**, *44*, 507–514. [CrossRef]
43. Krivovichev, S.V.; Filatov, S.K.; Vergasova, L.P. The crystal structure of ilinskite, $NaCu_5O_2(SeO_3)_2Cl_3$, and review of mixed-ligand CuO_mCl_n coordination geometries in minerals and inorganic compounds. *Miner. Petrol.* **2013**, *107*, 235–242. [CrossRef]
44. Semenova, T.F.; Rozhdestvenskaya, I.V.; Filatov, S.K.; Vergasova, L.P. Crystal structure and physical properties of sophiite, $Zn_2(SeO_3)Cl_2$, a new mineral. *Mineral. Mag.* **1992**, *56*, 241–245. [CrossRef]
45. Johnsson, M.; Tornroos, K.W. Zinc selenium oxochloride, β-$Zn_2(SeO_3)Cl_2$, a synthetic polymorph of the mineral sophiite. *Acta Crystallogr. C* **2007**, *63*, i34–i36. [CrossRef] [PubMed]
46. Krivovichev, S.V.; Shuvalov, R.R.; Semenova, T.F.; Filatov, S.K. Crystal chemistry of inorganic compounds based on chains of oxocentered tetrahedra. III. Crystal structure of georgbokiite, $Cu_5O_2(SeO_3)_2Cl_2$. *Z. Kristallogr.* **1999**, *214*, 135–138. [CrossRef]
47. Krivovichev, S.V.; Filatov, S.K.; Burns, P.C.; Vergasova, L.P. The crystal structure of parageorgbokiite, β-$Cu_5O_2(SeO_3)_2Cl_2$. *Can. Mineral.* **2007**, *45*, 929–934. [CrossRef]
48. Burns, P.C.; Krivovichev, S.V.; Filatov, S.K. New Cu^{2+} coordination polyhedra in the crystal structure of burnsite, $KCdCu_7O_2(SeO_3)_2Cl_9$. *Can. Mineral.* **2002**, *40*, 1587–1595. [CrossRef]
49. Dovesi, R.; Orlando, R.; Erba, A.; Zicovich-Wilson, C.M.; Civalleri, B.; Casassa, S.; Maschio, L.; Ferrabone, M.; De La Pierre, M.; D'Arco, P.; et al. CRYSTAL14: A program for *ab initio* investigation of crystalline solids. *Int. J. Quantum Chem.* **2014**, *114*, 1287–1317. [CrossRef]
50. Peintinger, M.F.; Oliveira, D.V.; Bredow, T. Consistent Gaussian basis sets of triple-zeta valence with polarization quality for solid-state calculations. *J. Comput. Chem.* **2013**, *34*, 451–459. [CrossRef] [PubMed]
51. Dou, Y.; Egdell, R.G.; Law, D.S.L.; Harrison, N.M.; Searle, B.G. An experimental and theoretical investigation of the electronic structure of CdO. *J. Phys. Condens. Matter* **1998**, *10*, 8447–8458. [CrossRef]
52. Gatti, C.; Casassa, S. *TOPOND14. User's Manual*; CNR-ISTM of Milano: Milano, Italy, 2013.
53. Gatti, C.; Saunders, V.R.; Roetti, C. Crystal field effects on the topological properties of the electron density in molecular crystals. The case of urea. *J. Chem. Phys.* **1994**, *101*, 10686–10696. [CrossRef]
54. Kovrugin, V.M.; Siidra, O.I.; Colmont, M.; Mentré, O.; Krivovichev, S.V. Emulating exhalative chemistry: Synthesis and structural characterization of ilinskite, $Na[Cu_5O_2](SeO_3)_2Cl_3$, and its K-analogue. *Miner. Petrol.* **2015**, *109*, 421–430. [CrossRef]
55. Galy, J.; Bonnet, J.J.; Andersson, S. The crystal structure of a new oxide chloride of copper(II) and selenium(IV) $Cu_5Se_2O_8Cl_2$. *Acta Chem. Scand.* **1979**, *A33*, 383–389. [CrossRef]
56. Bergerhoff, G.; Paeslack, J. Sauerstoff als Koordinationszentrum in Kristallstrukturen. *Z. Kristallogr.* **1968**, *126*, 112–123. [CrossRef]
57. Krivovichev, S.V.; Mentré, O.; Siidra, O.I.; Colmont, M.; Filatov, S.K. Anion-centered tetrahedra in inorganic compounds. *Chem. Rev.* **2013**, *113*, 6459–6535. [CrossRef] [PubMed]
58. Krivovichev, S.V. Structure description, interpretation and classification in mineralogical crystallography. *Crystallogr. Rev.* **2017**, *23*, 2–71. [CrossRef]

59. Haas, H.; Jansen, M. Synthese und Charakterisierung von Na_5AsO_5. *Z. Anorg. Allg. Chem.* **2001**, *627*, 1013–1016. [CrossRef]
60. Krivovichev, S.V. Minerals with antiperovskite structure: A review. *Z. Kristallogr.* **2008**, *223*, 109–113. [CrossRef]
61. Reckeweg, O.; Blaschkowski, B.; Schleid, T. Li_5OCl_3 and Li_3OCl: Two remarkably different lithium oxide chlorides. *Z. Anorg. Allg. Chem.* **2012**, *638*, 2081–2086. [CrossRef]
62. Nuss, J.; Muehle, C.; Hayama, K.; Abdolazimi, V.; Takagi, H. Tilting structures in inverse perovskites, M_3TtO (M = Ca, Sr, Ba, Eu; Tt = Si, Ge, Sn, Pb). *Acta Crystallogr.* **2015**, *B71*, 300–312. [CrossRef]
63. Galuskin, E.V.; Gfeller, F.; Armbruster, T.; Galuskina, I.O.; Vapnik, Y.; Murashko, M.; Włodyka, R.; Dzierżanowski, P. New minerals with a modular structure derived from hatrurite from the pyrometamorphic Hatrurim Complex. Part I. Nabimusaite, $KCa_{12}(SiO_4)_4(SO_4)_2O_2F$, from larnite rocks of Jabel Harmun, Palestinian Autonomy, Israel. *Mineral. Mag.* **2015**, *79*, 1061–1072. [CrossRef]
64. Galuskin, E.V.; Gfeller, F.; Galuskina, I.O.; Pakhomova, A.; Armbruster, T.; Vapnik, Y.; Włodyka, R.; Dzierżanowski, P.; Murashko, M. New minerals with a modular structure derived from hatrurite from the pyrometamorphic Hatrurim Complex. Part II. Zadovite, $BaCa_6[(SiO_4)(PO_4)](PO_4)_2F$ and aradite, $BaCa_6[(SiO_4)(VO_4)](VO_4)_2F$, from paralavas of the Hatrurim Basin, Negev Desert, Israel. *Mineral. Mag.* **2015**, *79*, 1073–1087. [CrossRef]
65. Oudah, M.; Ikeda, A.; Hausmann, J.N.; Yonezawa, S.; Fukumoto, T.; Kobayashi, S.; Sato, M.; Maeno, Y. Superconductivity in the antiperovskite Dirac-metal oxide $Sr_{3-x}SnO$. *Nat. Commun.* **2016**, *12*, 13617. [CrossRef] [PubMed]
66. Lai, K.T.; Antonyshyn, I.; Prots, Y.; Valldor, M. Anti-perovskite Li-battery cathode materials. *J. Am. Chem. Soc.* **2017**, *139*, 9645–9649. [CrossRef] [PubMed]
67. Krivovichev, S.V.; Starova, G.L.; Filatov, S.K. "Face-to-face" relationships between oxocentered tetrahedra and cation-centered tetrahedral oxyanions in crystal structures of minerals and inorganic compounds. *Mineral. Mag.* **1999**, *63*, 263–266. [CrossRef]
68. Krivovichev, S.V.; Filatov, S.K. Structural principles for minerals and inorganic compounds containing anion-centered tetrahedra. *Am. Mineral.* **1999**, *84*, 1099–1106. [CrossRef]
69. Jahn, H.A.; Teller, E. Stability of polyatomic molecules in degenerate electronic states. I. Orbital degeneracy. *Proc. R. Soc. A* **1937**, *A161*, 220–235. [CrossRef]
70. Brown, I.D. *The Chemical Bond in Inorganic Chemistry. The Bond Valence Model*, 2nd ed.; Oxford University Press: Oxford, UK, 2016; ISBN 9780198742951.
71. Semenova, T.F.; Pankratova, O.Y.; Habanova, A.A.; Shuvalov, R.R. Synthesis of exhalation copper selenites analogues by chemical gas transport reactions method. *Vestnik Sankt-Peterb. Univ. Ser. 4 Fiz. Khim.* **2005**, *2*, 75–81. (In Russian)
72. Kovrugin, V.M.; Colmont, M.; Mentré, O.; Siidra, O.I.; Krivovichev, S.V. Dimers of oxocentred $[OCu_4]^{6+}$ tetrahedra in two novel copper selenite chlorides, $K[Cu_3O](SeO_3)_2Cl$ and $Na_2[Cu_7O_2](SeO_3)_4Cl_4$, and related minerals and inorganic compounds. *Mineral Mag.* **2016**, *80*, 227–238. [CrossRef]
73. Tang, Y.; Guo, W.; Zhang, S.; Xiang, H.; Cui, M.; He, Z. $Na_2Cu_7(SeO_3)_4O_2Cl_4$: A selenite chloride compound with Cu_7 units showing spin-frustration and a magnetization plateau. *Dalton Trans.* **2016**, *45*, 8324–8326. [CrossRef] [PubMed]
74. Cavallo, G.; Metrangolo, P.; Milani, R.; Pilati, T.; Priimagi, A.; Resnati, G.; Terraneo, G. The halogen bond. *Chem. Rev.* **2016**, *116*, 2478–2601. [CrossRef] [PubMed]
75. Benz, S.; Macchione, M.; Verolet, Q.; Mareda, J.; Sakai, N.; Matile, S. Anion transport with chalcogen bonds. *J. Am. Chem. Soc.* **2016**, *138*, 9093–9096. [CrossRef] [PubMed]
76. Sánchez-Sanz, G.; Trujillo, C. Improvement of anion transport systems by modulation of chalcogen interactions: The influence of solvent. *J. Phys. Chem. A* **2018**, *122*, 1369–1377. [CrossRef] [PubMed]
77. Batsanov, S.S. Van der Waals radii of elements. *Inorg. Mater.* **2001**, *37*, 871–885. [CrossRef]
78. Espinosa, E.; Alkorta, I.; Rozas, I.; Elguero, J.; Molins, E. About the evaluation of the local kinetic, potential and total energy densities in closed-shell interactions. *Chem. Phys. Lett.* **2001**, *336*, 457–461. [CrossRef]
79. Desiraju, G.; Steiner, T. *The Weak Hydrogen Bond in Structural Chemistry and Biology*; Oxford University Press: Oxford, UK, 2001; ISBN 9780198509707.
80. Nelyubina, Y.V.; Antipin, M.Y.; Lyssenko, K.A. Extremely short halogen bond: The nature and energy of iodine–oxygen interactions in crystalline iodic acid. *Mendeleev Commun.* **2011**, *21*, 250–252. [CrossRef]

81. Mata, I.; Alkorta, I.; Molins, E.; Espinosa, E. Electrostatics at the origin of the stability of phosphate-phosphate complexes locked by hydrogen bonds. *ChemPhysChem* **2012**, *13*, 1421–1424. [CrossRef] [PubMed]
82. Weinhold, F.; Klein, R.A. Anti-electrostatic hydrogen bonds. *Angew. Chem. Int. Ed.* **2014**, *53*, 11214–11217. [CrossRef] [PubMed]

crystals

MDPI

Article

$Sc_2[Se_2O_5]_3$: The First Rare-Earth Metal Oxoselenate(IV) with Exclusively $[Se_2O_5]^{2-}$ Anions

Stefan Greiner and Thomas Schleid *

Institute for Inorganic Chemistry, University of Stuttgart, Pfaffenwaldring 55, 70569 Stuttgart, Germany; stefan.greiner@iac.uni-stuttgart.de

* Correspondence: schleid@iac.uni-stuttgart.de; Tel.: +49711/6856-4240

Received: 23 March 2018; Accepted: 20 April 2018; Published: 26 April 2018

Abstract: The scandium oxodiselenate(IV) $Sc_2[Se_2O_5]_3$ was synthesized via solid-state reactions between scandium sesquioxide (Sc_2O_3) and selenium dioxide (SeO_2) with thallium(I) chloride (TlCl) as fluxing agent in molar ratios of 1:4:2. Evacuated fused silica ampoules were used as reactions vessels for annealing the mixtures for five days at 800 °C. The new scandium compound crystallizes in the triclinic space group $P\bar{1}$ with the lattice parameters a = 663.71(5) pm, b = 1024.32(7) pm, c = 1057.49(8) pm, α = 81.034(2)°, β = 87.468(2)°, γ = 89.237(2)° and Z = 2. There are two distinct Sc^{3+} positions, which show six-fold coordination by oxygen atoms as $[ScO_6]^{9-}$ octahedra (d(Sc–O) = 205–212 pm). Three different $[Se_2O_5]^{2-}$ anions provide these oxygen atoms with their terminal ligands (O^t). Each of the six selenium(IV) central atoms exhibit a stereochemically active lone pair of electrons, so that all $[Se_2O_5]^{2-}$ anions consist of two ψ^1-tetrahedral $[SeO_3]^{2-}$ subunits (d(Se–O^t) = 164–167 pm, d(Se–O^b) = 176–185 pm, ∢(O–Se–O) = 93–104°) sharing one bridging oxygen atom (O^b) with ∢(Se–O^b–Se) = 121–128°. The vibrational modes of the complex anionic $[Se_2O_5]^{2-}$ entities were characterized via single-crystal Raman spectroscopy.

Keywords: scandium; lone-pair; oxoselenate; complex anions; Raman spectroscopy; solid-state reactions

1. Introduction

Owing to their potential as materials with an inorganic antenna effect [1] within energy transfer processes for lighting applications, many rare-earth metal(III) oxoselenates(IV) were published with different structural characteristics in the past decades. So even the pure rare-earth metal(III) oxoselenates(IV) with the simple formula $RE_2[SeO_3]_3$ (≡ $RE_2Se_3O_9$; RE = Sc, Y, La–Lu) [2–12] show a cornucopia of structure and space-group types. For the smallest rare-earth metal, scandium $Sc_2[SeO_3]_3$ crystallizes in a hexagonal crystal structure in space group $P6_3/m$ [3]. In contrast, the $RE_2[SeO_3]_3$-type phases with lanthanum and cerium show an orthorhombic structure in space-group $Pnma$ [2,4]. The next two lanthanides, praseodymium and neodymium, exhibit for their $RE_2[SeO_3]_3$ compounds the monoclinic crystal system with the space group $P2_1/n$ [2,8]. All further rare-earth metals(III) (RE = Y, Sm–Lu) [6,7,10] adopt the same triclinic crystal structure for their $RE_2[SeO_3]_3$-type representatives with space-group $P\bar{1}$. Besides this formula type, representatives containing oxygen atoms not bonded to the Se^{4+} cations are known with the formula $RE_2O[SeO_3]_2$ (≡ $RE_2Se_2O_7$; RE = Y, Sm–Tm) [13–16]. Most of the compounds crystallize in the tetragonal $Tb_2O[SeO_3]_2$ structure-type [16], but the newest experimental research shows that monoclinic $Sm_3O_2Sm[SeO_3]_4$ (≡ $Sm_2Se_2O_7$) is also accessible [15]. All these compounds exhibit the same basic module, which is responsible for the crystal structure, and these basic modules are oxygen-centered $[ORE_4]^{10+}$ tetrahedra, which are interconnected in different ways. Furthermore, in the literature is a rare-earth metal(III) oxoselenate(IV) known with two 'free' oxygen atoms per formula unit and the composition $Sc_2O_2[SeO_3]$ [17,18]. This formula type $RE_2O_2[SeO_3]$ (≡ RE_2SeO_5) was long

postulated from *Oppermann* et al. [19–23] in various RE_2O_3/SeO_2 systems. Nevertheless, no single crystals were available to confirm this crystal structure, so it was only assumed via powder diffraction methods [19–23]. Only one representative, including rare-earth metals, is known so far in the literature, which exhibits complex anionic $[Se_2O_5]^{2-}$ units. $Sm_2[SeO_3][Se_2O_5]_2$ ($\equiv Sm_2Se_5O_{13}$) [24] contains only two of these anions, while with the title compound the first rare-earth metal(III) oxoselenate(IV) was accessible with exclusively these sort of anions. The aim of the synthesis was a $TlSc[SeO_3]_2$, however, which should be structurally similar to the alkali-metal scandium oxoselenates(IV) $ASc[SeO_3]_2$ (A = Na–Cs) [25] known in the literature. This paper describes the crystal structure of the new title compound $Sc_2[Se_2O_5]_3$ as well as the vibrational modes of the $[Se_2O_5]^{2-}$ groups via single-crystal Raman measurements.

2. Materials and Methods

For the synthesis of the scandium oxodiselenate(IV) $Sc_2[Se_2O_5]_3$ a mixture of Sc_2O_3 (ChemPur: 99.9%), SeO_2 (ChemPur: 99.9%) and TlCl (Alfa Aesar: 'pure') in a molar ratio of 1:4:2 was used. The target product was thus $TlSc[SeO_3]_2$ according to the known alkali-metal scandium oxoselenates(IV) $ASc[SeO_3]_2$ (A = Na–Cs) [25]. The chemicals were stored and handled in a glove box (GS Glove-Box Systems) under an argon atmosphere. The reactants were filled into glassy fused silica ampoules, which were evacuated to 10^{-3} mbar and torch sealed. Afterwards, the reaction vessels were heated up over 8 h to 800 °C and tempered for five days at this temperature. The furnace was cooled down to 500 °C within 99 h, and held at this temperature for another 2 h, before it was completely cooled down within 4 h to room temperature. The crude product was checked for its water- and air-stability. Afterwards it was washed with demineralized water to remove most of the fluxing agents (SeO_2 and TlCl). Some colorless, plate-like crystals were selected and characterized via X-ray structure analysis. For this purpose, the crystals were measured at room temperature on a κ-CCD X-ray diffractometer (Bruker Nonius, Karlsruhe, Germany) with graphite-monochromatized Mo-Kα radiation (λ = 71.07 pm). A numerical absorption correction was carried out with the program HABITUS [26], but the structure solution and refinement was performed with the program SHELX-97 [27,28]. In Table 1 the crystallographic data of $Sc_2[Se_2O_5]_3$ are summarized, while Table 2 contains the atomic positions and their equivalent isotropic displacement coefficients. The interatomic distances and bond angles are shown in Table 3.

The reflections in the X-ray powder pattern (Figure 1) exhibit a low intensity due to the poor crystallinity of the product, therefore a good evaluation and characterization was not possible (Figure 1). However, scandium oxoselenate(IV) $Sc_2[SeO_3]_3$ and some residual thallium(I) chloride TlCl could be identified as by-products. In addition, the powder pattern shows reflections of another side phase, which could not be determined so far. Hence, a successful synthesis of the phase pure title compound $Sc_2[Se_2O_5]_3$ was not successful yet.

The single-crystal Raman measurements were operated on a XploRa device (Horiba, Bensheim, Germany) from 200–1000 cm^{-1} to detect the vibrational modes of the complex anionic $[Se_2O_5]^{2-}$ anions. Further details of the crystal structure investigations can be obtained at the Fachinfomrationszentrum Karlsruhe, 76334 Eggenstein-Leopoldshafen, Germany (Fax: +49-7247-808-666; E-Mail: crysdata@fiz-karlsruhe.de, http://www.fiz-karlsruhe.de/requestfordepositeddata.html) for the depository number CSD-433355 of $Sc_2[Se_2O_5]_3$.

Table 1. Crystallographic data of $Sc_2[Se_2O_5]_3$ and their determination.

Empirical Formula	**$Sc_2[Se_2O_5]_3$ ($\equiv Sc_2Se_6O_{15}$)**
Crystal system	triclinic
Space group	$P\bar{1}$ (no. 2)
Lattice parameters	
a/pm	663.71(5)
b/pm	1024.32(7)
c/pm	1057.49(8)
α/deg	81.034(2)
β/deg	87.468(2)
γ/deg	89.237(2)
Number of formula units (Z)	2
Calculated density (D_x in g/cm^3)	3.762
Molar volume (V_m in cm^3/mol)	188.58(9)
Diffractometer	κ-CCD (Bruker Nonius)
Wavelength (λ in pm)	71.07 (Mo Kα)
Index range ($\pm h_{max}$, $\pm k_{max}$, $\pm l_{max}$)	8/13/13
Number of e$^-$ per unit cell (F(000))	732
Absorption coefficient (μ in mm^{-1})	16.426
Number of collected vs. unique reflections	31217/3256
Data-set residuals (R_{int}/R_σ)	0.084/0.036
Structure residuals (R_1/wR_2)	0.034/0.074
Goodness of fit (GooF)	1.058
Extinction coefficient (g)	0.0101(5)
Residual electron density (max./min. in e$^-$ 10^{-6} pm^{-3})	1.318/−1.267
CSD-number	433,355

Table 2. Atomic coordinates and equivalent isotropic displacement coefficients (U_{eq}/pm^2) for $Sc_2[Se_2O_5]_3$ (all atoms occupy the general 2*i* site)

Atom	***x*/*a***	***y*/*b***	***z*/*c***	U_{eq} [1]
Sc1	0.16448(9)	0.58715(7)	0.26677(7)	145(2)
Sc2	0.31102(9)	0.06071(7)	0.28974(7)	143(2)
Se1	0.22321(5)	0.77750(4)	0.51356(4)	173(1)
Se2	0.31368(5)	0.30185(4)	0.49159(4)	156(1)
Se3	0.14680(5)	0.33785(4)	0.08075(4)	197(1)
Se4	0.34062(5)	0.46713(4)	0.80898(4)	189(1)
Se5	0.20134(5)	0.01376(4)	0.77299(4)	171(1)
Se6	0.32216(5)	0.85034(4)	0.04488(4)	173(1)
O1	0.3565(4)	0.8834(3)	0.4083(3)	257(6)
O2	0.1123(4)	0.6849(3)	0.4203(3)	241(6)
O3	0.4252(4)	0.6720(3)	0.5744(3)	229(6)
O4	0.2120(4)	0.4093(3)	0.3801(3)	245(6)
O5	0.2599(4)	0.1567(3)	0.4489(3)	210(6)
O6	0.3013(4)	0.2435(3)	0.1727(3)	288(7)
O7	0.1988(4)	0.4927(3)	0.1010(3)	289(7)
O8	0.2873(4)	0.3302(3)	0.9362(3)	354(8)
O9	0.1421(4)	0.4542(3)	0.7240(3)	308(7)
O10	0.4805(4)	0.6157(3)	0.2594(3)	241(6)
O11	0.0055(4)	0.0288(3)	0.2913(3)	289(7)
O12	0.3733(4)	0.9148(3)	0.7186(3)	227(6)
O13	0.1454(4)	0.9259(3)	0.9300(3)	346(8)
O14	0.3719(4)	0.9735(3)	0.1228(3)	288(7)
O15	0.1445(4)	0.7649(3)	0.1370(3)	229(6)

[1] defined as temperature factor according to: $\exp[-2\pi^2(U_{11}h^2a^{*2} + U_{22}k^2b^{*2} + U_{33}l^2c^{*2} + 2U_{13}hla^*c^* + 2U_{12}hka^*b^* + 2U_{23}klb^*c^*)]$.

Table 3. Selected interatomic distances (d/pm) and angles ($\sphericalangle$/°) in the crystal structure of $Sc_2[Se_2O_5]_3$.

Sc1–O4	204.7(3)	Sc2–O11	205.7(3)
Sc1–O2	205.1(3)	Sc1–O1	206.7(3)
Sc1–O9	207.9(3)	Sc1–O6	207.9(3)
Sc1–O15	210.9(3)	Sc1–O5	209.1(3)
Sc1–O10	211.8(3)	Sc1–O12	211.0(3)
Sc1–O7	213.3(3)	Sc1–O14	212.1(3)
Se1–O1	166.1(3)	Se2–O4	164.4(3)
Se1–O2	167.0(3)	Se1–O5	166.7(3)
Se1–O3	178.9(3)	Se1–O3	184.6(3)
Se3–O6	164.3(3)	Se4–O9	164.5(3)
Se1–O7	167.6(3)	Se1–O10	165.6(3)
Se1–O8	176.7(3)	Se1–O8	181.3(3)
Se5–O11	165.2(3)	Se6–O14	165.5(3)
Se1–O12	166.0(3)	Se1–O15	166.3(6)
Se1–O13	178.7(3)	Se1–O13	180.6(3)
O1–Se1–O3	098.52(13)	O3–Se2–O4	095.05(13)
O2–Se1–O3	101.80(14)	O3–Se2–O5	101.58(14)
O1–Se1–O2	102.67(14)	O4–Se2–O5	103.23(14)
O6–Se3–O8	095.50(15)	O8–Se4–O10	093.04(15)
O7–Se3–O8	099.83(15)	O8–Se4–O9	098.24(16)
O6–Se3–O7	105.18(15)	O9–Se4–O10	104.03(15)
O11–Se5–O13	096.13(15)	O13–Se6–O15	093.44(13)
O12–Se5–O13	100.96(15)	O13–Se6–O14	102.13(15)
O11–Se5–O12	102.11(14)	O14–Se6–O15	103.96(15)
Se1–O3–Se2	121.32(14)	Se3–O8–Se4	126.31(18)
Se5–O13–Se6	127.48(17)		

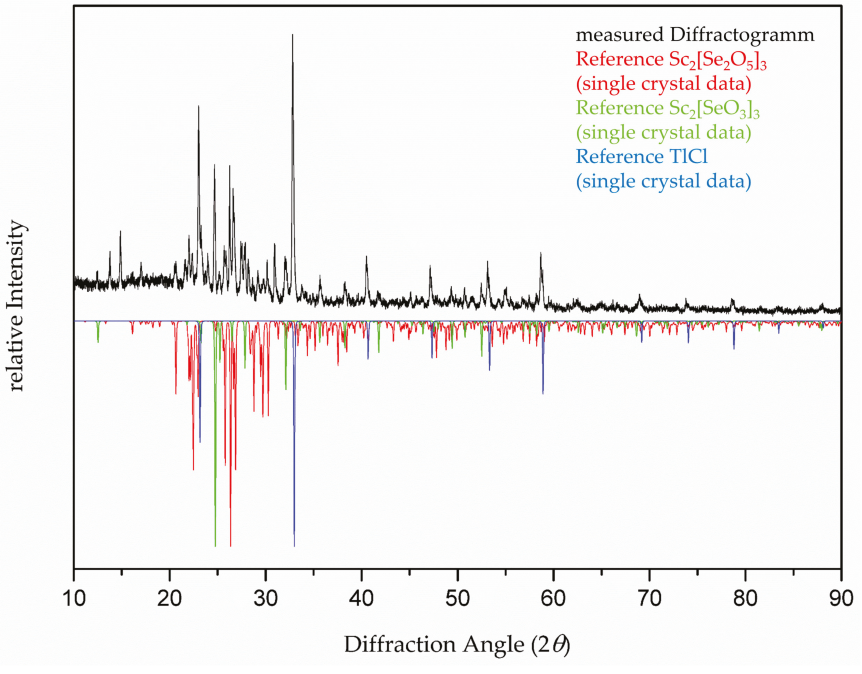

Figure 1. Measured powder pattern of the title compound (black) with the reference of $Sc_2[Se_2O_5]_3$ (red), $Sc_2[SeO_3]_3$ (green), and TlCl (blue) from single crystal data.

3. Results and Discussion

The new scandium oxodiselenate(IV) $Sc_2[Se_2O_5]_3$ ($\equiv Sc_2Se_6O_{15}$) crystallizes in the triclinic space group $P\bar{1}$ (no. 2) with the lattice parameters a = 663.71(5) pm, b = 1024.32(7) pm, c = 1057.49(8) pm, α = 81.034(2)°, β = 87.468(2)°, γ = 89.237(2)°, and Z = 2 (Table 1). In the crystal structure, two distinct Sc^{3+} cations exist (Table 2). Both of them are six-fold coordinated by oxygen atoms as $[ScO_6]^{9-}$ octahedra, which belong to six terminally attached $[Se_2O_5]^{2-}$ units (Figure 2). The Sc^{3+}–O^{2-} distances range in the area of 204 to 212 pm (Table 3). These correlate well with them known from the scandium oxoselenate(IV) $Sc_2[SeO_3]_3$ (d = 201–220 pm) [3].

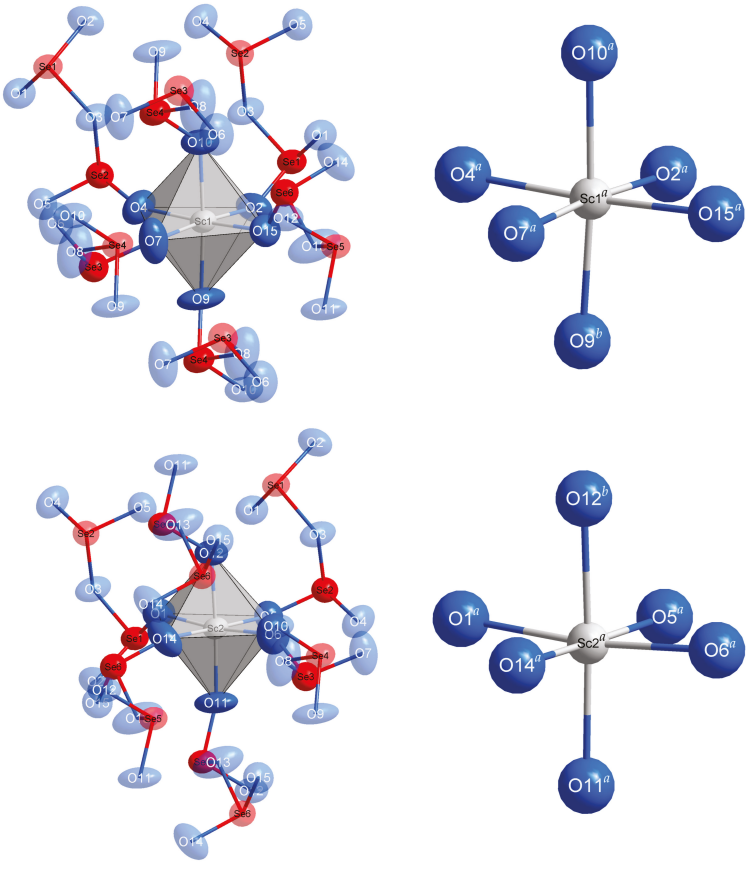

Figure 2. Coordination sphere of the two crystallographically distinct Sc^{3+}, which are six-fold coordinated by oxygen atoms as $[ScO_6]^{9-}$ octahedra ((**top left**) and (**bottom left**)). The oxygen atoms themselves belong to six terminally attached $[Se_2O_5]^{2-}$ anions. Symmetry related atoms are shown with an $^a(x, y, z)$ or $^b(-x, -y, -z)$ and a thermal ellipsoid representation with probability factor of 95% (**left**).

Moreover, three different complex anionic $[Se_2O_5]^{2-}$ groups occur in the crystal structure (Figure 3), showing different dihedral angles between the two (O,O,O)-faces ((O1,O2,O3)–(O3,O4,O5) = 121.2°; (O6,O7,O8)–(O8,O9,O10) = 146.0°; (O11,O12,O13)–(O13,O14,O15) = 152.2°). The Se^{4+}–O^{2-} distances are located in an interval from 164 to 167 pm (Table 3), this is slightly smaller than those in downeyite-type SeO_2 (d = 171–173 pm) [29]. In contrast, the Se^{4+}–$(O^b)^{2-}$ distances are significantly

longer with 177 to 185 pm. Similar distances were found in the first known lanthanoid(III) oxoselenate(IV) with $[Se_2O_5]^{2-}$ units, $Sm_2[SeO_3][Se_2O_5]_2$ ($\equiv Sm_2Se_5O_{13}$, d = 164–184 pm) [24] namely. The $[ScO_6]^{9-}$ octahedra are interconnected via the terminally grafting $[Se_2O_5]^{2-}$ units resulting in the three-dimensional network of $Sc_2[Se_2O_5]_3$ (Figure 4). The displacements of the Se^{4+} cations from their triangular (O,O,O)-plane are for all three complex anionic $[Se_2O_5]^{2-}$ anions very much alike. These displacements range from 77.3 pm (Se1), 78.3 pm (Se3), 79.4 pm (Se6), 79.5 pm (Se5), 79.7 pm (Se2), to 82.0 pm (Se4). Also the Se–O^b–Se angles are located in a small area with (Se1)–$(O3)^b$–(Se2) = 121.3°, (Se3)–$(O8)^b$–(Se4) = 126.3°, and (Se5)–$(O13)^b$–(Se6) = 127.5°.

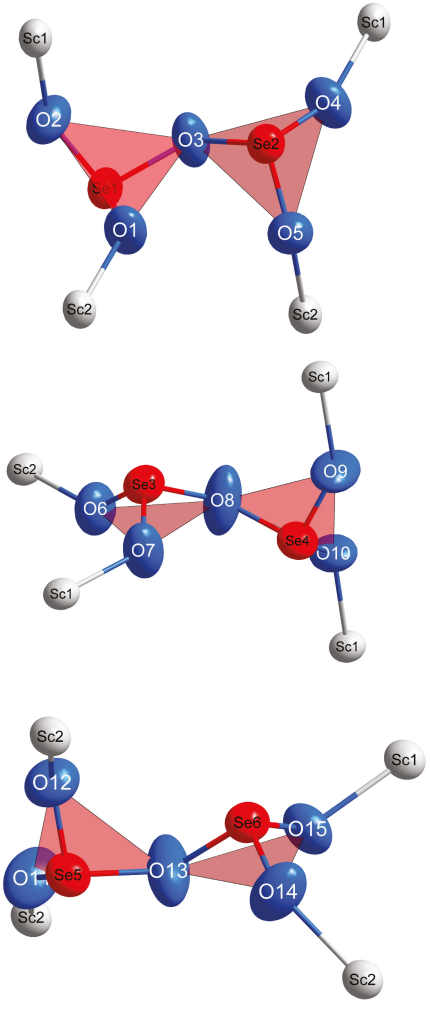

Figure 3. Configuration of the three different $[Se_2O_5]^{2-}$ groups in the crystal structure of triclinic $Sc_2[Se_2O_5]_3$. These consist of two via vertex interconnected ψ^1-tetrahedral $[SeO_3]^{2-}$ subunits with different tilting angles between their two (O,O,O)-faces. In addition, the cationic coordination sphere of the $[Se_2O_5]^{2-}$ anions is shown (thermal ellipsoid representation with probability factor of 95%). Note that none of the bridging oxygen atoms (O3, O8, and O13) has a coordinative contacts to the Sc^{3+} cations.

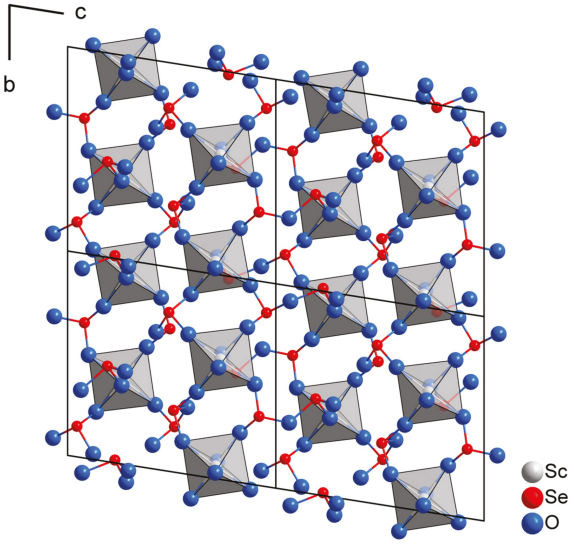

Figure 4. All $[ScO_6]^{9-}$ octahedra are interconnected by terminally attached $[Se_2O_5]^{2-}$ anions to form the three-dimensional network of triclinic $Sc_2[Se_2O_5]_3$.

Raman-spectroscopic measurements of $Sc_2[Se_2O_5]_3$ single crystals show typically modes, known from free $[SeO_3]^{2-}$ units with ψ^1-tetrahedral shape and ideal C_{3v} symmetry. These modes belong to two symmetric vibrations with A_1 at 810 and 425 cm^{-1} and E at 740 and 375 cm^{-1} according to Siebert [30]. By the influence of the crystal field these bands of the $[SeO_3]^{2-}$ anions split up into wide areas. The symmetric stretching modes are located in the range of 890–790 cm^{-1} (ν_s) and the anti-symmetric stretching modes occur between 760 and 660 cm^{-1} (ν_{as}). According to these, also the bending modes have an expanded area with the symmetric bending mode between 510 and 420 cm^{-1} (δ_s) and anti-symmetric bending mode from 410 up to 330 cm^{-1} [30]. The complex anionic oxodiselenate(IV) units generate one more stretching mode resulted from the slightly longer Se^{4+}–$(O^b)^{2-}$ bond by about 10 to 15 pm expanded. This mode is located between 650 and 550 cm^{-1} [12] and seems to be specific for $[Se_2O_5]^{2-}$ anions (ν_{SeOB}). In the Raman spectrum three signals can be detected in this area with ν = 578, 606 and 632 cm^{-1}. For the symmetric stretching mode (ν_s) two signals appear at 901 and 934 cm^{-1} and for the anti-symmetric stretching mode (ν_{as}) three at 739, 800, and 811 cm^{-1}. In the area of the symmetric bending mode ν = 420–550 cm^{-1} (δ_s) four signals can be found at 435, 469, 523, and 539 cm^{-1}. At smaller wavenumbers between 208 and 387 cm^{-1}, the anti-symmetric bending modes as well as lattices vibrations are located. Seven signals at 208, 235, 274, 292, 322, 347, and 387 cm^{-1} become obvious in these areas (Figure 5). For the characterization of these modes modern articles were used as references [11,18,31–33].

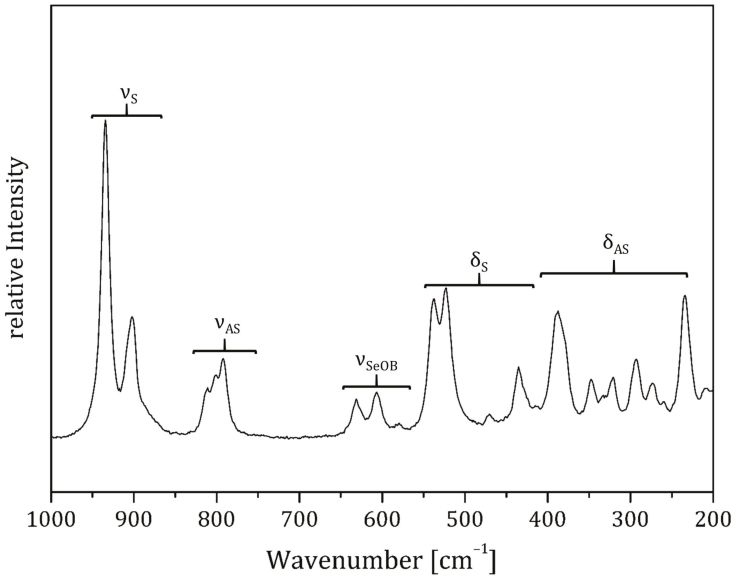

Figure 5. Single-crystal Raman spectrum of $Sc_2[Se_2O_5]_3$ in the area from 200 to 1000 cm^{-1}. The different stretching and bending modes of the complex anionic $[Se_2O_5]^{2-}$ units are shown.

4. Conclusions

Unlike yttrium, its heavier congener in group III of the periodic table of the elements, scandium hardly forms compounds suitable as hosts for doping with appropriate lanthanoid(III) cations (e.g., Eu^{3+} or Tb^{3+}) for luminescence materials. Its small ionic radius (r:(Sc^{3+}) = 74.5 pm for C.N. = 6 [34]) and its preference for octahedral coordination figures explain this finding plausibly, whereas yttrium (r:(Y^{3+}) = 101.9 pm for C.N. = 8 [34]) ranges within the heavy lanthanoid compartment (Dy^{3+}, Ho^{3+}, or Er^{3+}) under these circumstances, without being a 4*f* element. So even with nice $[SeO_3]^{2-}$ pyramids as building blocks with a lone-pair of electron at the Se^{4+} cations, scandium(III) oxoselenate(IV) derivatives are unable to host Ln^{3+} cations, as long as they contain only six-fold coordinated Sc^{3+} cations, e.g., $Sc_2[SeO_3]_3$ [3], $Sc_2O_2[SeO_3]$ [17,18] and our new example $Sc_2[Se_2O_5]_3$. However this changes, whenever the Sc^{3+} cations reside in coordination polyhedra with higher coordination numbers. In the case of $ScF[SeO_3]$ [17,18,35] and $ScCl[SeO_3]$ [17,36] with seven-fold coordinated Sc^{3+} cations in pentagonal bipyramids, Eu^{3+} cations can replace these partially (1–5%), which leads to red luminescent materials in the case of $ScF[SeO_3]:Eu^{3+}$ [17]. The tight $[ScO_5F_2]^{9-}$ polyhedra provoke a slight red-shift of the Eu^{3+}-centered luminescence, however, as compared to the $YF[SeO_3]:Eu^{3+}$ example [10] with Eu^{3+} in the eight-fold coordination of $[YO_6F_2]^{11-}$ polyhedra.

Supporting Materials: The CIF of the title compound can be downloaded directly with the publication, containing all crystallographic data.

Author Contributions: Stefan Greiner and Thomas Schleid conceived and designed the experiments; Stefan Greiner performed the experiments; Stefan Greiner and Thomas Schleid analyzed the data; Thomas Schleid contributed reagents/materials/analysis tools; Stefan Greiner wrote the paper and Thomas Schleid polished it.

Acknowledgments: We thank Sabine Strobel for the single-crystal X-ray diffraction measurement. Additionally, we are grateful to Adrian H. Geyer for the single-crystal Raman analysis. Finally, we acknowledge the considerable financial support by the State of Baden-Württemberg (Stuttgart).

Conflicts of Interest: The authors declare no conflict of interest.

References

1. Blasse, G.; Grabmaier, B.C. *Luminescent Materials*; Springer: Berlin/Heidelberg, Germany, 1994.
2. Wontcheu, J.; Schleid, T. $Ce_2[SeO_3]_3$ and $Pr_2[SeO_3]_3$: *Non*-Isostructural Oxoselenates(IV) of the Light Lanthanoids. *Z. Anorg. Allg. Chem.* **2006**, *632*, 645–654. [CrossRef]
3. Wontcheu, J.; Schleid, T. $Sc_2Se_3O_9$: Scandium(III) Oxoselenate(IV) According to $Sc_2[SeO_3]_3$ with a Hexagonal "Lone-Pair" Channel Structure. *Z. Anorg. Allg. Chem.* **2003**, *629*, 1463–1465. [CrossRef]
4. Harrison, W.T.A. Lanthanum selenite, $La_2(SeO_3)_3$. *Acta Crystallogr.* **2000**, *56*, 627–628.
5. Wickleder, M.S. Wasserfreie Selenite des Lanthans: Synthese und Kristallstruktur von $La_2(SeO_3)_3$ und $LaFSeO_3$. *Z. Anorg. Allg. Chem.* **2000**, *626*, 547–551. [CrossRef]
6. Krügermann, I.; Wickleder, M.S. Syntheses and Crystal Structures of $Er_2(SeO_3)_3$ and $Dy_3(SeO_3)_4F$. *J. Solid State Chem.* **2002**, *167*, 113–118. [CrossRef]
7. Krügermann, I.; Wickleder, M.S.; Wontcheu, J.; Schleid, Th. The Unique Crystal Structure of the Triclinic Samarium(III) Oxoselenate(IV) $Sm_2[SeO_3]_3$. *Z. Anorg. Allg. Chem.* **2006**, *632*, 901–904. [CrossRef]
8. Krügermann, I.; Wickleder, M.S. Kristallstruktur und Phasenumwandlung von $Nd_2(SeO_3)_3$. *Z. Anorg. Allg. Chem.* **2002**, *628*, 2197. [CrossRef]
9. Krügermann, I. Oxoselenate(IV/VI) der Selten-Erd-Elemente und ihre Derivate. Ph.D. Thesis, Universität Köln, Cologne, Germany, 2002.
10. Wontcheu, J. Oxoselenates(IV) of the Trivalent Rare-Earth Elements and Some Derivatives. Ph.D. Thesis, Universität Stuttgart, Stuttgart, Germany, 2004.
11. Chou, S.-C. Rare-Earth Metal(III) Oxoselenates(IV) and Oxotellurates(IV) and Investigation of Their Luminescent Properties. Ph.D. Thesis, Universität Stuttgart, Stuttgart, Germany, 2015.
12. Wickleder, M.S. *Handbook on the Physics and Chemistry of Rare Earths*; Gschneidner, K.A., Jr., Bünzli, J.-C.G., Pecharsky, V.K., Eds.; Elsevier Scinece Publishers: New York, NY, USA, 2005; Volume 35.
13. Greiner, S. Untersuchungen zum Antennen-Effekt bei lanthanoidischen Leuchtstoffen auf Oxoselenat(IV)-Basis. Bachelor Thesis, Universität Stuttgart, Stuttgart, Germany, 2013.
14. Wontcheu, J.; Zitzer, S.; Schleid, Th. Die Lanthanoid(III)-Oxid-Oxoselenate(IV) $Ln_2O[SeO_3]_2$ (*Ln* = Sm − Tm). *Z. Naturforsch.* **2016**, *71b*, 1279–1285. [CrossRef]
15. Zitzer, S.; Su, S.-H.; Greiner, S.; Schleid, Th. $Sm_2Se_2O_7$ and $Sm_3O_2Cl[SeO_3]_2$: A New Monoclinic Modification of Samarium(III) Oxide Oxoselenate(IV) and a Samarium(III) Oxide Chloride Oxoselenate(IV) Both Containing Oxygen-Centered Samarium Tetrahedra. *Z. Anorg. Allg. Chem.* **2018**, in press.
16. Wontcheu, J.; Schleid, Th. $Tb_2Se_2O_7$: Terbium(III) Oxide Oxoselenate(IV) according to $Tb_2O[SeO_3]_2$ with a "Lone-Pair" Channel Structure. *Z. Anorg. Allg. Chem.* **2002**, *628*, 1941–1945. [CrossRef]
17. Greiner, S. Scandium(III)-Oxoselenate(IV) als kompakte Wirtsgitter für Lanthanoid-Dotierungen. Master's Thesis, Universität Stuttgart, Stuttgart, Germany, 2015.
18. Greiner, S.; Chou, S.-C.; Schleid, Th. Two anionically derivatized scandium oxoselenates(IV): $ScF[SeO_3]$ and $Sc_2O_2[SeO_3]$. *J. Solid State Chem.* **2017**, *246*, 160–166. [CrossRef]
19. Zhang-Preße, M.; Oppermann, H. Thermochemical Investigation of RE_2O_3–SeO_2 Systems, III. Yttrium selenium oxides in the pseudo-binary system. *J. Therm. Anal. Calorim.* **2002**, *69*, 301–316. [CrossRef]
20. Zhang-Preße, M.; Oppermann, H. Thermochemische Untersuchungen zu den Systemen SE_2O_3–SeO_2, IV. Lösungskalorimetrie der $SE_2Se_xO_{3+2x}$-Phasen (SE = Nd, Sm, Y). *Z. Naturforsch* **2002**, *57b*, 661–667.
21. Oppermann, H.; Zhang-Preße, M.; Schmidt, P. Thermochemische Untersuchungen zu den Systemen SE_2O_3–SeO_2, V. Ytterbiumselenoxide auf dem Schnitt Yb_2O_3–SeO_2. *Z. Naturforsch.* **2002**, *57b*, 868–876.
22. Oppermann, H.; Zhang-Preße, M.; Weck, S.; Liebig, S. Thermochemische Untersuchungen zu den Systemen SE_2O_3/SeO_2, I. Neodymselenoxide auf dem Schnitt Nd_2O_3–SeO_2. *Z. Anorg. Allg. Chem.* **2002**, *628*, 81–90. [CrossRef]
23. Oppermann, H.; Zhang-Preße, M. Thermochemische Untersuchungen zu den Systemen SE_2O_3–SeO_2, II. Samariumselenoxide auf dem Schnitt Sm_2O_3–SeO_2. *Z. Naturforsch* **2001**, *56b*, 917–926.
24. Wickleder, M.S. $Sm_2Se_5O_{13}$: A Selenite–Diselenite according to $Sm_2(SeO_3)(Se_2O_5)_2$. *Z. Anorg. Allg. Chem.* **2006**, *632*, 2377–2379. [CrossRef]
25. Song, S.Y.; Ok, K.M. Modulation of Framework and Centricity: Cation Size Effect in New Quaternary Selenites, $ASc(SeO_3)_2$ (A = Na, K, Rb, and Cs). *Inorg. Chem.* **2015**, *54*, 5032–5038. [CrossRef] [PubMed]

26. Herrendorf, W.; Bärnighausen, H. *HABITUS: Programm zur Optimierung der Kristallgestalt für die Numerische Absorptionskorrektur als Version X-SHAPE*, version 1.06; Universität Karlsruhe 1993, Universität Gießen 1996; Fa. Stoe: Darmstadt, Germany, 1999.
27. Sheldrick, G.M. *SHELX-97: Program Suite for the Solution and Refinement of Crystal Structures*; Universität Göttingen: Göttingen, Germany, 1997.
28. Sheldrick, G.M. A short history of SHELX. *Acta Crystallogr.* **2008**, *64*, 112–122. [CrossRef] [PubMed]
29. McCullough, J.D. The Crystal Structure of Selenium Dioxide. *J. Am. Chem. Soc.* **1937**, *59*, 789–794. [CrossRef]
30. Siebert, H. *Anwendung der Schwinungsspektroskopie in der Anorganischen Chemie*; Springer: Berlin/Heidelberg, Germany; New York, NY, USA, 1966.
31. Zitzer, S. Selten-Erd-Metall(III)-Oxoselenate(IV) und -Oxotellurate(IV): Synthese, Kristallstrukturaufklärung und fluoreszenzspektroskopische Untersuchungen ausgewählter Leuchtstoffe. Ph.D. Thesis, Universität Stuttgart, Stuttgart, Germany, 2011.
32. Ok, K.M.; Halasyamani, P.S. New Selenites: Syntheses, Structures, and Characterization of Centrosymmetric $Al_2(Se_2O_5)_3$ and $Ga_2(Se_2O_5)_3$ and Non-centrosymmetric $In_2(Se_2O_5)_3$. *Chem. Mater.* **2002**, *14*, 2360–2364. [CrossRef]
33. Verma, V.P. A review of synthetic, thermoanalytical, IR, Raman and X-ray studies on metal selenites. *Thermochim. Acta* **1999**, *327*, 63–102. [CrossRef]
34. Shannon, R.D. Revised Effective Ionic Radii and Systematic Studies of Interatomic Distances in Halides and Chalcogenides. *Acta Crystallogr.* **1976**, *32*, 751–767. [CrossRef]
35. Chou, S.-C.; Greiner, S.; Magdysyuk, O.V.; Dinnebier, R.E.; Schleid, Th. Theoretical and Experimental Analysis of Structural Phase Transitions for $ScF[SeO_3]$ and $YF[SeO_3]$. *Z. Anorg. Allg. Chem.* **2014**, *640*, 3203–3211. [CrossRef]
36. Greiner, S.; Schleid, T.H. $ScCl[SeO_3]$: The Chloride Oxoselenate(IV) of the Smallest Rare-Earth Metal. *Z. Anorg. Allg. Chem.* **2016**, *642*, 1076.

crystals

MDPI

Article

Role of Bis(triphenylphosphine)iminium Cation $[PNP]^+$ on the Crystal Packing of $[PNP]^+[HSeO_3]^-$ Solvate Salt

Stefano Canossa [1] and Claudia Graiff [1,2,*]

[1] Department of Chemistry, Life Sciences and Environmental Sustainability, University of Parma, Parco Area delle Scienze 17/A, 43124 Parma, Italy; stefano.canossa@studenti.unipr.it
[2] C.I.R.C.C.—Consorzio Interuniversitario Reattività Chimica e Catalisi, Via Celsio Ulpiani 27, 70126 Bari, Italy
* Correspondence: claudia.graiff@unipr.it; Tel.: +39-0521-905428

Received: 14 March 2018; Accepted: 28 March 2018; Published: 29 March 2018

Abstract: Selenate(IV) and hydrogen selenate(IV) salts of bulky cations are very interesting compounds for synthetic and kinetic studies. In this work, bis(triphenylphosphine)iminium ($[PNP]^+$) chloride has been used, which aims to synthesize the corresponding selenate(IV) salt by an exchange reaction in the aqueous solution and subsequent crystallization by solvent evaporation. Unexpectedly, the procedure afforded a solvate form of the $[PNP]^+[HSeO_3]^-$ salt (**1**). In this solid phase, which has a structure that is determined by Single Crystal XRD, the anion tends to maximize the interactions with itself, although it leaves the cationic moiety to have only weak interactions with the anions and the solvent molecules. In turn, the latter builds a network of effective hydrogen bonds. This behavior opposes the general tendency of selenite(IV) and hydrogen selenite(IV) compounds, since these anions are commonly found to have formed effective hydrogen bonds with surrounding chemical species. Moreover, as the exchange reaction is non-quantitative, the exceeding traces of the starting bis(triphenylphosphine)iminium chloride reagent reacted with bis(acetonitrile)dichloropalladium(II) to form the bis(triphenylphosphine)iminium hexachloropalladate (**2**). In the solid phase, $[PNP]^+$ causes the absence of strong supramolecular interactions, which highlights the peculiar behavior of the cation in the crystal packing of its solid phases.

Keywords: hydrogen selenate(IV) compounds; crystal structure; PNP salt; hydrogen bond interactions

1. Introduction

The interest of the scientific community in the structural chemistry of selenite(IV) and tellurate(IV) has grown significantly in the last decades due to several reasons. First of all, these anions allow the formation of solid state structures characterized by the presence of cavities, which are mostly in the form of channels. These cavities are able to house the selenium or tellurium electron pairs and form open framework structures [1–6]. Moreover, it is known that the presence of pyramidal anions, such as XO_3^{2-} (X = S, Se, Te), can lead to the formation of non-centrosymmetric structures. These materials can display non-linear optical properties and other interesting properties. such as ferroelectricity and piezoelectricity [7–12]. In addition, the weak coordinative capability of Se(IV) electron lone pairs in selenate(IV) anions has been recently suggested to play a crucial role in the formation of supramolecular interactions, which was observed in the case of the $[Pd_{15}(\mu_3\text{-}SeO_3)_{10}(\mu_3\text{-}O)_{10}Na]^{9-}$ anion [13]. On the other hand, the bis(triphenylphosphine)iminium cation has been used extensively as the counter ion in synthetic and kinetic studies. In fact, its salts are commonly very soluble and dissociate well in a number of aprotic solvents [14,15], thus allowing more homogeneous reactions and facilitating the study of their kinetics [16]. Moreover, the weak polarizability of this cation improves the crystallization and the consequent isolation of many salts of anions, which would otherwise not be

possible to obtain. Pursuing our interest in the chemistry of selenite(IV) metal complexes, we decided to investigate the reactivity of selenate(IV) of a bulky cation, such as bis(triphenylphosphine)iminium, in order to explore the possibility of using starting materials that are soluble in non-polar solvents. In fact, the absence of interactions between selenate(IV) anion and solvent molecules would promote the formation of coordinative interactions between the selenate(IV) anion and a metal ion. Moreover, the combination of a bulky cation, such as bis(triphenylphosphine)iminium, with the selenate(IV) anion might enhance the solubility of the selenate(IV) in a non-polar solvent. When in the presence of a cation, this combination is capable of creating interactions with anions of similar hindrance and dimensions, such as oxo- chloro- or cyanometallate, to promote the formation of crystalline phases [17]. With this idea in mind, we tried to synthesize the bis(triphenylphosphine)iminium selenate(IV) and aimed to react it with bis(acetonitrile)dichloropalladium(II).

2. Results and Discussion

Following the procedure reported in a previous study [18], we reacted aqueous solutions of bis(triphenylphosphine)iminium chloride and sodium selenate(IV) in a 1:5 molar ratio at 70 °C. The reaction was stirred for 10 min, before being cooled in an ice bath for 1 h. The pale gray microcrystalline powder subsequently obtained was filtered and washed with water. The powder is soluble at room temperature in acetone, methanol, ethanol, dimethylsulfide, acetonitrile, dichloromethane and chloroform. The IR spectrum of the microcrystalline product shows the typical bands of the bis(triphenylphosphine)iminium ion and two bands at 690 and 728 cm^{-1} due to the presence of Se-O groups (Figure S1). The SEM analysis conducted on the powder clearly shows the presence of chlorine, which likely belongs to the unreacted starting reagent (Figure S2). The slow solvent evaporation of a dichloromethane solution created prismatic colorless crystals suitable for single crystal X-Ray diffraction, which allowed the structure of this phase to be solved.

2.1. Crystal and Molecular Structure of Bis(triphenylphosphine)iminium Hydrogen Selenate(IV) Solvate (**1**)

The crystal structure of **1** consists of a bis(triphenylphosphine)iminium cation, a hydrogen selenate(IV) anion, a dichloromethane and a water molecule. The crystal structures of hydrogen selenate(IV) of alkali metals or ammonium have been largely reported in the literature [19–21], while relatively few phases containing hydrogen selenate(IV) and organic nitrogen cations have been described until now [22–29]. Some relevant features of the structure of **1** are reported in Figure 1.

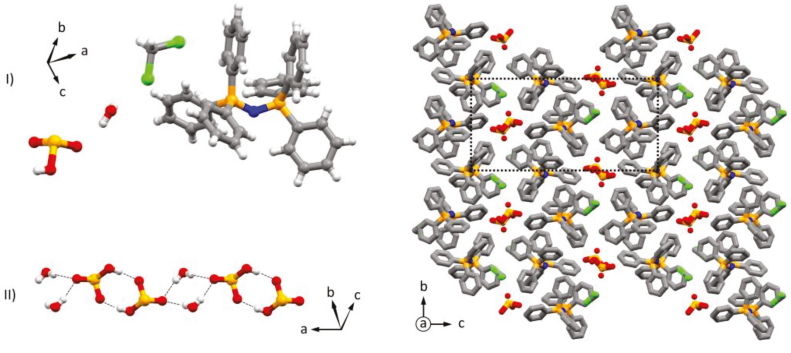

Figure 1. (I) Asymmetric unit of **1**, ball and stick representation; and (II) The chain formed by hydrogen selenite(IV) anions and water molecules is displayed in ball and stick representation. On the right, the crystal packing is shown along the crystallographic direction *a*; and the hydrogen atoms are omitted for the sake of clarity. This is shown in a capped sticks representation.

The hydrogen selenate(IV) anions are linked together by strong hydrogen bonds forming dimers (O···O distance 2.762(2) Å, O···H distance 1.964(2) Å, O-H···O angle 164.07(2)°). Two water molecules act as H-bond donors towards two different hydrogen selenate(IV) dimers, bridging them and forming an infinite chain of hydrogen selenate(IV) anions and water molecules. These develop along the crystallographic *a* axis. To the best of our knowledge, this type of arrangement has never been reported in the literature for hydrogen selenate(IV) anions. Remarkably, the selenium lone pair is not involved in any recognizable interaction, since the nearest H-bond donor, which is the adjacent aromatic –CH groups of PNP, are involved in H-bond with the oxygen atoms of the anions. A dichloromethane molecule is also present in the crystal packing, which is involved in interactions with another dichloromethane and with a water molecule through the H atoms. [Distance H···Cl 2.858(2) Å and distance H···O 2.142(2) Å]. As shown in Figure 2, the overall supramolecular network forms a grid, whose apertures host the bulky cations.

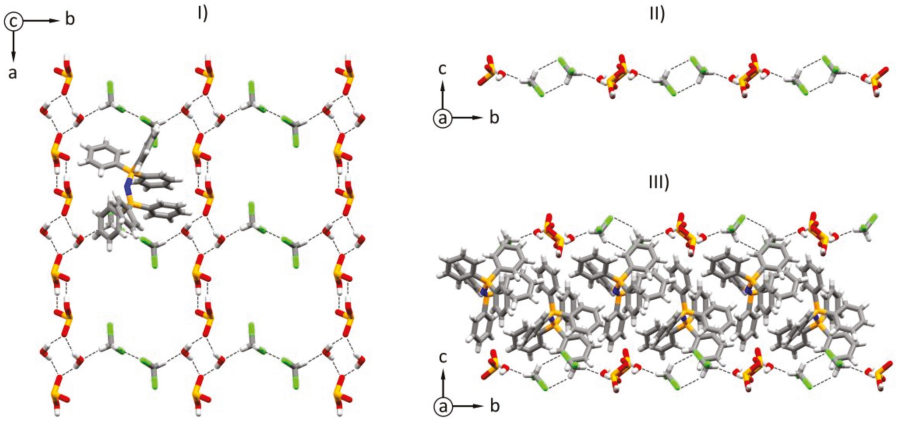

Figure 2. Supramolecular interactions in **1**. Hydrogen selenate(IV), dichloromethane and water molecules form a network of hydrogen bonds along the *a* and *b* directions (I, II). This arrangement forms square shaped apertures, where the $[PNP]^+$ cations are allocated (I; only one cation is shown for the sake of clarity), resulting in layers of cations (III). This is shown in a capped sticks representation.

Considering the structures reported in the Cambridge Crystallographic Data Centre that are comprised of hydrogen selenate(IV) anions of nitrogen containing cations, usually a strong network of hydrogen bonds developing in the entire three-dimensional array of the crystal packing is observed [22–29]. For example, the reported crystal structure of the ammonium hydrogen selenate(IV) [19], which is the simplest of this type of compounds, is consolidated by a network of hydrogen bonds, with donor···acceptor distances (N···$O_{(Se)}$ and O···$O_{(Se)}$) ranging between 2.80 and 3.07 Å. In other more complexes, nitrogen-containing organic cations have been reported, such as *N*,*N*′-dimethylpiperazinium [22], anilinium [23], L-triptophanium [29], 1-carbamoylguanidinium [24], L-argininium [25], *N*-*N*′-diphenylguanidinium [26], cytosinium [27], and several organoammonium cations described by Lukevics et al. [28]. The stabilization of the crystal packing is achieved again by forming an extended network of hydrogen bonds of the type O-H···$O_{(Se)}$, or N-H···$O_{(Se)}$. Various intermolecular hydrogen-bonding motifs, including linear and bifurcated bonds, are present and based on the O···$O_{(Se)}$ and N···$O_{(Se)}$ separations, these bonds vary in strength from fairly strong to very weak. Moreover, the directionality of the hydrogen bonds can contribute to the formation of layers or ribbons. In the crystal structure of 1-carbamoylguanidinium hydrogen selenate(IV) reported in a previous study [24], strong and short inter-selenate(IV) hydrogen bonds help to fuse molecular layers formed by the planar 1-carbamoylguanidinium ions into double sheets. In the case of the crystal structure of

anilinium hydrogen selenate(IV) monohydrate reported in a previous study [23], the crystal packing consists of alternating layers of anilinium cations and hydrogen selenate(IV) anions interconnected by N-H···O hydrogen bonds. Water molecules are located within the anionic layers and are involved in very strong O-H···O intermolecular interactions connecting the hydrogen selenate(IV) anions. On the contrary, in our case, the bulky bis(triphenylphosphine)iminium cation prevents the formation of strong intermolecular interactions between the cation and the hydrogen selenate(IV) anion. We found that the anion prefers to auto-assemble in the form of an infinite chain together with water molecules.

2.2. Reaction of the Crude Product of Bis(triphenylphosphine)iminium Chloride and Sodium Selenate(IV) with Bis(acetonitrile)dichloropalladium(II). Identification of Bis(triphenylphosphine)iminium Hexachloropalladate (**2**)

We know from a previous study [18] that by reacting the aqueous solutions of bis(triphenylphosphine)iminium chloride with an excess of sodium selenate(IV), the corresponding bis(triphenylphosphine)iminium selenate(IV) was formed. Therefore, we used the obtained white homogeneous microcrystalline powder in a reaction with bis(acetonitrile)dichloropalladium(II) dissolved in dichloromethane, with the aim to investigate the possibility of forming new crystalline phases containing selenate(IV) anions and bis(acetonitrile)palladium(II) cations. After stirring the reaction mixture for one hour at room temperature, the solvent was left to evaporate and red single crystals have grown. One of them was analyzed by X-Ray diffraction and the crystal structure revealed that bis(triphenylphosphine)iminium hexachloropalladate (**2**) was formed.

The compound is isostructural with the analogous bis(triphenylphosphine)iminium hexachlorocuprate [30]. The geometrical parameters of the bis(triphenylphosphine)iminium cation is consistent with those observed in the literature. Considering the crystal packing of the compound, the multiple pairs of approximately parallel phenyl rings are present and the bis(triphenylphosphine)iminium cations weakly interact through multiple C-H···Cπ interactions, which has C···C distances of 3.538(2)–3.757(2) Å. Moreover, six bis(triphenylphosphine)iminium cations surround a $[Pd_2Cl_6]^{2-}$ anion through C-H···Cl weak interactions [H···Cl distances of 2.736(2)–3.039(2) Å], which is shown in Figure 3. Once again, the bulky cation prevents the formation of strong interactions between itself and the anionic complex.

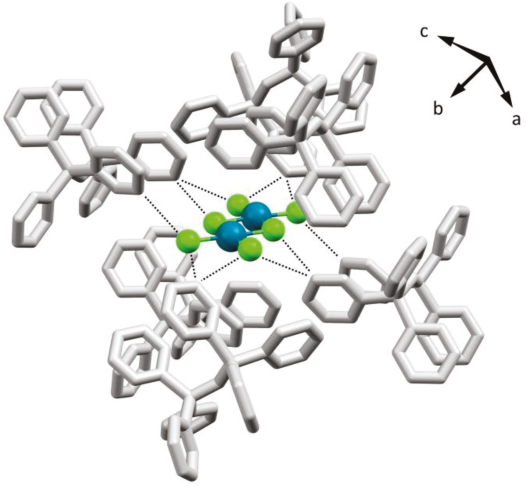

Figure 3. Crystal packing of **2** showing the six cationic molecules (capped sticks representation depicted in gray for clarity) that surrounds the hexachloropalladate anion.

In the crystal packing of the compound viewed along the crystallographic *a* axis (Figure 4), it is evident that the cations and hexachloropalladate anions tend to pile one over the other, forming infinite pillars of cations and anions.

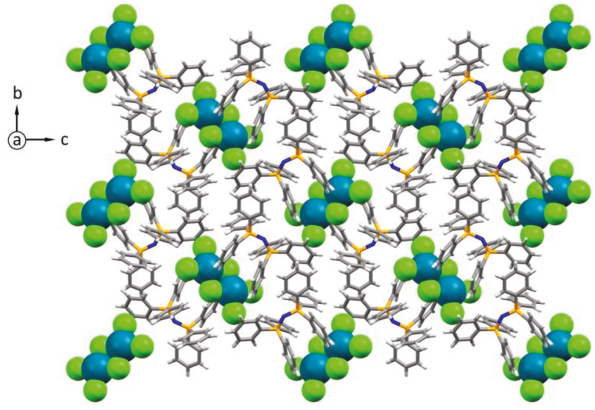

Figure 4. Crystal packing of **2** along the crystallographic axis *a*, highlighting the isolation of the chloro-anions (in ball and stick representation) by means of bis(triphenylphosphine)iminium cations (in capped sticks representation).

2.3. Crystal and Molecular Structure of a Novel Phase of Bis(triphenylphosphine)iminium Chloride Bihydrate (**3**)

In order to better investigate the nature of the microcrystalline powder obtained by reacting bis(triphenylphosphine)iminium chloride with an excess of sodium selenate(IV), a dichloromethane solution of the crude product was left to evaporate, creating two crystal phases with slightly different morphologies. The first type was the bis(triphenylphosphine)iminium hydrogen selenate(IV) solvate described above, while the second one was unambiguously identified as an unreported hydrated phase of bis(triphenylphosphine)iminium chloride (**3**). Several bis(triphenylphosphine)iminium chloride structures containing solvate molecules have been determined [31] and in our case, the principal geometrical parameters of the cations are in the expected range for similar bond distances and angles reported in the literature. On the other hand, we want to comment on the crystal packing of the bihydrated bis(triphenylphosphine)iminium chloride, highlighting once again the fact that the bulky bis(triphenylphosphine)iminium cations prevent the formation of strong intermolecular interactions between the cationic and the anionic parts of the compound. In fact, as shown in Figure 5, two water molecules and a chlorine atom are connected by hydrogen bonds and four bis(triphenylphosphine)iminium cations surround this aggregate, which interact by means of hydrogen bonds.

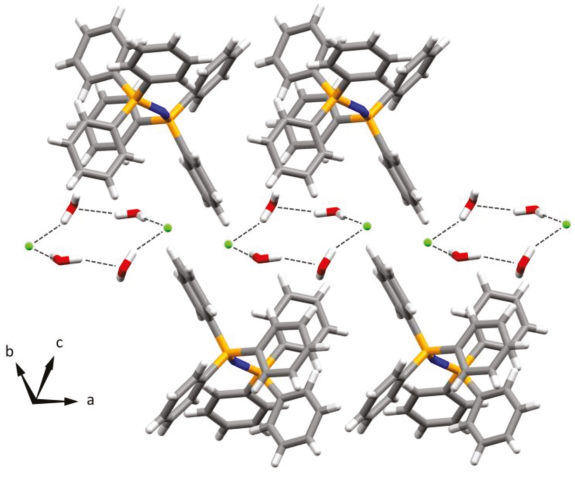

Figure 5. Crystal packing of **3**, showing the formation of hydrogen bonds between water molecules and chlorine atoms. This is shown in a capped sticks representation.

3. Conclusions

The synthesis of the bis(triphenylphosphine)iminium selenate(IV) is not easily predicted in a previous study [18], leading to the formation of the corresponding hydrogen selenate(IV) salt (**1**), which is shown by X-ray diffraction analysis. Moreover, the reaction does not fully complete, leaving traces of bis(triphenylphosphine)iminium chloride in the reaction mixture, although the exchange reaction has been carried out in the presence of an excess of sodium selenate(IV). The presence of chloride anions in the reaction mixture together with the scarce coordination ability of the acetonitrile ligands and the high stability of hexachloropalladate anion caused the formation of compound **2**, whose identity has been unequivocally confirmed by X-ray diffraction analysis. Further efforts aiming to purify the reaction mixture are needed to obtain a 100% yield of **1**. We observed that dissimilar to other ionic selenate(IV) and hydrogen selenate(IV) compounds reported in the CCDC (Cambridge Crystallographic Data Center), the anion does not interact with the bulky cation in the crystal packing of **1**, preferring to build 2D networks of hydrogen selenate(IV) and solvent molecules. A comparison between the crystal packing of the compound and the structural motifs reported in literature involving hydrogen selenate(IV) of organic nitrogen containing cations confirms that the presence of the bulky bis(triphenylphosphine)iminium cation prevents the formation of hydrogen bond interactions with the anionic part of the compounds. This behavior has also been shown in the case of the crystal structure of **2**, in which the cations and hexachloropalladate anions tend to pile one over the other, forming infinite pillars of cations and anions without any appreciable strong interactions between them.

4. Materials and Methods

4.1. General Remarks

All the preparations were carried out at room temperature in the presence of air. Bis(triphenylphosphine)iminium chloride, sodium selenate(IV), bis(acetonitrile)dichloropalladium(II) and solvents of acetone, methanol, ethanol, dimethylsulfide, acetonitrile, dichloromethane and chloroform were purchased and used as received (Merck KGaA, Darmstadt, Germany). FTIR spectra (4000–400 cm^{-1}) were recorded on a Nicolet Nexus spectrophotometer equipped with a Smart Orbit HATR accessory (diamond). SEM analysis was taken by a Scanning Electron Microscope (SEM) Jeol

6400 with Energy Dispersive System (EDS) Oxford INCA (15–20 kV, 1.2 nA, electronic beam diameter of 1 mm, acquisition time of 60 s).

4.1.1. Preparation of **1**

A water solution (10 mL) of Na_2SeO_3 (0.7635 g, 4.35 mmol) was added to a water solution (15 mL) containing PNPCl (0.5002 g, 0.87 mol) at 70 °C. The colorless solution was stirred at the same temperature for 10 min. After this, the solution was cooled at 0 °C using an ice bath for one hour. The white precipitate formed was filtered on a Buchner and washed with water. The microcrystalline solid is soluble in acetone, methanol, ethanol, dimethylsulfide, acetonitrile, dichloromethane and chloroform. This crystallizes by slow evaporation when dissolved again in dichloromethane, forming a small amount of colorless crystals suitable for X-ray analysis together with very few morphologically different ones, which were subsequently identified as hydrated PNPCl salts (see Section 2). The FTIR of the identified bis(triphenylphosphine)iminium hydrogen selenate(IV) (Diamond crystal HATR, cm^{-1}) was at υ of 498 cm^{-1}, 531 cm^{-1}, 690 cm^{-1}, 728 cm^{-1}, 1002 cm^{-1}, 1117 cm^{-1}, 1227 cm^{-1}, 1265 cm^{-1}, 1441 cm^{-1} and 3057 cm^{-1}.

4.1.2. Preparation of **2**

A dichloromethane solution (5 mL) containing 0.078 g of bis(acetonitrile)dichloropalladium(II) was added dropwise to 10 mL of a dichloromethane solution, which contained 0.204 g of the white microcrystalline powder that was prepared according to Section 4.1.1. The solution is stirred at room temperature for 1 h and the color changed to deep red. Under slow evaporation of the solvent, several red crystals are formed and analyzed by X-ray diffraction methods.

4.2. X-ray Data Collection, Structure Solution, and Refinement

The intensity data of the three compounds were collected at room temperature on a Bruker APEX II single crystal diffractometer [32,33] equipped with an area detector using a graphite monochromated Mo Kα radiation (λ = 0.71073 Å). Crystallographic and experimental details of the reported structures are summarized in Table 1. The structures were solved by direct methods and refined by full-matrix least-squares procedures (based on Fo^2) using SHELXL-2014/7 [34]. This is first conducted with isotropic thermal parameters, before using anisotropic thermal parameters in the last cycles of refinement for all the non-hydrogen atoms. The hydrogen atoms were introduced into the geometrically calculated positions and refined depending on the corresponding parent atoms, except for the hydrogen atoms of the water molecules in **1** and in **3**. CCDC 1829597, 1829598 and 1829599 contain the supplementary crystallographic data for this paper. These data can be obtained free of charge via http://www.ccdc.cam.ac.uk/conts/retrieving.html (or from the CCDC, 12 Union Road, Cambridge CB2 1EZ, UK; Fax: +44-1223-336-033; E-mail: deposit@ccdc.cam.ac.uk).

Table 1. Summary of crystallographic data for **1**, **2** and **3**.

	[PNP][HSeO$_3$]·H$_2$O·CH$_2$Cl$_2$ 1	**[PNP]$_2$[Pd$_2$Cl$_6$] 2**	**[PNP]Cl·2H$_2$O 3**
Formula	C37 H35 Cl2 N O4 P2 Se	$C_{72}H_{60}N_2P_4Pd_2Cl_6$	$C_{36}H_{34}ClNO_2P_2$
FW	769.46	1502.6	610.03
crystal system	monoclinic	monoclinic	monoclinic
space group	$P2_1/c$	$P2_1/c$	$P2_1/c$
a, Å	10.8664(11)	9.1894(4)	10.6243(9)
b, Å	12.6743(13)	22.3661(10)	12.6404(11)
c, Å	26.029(3)	16.2595(7)	23.595(2)
β, deg	95.727(2)	103.657(1)	101.558(2)
V, Å^3	3567.0(6)	3247.4(2)	3104.4(5)
Z	4	2	4
D_{calcd}, g cm^{-3}	1.433	1.537	1.305
F(000)	1576.0	1520.0	1280.0
μ, cm^{-1}	1.333	0.944	0.260
rflns collected	34915	50951	49398
rflns unique	5605	9552	9461
rflns observed [I>2σ(I)]	4326 [R_{int} = 0.0335]	7832 [R_{int} = 0.0334]	6719 [R_{int} = 0.0435]
Parameters	428	388	385
R indices [I>2σ(I)]	R1 = 0.0963; wR2 = 0.3612	R1 = 0.0319; wR2 = 0.0817	R1 = 0.0652; wR2 = 0.1825
R indices (all data)	R1 = 0.1141; wR2 = 0.3953	R1 = 0.0425; wR2 = 0.0867	R1 = 0.0918; wR2 = 0.2039

$R1 = \sum | |F_o| - |F_c| | / \sum |F_o|$. $wR2 = [\sum[w(F_o^2 - F_c^2)^2] / \sum[w(F_o^2)^2]]$.

Supplementary Materials: The following are available online at http://www.mdpi.com/2073-4352/8/4/151/s1, Figure S1: IR pattern of bis(triphenylphosphine)iminium hydrogen selenite, Figure S2: SEM analysis on the microcrystalline powder obtained by reaction between bis(triphenylphosphine)iminium chloride and sodium selenite in 1:5 molar ratio.

Author Contributions: Both authors contributed equally to the research and writing of the present paper.

Conflicts of Interest: The authors declare no conflict of interest.

References

1. Paterson, B.; Harrison, W.T.A. Synthesis and Crystal Structure of In(OH)(SeO_3). *Zeitschrift fur Anorganische und Allgemeine Chemie* **2007**, *633*, 158–161. [CrossRef]
2. Wontcheu, J.; Schleid, T. $Tb_3O_2Cl[SeO_3]_2$ and $Tb_5O_4Cl_3[SeO_3]_2$: Oxide chloride oxoselenates(IV) of trivalent terbium with "lone-pair" channel or layer structures. *Zeitschrift fur Anorganische und Allgemeine Chemie* **2005**, *631*, 309–315. [CrossRef]
3. Albrecht-Schmitt, T.E.; Almond, P.M.; Sykora, R.E. Cation-cation interactions in neptunyl(V) compounds: Hydrothermal preparation and structural characterization of $NpO_2(IO_3)$ and α- and β-$AgNpO_2(SeO_3)$. *Inorg. Chem.* **2003**, *42*, 3788–3795. [CrossRef] [PubMed]
4. Porter, Y.; Halasyamani, P.S. New alkali-metal-molybdenum(VI)-selenium(IV) oxides: Syntheses, structures, and characterization of A_2SeMoO_6(*A*=Na+, K+, or Rb+). *J. Solid State Chem.* **2003**, *174*, 441–449. [CrossRef]
5. Almond, P.M.; Peper, S.M.; Bakker, E.; Albrecht-Schmitt, T.E. Variable dimensionality and new uranium oxide topologies in the alkaline-earth metal uranyl selenites *AE*[$(UO_2)(SeO_3)_2$] (*AE*=Ca, Ba) and Sr[$(UO_2)(SeO_3)_2$] $2H_2O$. *J. Solid State Chem.* **2002**, *168*, 358–366. [CrossRef]
6. Harrison, W.T.A. Caesium vanadium selenite, $Cs(VO_2)_3(SeO_3)_2$. *Acta Crystallogr. Sect. C Cryst. Struct. Commun.* **2000**, *C56*, e422. [CrossRef]
7. Halasyamani, P.S.; Poeppelmeier, K.R. Noncentrosymmetric Oxides. *Chem. Mater.* **1998**, *10*, 2753–2769. [CrossRef]
8. Ra, H.-S.; Ok, K.M.; Halasyamani, P.S. Combining second-order Jahn-Teller distorted cations to create highly efficient SHG materials: Synthesis, characterization, and NLO properties of $BaTeM_2O_9$ (M = Mo^{6+} or W^{6+}). *J. Am. Chem. Soc.* **2003**, *125*, 7764–7765. [CrossRef] [PubMed]
9. Ok, K.M.; Halasyamani, P.S. Asymmetric Cationic Coordination Environments in New Oxide Materials: Synthesis and Characterization of $Pb_4Te_6M_{10}O_{41}$(M = Nb^{5+} or Ta^{5+}). *Inorg. Chem.* **2004**, *43*, 4248–4253. [CrossRef] [PubMed]

10. Ok, K.M.; Orzechowski, J.; Halasyamani, P.S. Synthesis, Structure, and Characterization of Two New Layered Mixed-Metal Phosphates, $BaTeMO_4(PO_4)$ (M = Nb^{5+} or Ta^{5+}). *Inorg. Chem.* **2004**, *43*, 964–968. [CrossRef] [PubMed]
11. Goodey, J.; Ok, K.M.; Broussard, J.; Hofmann, C.; Escobedo, F.V.; Halasyamani, P.S. Syntheses, structures, and second-harmonic generating properties in new quaternary tellurites: $A_2TeW_3O_{12}$(*A*=K, Rb, or Cs). *J. Solid State Chem.* **2003**, *175*, 3–12. [CrossRef]
12. Mao, J.-G.; Jiang, H.-L.; Kong, F. Structures and Properties of Functional Metal Selenites and Tellurites. *Inorg. Chem.* **2008**, *47*, 8498–8510. [CrossRef] [PubMed]
13. Delferro, M.; Graiff, C.; Elviri, L.; Predieri, G. Self-assembly of polyoxoselenitopalladate nanostars $[Pd_15(\mu_3\text{-}SeO_3)_10(\mu_3\text{-}O)_10Na]^{9-}$ and their supramolecular pairing in the solid state. *Dalton Trans.* **2010**, *39*, 4479–4481. [CrossRef] [PubMed]
14. Savedoff, L.G. Conductance of Electrolytes in Anhydrous Acetone. *J. Am. Chem. Soc.* **1966**, *88*, 664–667. [CrossRef]
15. Springer, C.H.; Coetzee, J.F.; Kay, R.L. Transference number measurements in acetonitrile as solvent. *J. Phys. Chem.* **1969**, *73*, 471–476. [CrossRef]
16. Austad, T.; Engemyr, L.B.; Songstad, J. The Nucleophilicity of the Cyanate Ion. *Acta Chem. Scand.* **1971**, *25*, 3535–3536. [CrossRef]
17. De Lorentiis, L.; Graiff, C.; Predieri, G. Bis(triphenylphosphanylidene)iminium dichloridotriphenylstannate(IV). *Acta Crystallogr. Sect. E Struct. Rep. Online* **2011**, *E67*, m1356. [CrossRef] [PubMed]
18. Martinsen, A.; Songstad, J.; Larsson, R.; Pouchard, M.; Hagenmuller, P.; Andresen, A.F. Preparation and Properties of Some Bis(triphenylphosphine)iminium Salts, $[(Ph_3P)_2N]X$. *Acta Chem. Scand.* **1977**, *A31*, 645–650. [CrossRef]
19. Weil, M. Ammonium hydrogenselenate(IV). *Acta Crystallogr. Sect. E Struct. Rep. Online* **2006**, *E62*, i38–i40. [CrossRef]
20. Chomnilpan, B.Y.S.; Liminga, R. Lithium Hydrogenselenite. *Acta Crystallogr.* **1979**, *B35*, 3011–3013. [CrossRef]
21. Chomnilpan, S.; Liminga, R.; Sonnenveld, E.J.; Visser, J.W. A Reinvestigation of the Structure of Sodium Hydrogenselenite. *Acta Cryst.* **1981**, *B37*, 2220–2223. [CrossRef]
22. Němec, I.; Chudoba, V.; Havlíček, D.; Císařová, I.; Mička, Z. Preparation, crystal structure, vibrational spectra, and thermal behavior of N, N′-dimethylpiperazinium(2+) hydrogen selenite. *J. Solid State Chem.* **2001**, *161*, 312–318. [CrossRef]
23. Takouachet, R.; Benali-Cherif, R.; Bendeif, E.E.; Benali-Cherif, N.; Pillet, S.; Schaniel, D. Structural analysis and IR-spectroscopy of a new anilinium hydrogenselenite hybrid compound: A subtle structural phase transition. *Inorg. Chim. Acta* **2016**, *446*, 6–12. [CrossRef]
24. Ritchie, L.K.; Harrison, W.T.A. 1-Carbamoylguanidinium hydrogenselenite. *Acta Crystallogr. Sect. E Struct. Rep. Online* **2003**, *59*, o1296–o1298. [CrossRef]
25. De Matos Gomes, E.; Nogueira, E.; Fernandes, I.; Belsley, M.; Paixao, J.A.; Matos Beja, A.; Ramos Silva, M.; Martín-Gil, J.; Mano, J.F. Synthesis, structure, thermal and non-linear optical properties of L-argininium hydrogen selenite. *Acta Crystallogr. Sect. B Struct. Sci.* **2001**, *B57*, 828–832. [CrossRef] [PubMed]
26. Paixão, J.A.; Matos Beja, A.; Ramos Silva, M.; de Matos Gomes, E.; Martín-Gil, J.; Martín-Gil, F.J. N,N′-Diphenylguanidinium Hydrogenselenite Monohydrate. *Acta Crystallogr. Sect. C Crystal Struct. Commun.* **1997**, *53*, 1113–1115. [CrossRef]
27. Takouachet, R.; Benali-Cherif, R.; Benali-Cherif, N. Cytosinium hydrogen selenite. *Acta Crystallogr. Sect. E Struct. Rep. Online* **2014**, *70*, 57–64. [CrossRef] [PubMed]
28. Lukevics, E.; Arsenyan, P.; Shestakova, I.; Domracheva, I.; Kanepe, I.; Belyakov, S.; Popelis, J.; Pudova, O. Synthesis, structure and cytotoxicity of organoammonium selenites. *Appl. Organomet. Chem.* **2002**, *16*, 228–234. [CrossRef]
29. Paixão, J.A.; Silva, M.R.; Beja, A.M.; Eusébio, E. Crystal structure and properties of l-tryptophanium hydrogen selenite. *Polyhedron* **2006**, *25*, 2021–2025. [CrossRef]
30. Hasselgren, C.; Jagner, S.; Dance, I. Three-Coordinate $[Cu^{II}X_3]^-$ (X=Cl, Br), Trapped in a Molecular Crystal. *Chem. A Eur. J.* **2002**, *8*, 1270–1278. [CrossRef]
31. Andrews, S.J.; Robbt, D.A.; Welch, A.J. Structure of Bis(triphenylphosphoranediyl)ammonium Chloride-Boric Acid Adduct (1:1), C36H30NP2+.CI-.BH303. *Acta Crystallogr.* **1983**, *C39*, 880–882.
32. Bruker. *SAINT*; Version 7.06a; Bruker AXS Inc.: Madison, WI, USA, 2003.

33. Sheldrick, G.M. *SADABS—Bruker Nonius Area Detector Scaling and Absorption Correction, V2016/2*; Bruker AXS Inc.: Madison, WI, USA, 2016.
34. Sheldrick, G.M. Crystal structure refinement with SHELXL. *Acta Crystallogr. Sect. C Struct. Chem.* **2015**, *71*, 3–8. [CrossRef] [PubMed]

crystals

MDPI

Review

Selenium-Doped Hydroxyapatite Nanocrystals–Synthesis, Physicochemical Properties and Biological Significance

Kamil Pajor, Lukasz Pajchel, Barbara Kolodziejska and Joanna Kolmas *

Chair and Department of Inorganic and Analytical Chemistry, Faculty of Pharmacy with Laboratory Medicine Division, Medical University of Warsaw, ul. Banacha 1, 02-097 Warsaw, Poland; kamil.pajor@wum.edu.pl (K.P.); lukasz.pajchel@wum.edu.pl (L.P.); bkolodziejska21@gmail.com (B.K.)

* Correspondence: joanna.kolmas@wum.edu.pl; Tel.: +48-22-5720755

Received: 30 March 2018; Accepted: 24 April 2018; Published: 26 April 2018

Abstract: Hydroxyapatites (HAs), as materials with a similar structure to bone minerals, play a key role in biomaterials engineering. They have been applied as bone substitute materials and as coatings for metallic implants, which facilitates their osseointegration. One of the beneficial characteristics of HA, when used to create biocompatible materials with improved physicochemical or biological properties, is its capacity for ionic substitution. The aim of the study was to present the current state of knowledge about HAs containing selenate ions IV or VI. The enrichment of HAs with selenium aims to create a material with advantageous effects on bone tissue metabolism, as well as having anticancer and antibacterial activity. The work is devoted to both methods of obtaining Se-HA and an evaluation of its chemical structure and physicochemical properties. In addition, the biological activity of such materials in vitro and in vivo is discussed.

Keywords: hydroxyapatite; ionic substitution; selenium; selenite; selenite; physicochemical properties; biomaterials; bioceramics

1. Introduction

Calcium hydroxyapatite (HA), with the general formula $Ca_{10}(PO_4)_6(OH)_2$, belongs to the group of crystalline calcium phosphates [1]. Until recently, it was considered to be the main inorganic component of bone tissue and mineralized dental tissues. However, it turned out that biological apatite is characterized by a more complex composition; nevertheless, synthetic HA has been used as a bone replacement in orthopaedics, implantology, regenerative medicine, and dental surgery [2].

Hydroxyapatite is characterized by its high biocompatibility with bone tissue and its complete non-toxicity. Importantly, it has osteoconductive properties, stimulating bone tissue to grow. Therefore, HA is one of the basic materials used to cover metallic periosteal implants [2,3]. It is also used to create bone substitute materials and implants; however, its fragility limits its application only to areas with low mechanical stresses. In turn, one of the beneficial features of HA-based materials is their porosity, which depends, inter alia, on the method of synthesis and preparation. This feature is used in the development of bone drug delivery systems [4].

This work focuses on synthetic HA modified with selenium ions IV and VI. Our aim was to present the current state of knowledge on selenium's effect on the structure of HA and on its biological properties.

1.1. Hydroxyapatite–Structure and Function

Pure, stoichiometric HA crystallizes in a monoclinic system, space group $P2_1/b$ [5]. However, it is worth mentioning that HA like this is rare and very difficult to obtain by synthesis.

The most common type of HA is the type that crystallizes in the hexagonal system, space group $P6/_3m$ [5]. The crystallographic structure is well known and has been described in many articles [6,7]. In short, hydroxyl ions are located in the corners of the rhomboidal cell base (Figure 1). Six calcium ions are associated with hydroxyl groups from the unit cell corners. These calcium atoms (denoted in the literature as Ca(2)) form equilateral triangles situated perpendicularly to the "*c*" axis, and moved away from each other by 60°. The remaining four calcium atoms are arranged in two separate columns along the "*c*" axis. They are surrounded by six oxygen atoms derived from phosphate ions. Phosphorus atoms surrounded by four oxygen atoms occupy most of the space between the calcium ions, creating almost regular tetrahedrons. The parameters of the crystal lattice are as follows: $a = b = 9.432$, $c = 6.881$ Å, $\gamma = 120°$ [5,6].

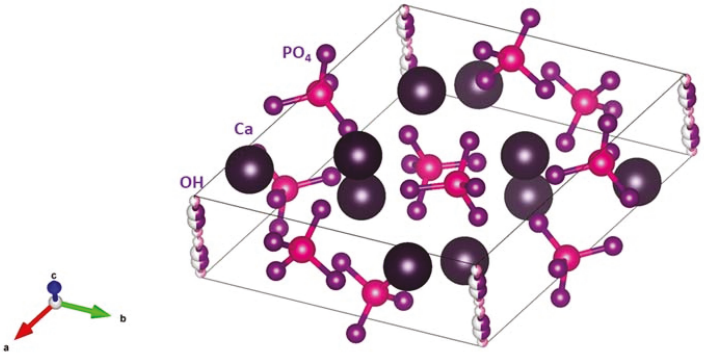

Figure 1. Crystallographic structure of HA.

The characteristic feature of HA is its susceptibility to ion substitutions, both in place of anions and cations, in the crystal lattice [7]. Certainly, ion exchange affects the size of the unit cell, the lattice parameters and, thus, the size of the crystallites. It also affects the physicochemical properties of HA, such as its solubility, thermal stability, surface area. Additionally, it is very important that "foreign ions" introduced into the HA structure can provide new biological properties. For example, silicate ions (SiO_4^{4-}) stimulate the proliferation of osteoblasts, thus improving the bioactivity of HA [8]. Silver ions have a strong bactericidal effect on most Gram(−) and Gram(+) strains, which can be used in the production of biomaterials with additional antibacterial properties [9].

1.2. The Role of Selenium in Human Organisms

Selenium is one of the essential microelements determining the proper functioning of the human body. The characteristic feature of selenium is its narrow therapeutic window—there is a very small difference between a concentration having a beneficial effect on the human body and one at which toxic activity is exhibited [10]. Selenium exhibits antioxidant properties and protects the body against free radicals and carcinogens. It contributes towards many biochemical processes as an important component of the 25 known selenoenzymes, e.g., glutathione peroxidase or iodothyronine deiodinase [11–13]. To date, there have been reports on the positive effects of selenium on cardiovascular diseases, cancers, the thyroid, the brain, reproduction, bone tissue, and viral infections, as well as on the immune system (Figure 2).

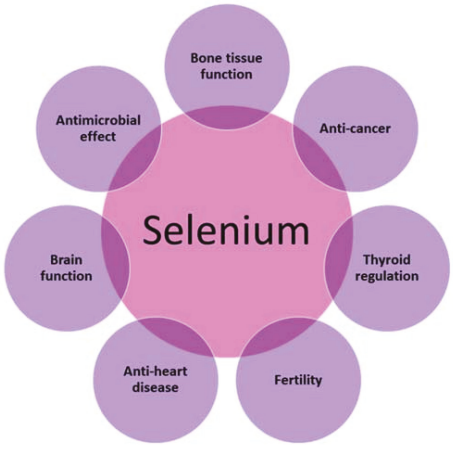

Figure 2. The health benefits of selenium.

Selenium also has immunostimulatory properties. It has been demonstrated that it increases the proliferation of activated T lymphocytes, increases the cytotoxicity of cancer cells, and also activates NK cells. The possible mechanism of the immunostimulatory action of selenium involves an increase in the expression of interleukin 2 receptors, which induces the proliferation of T lymphocytes [14,15]. It was proven in studies on mice that those on a diet rich in selenium showed an increased expression of interleukin 2, which was accompanied by a strengthened signal from T lymphocytes [16].

It was proven that selenium deficiency affects the development of epileptic seizures, and Parkinson's disease, as well as leading to coordination problems and a decline in cognitive skills [17,18]. Selenium also has a significant effect on male fertility [19,20]. It participates in the biosynthesis of testosterone, as well as in the formation and development of spermatozoa [19].

The thyroid is the organ containing the highest concentration of selenium. As mentioned, selenium is a component of selenoenzymes—for example, deiodinase, which is involved in the production of active thyroid hormones—and triiodothyronine from an inactive precursor, thyroxine. Moreover, selenium in the form of glutathione peroxidase protects the thyroid cells against hydrogen peroxide, which is formed as a result of the synthesis of thyroid hormones. An excess of this compound could cause the destruction and fibrosis of the gland [13,21,22].

Studies have indicated that low blood levels of selenium are also associated with myocardial infarction incidents and an increased risk of death due to cardiovascular diseases. Selenoproteins prevent the oxidative modification of lipids, inhibit platelet aggregation, and inhibit inflammation [21,23]. Therefore, selenium, through glutathione peroxidase, helps to protect the endothelial cells of blood vessels from the deposition of oxidized low-density lipoproteins arising from the oxidation of phospholipids and cholesterol esters. Therefore, it prevents atherosclerosis and its consequences [24–26].

The development of cancers is mediated by, inter alia, oxidative stress, as well as impaired bodily protective functions [13,27]. In recent years, scientists have been conducting intensive research on the effect of selenium on the reduction of colon, lung, liver, thyroid, and prostate cancer. Czeczot et al. [27] found a decrease in the activity of glutathione peroxidase in hepatic liver tissue when compared to healthy tissue. This weaker level of enzyme activity may result in enhanced lipid peroxidation and an increase in the number of final peroxidation products, such as malonic aldehyde (MDA). Increased MDA levels were observed in tumour tissue. The studies prove that there may be many mechanisms by which selenium inhibits carcinogenesis and improves the effectiveness of

cytostatic drugs, as well as reasons why the relationship between selenium dose and tumour growth is not linear [24,28].

Selenium is also essential for the proper functioning of bone tissue. It has been proven that selenium deficiencies may delay growth and affect the metabolism of bone tissue [29]. The mechanism of these processes is associated with the function of selenoproteins, of which at least nine are expressed in human foetal osteoblasts. Their expression seems to protect bones from oxidative stress, which is important in the regulation of inflammation and the differentiation of bone cells. An excessive level of intracellular reactive oxygen species (ROS) may contribute to the development of osteoporosis by inhibiting the differentiation of osteoblasts in bone marrow stromal cells [30,31]. It was found that the concentration of selenium in plasma is inversely proportional to the rate of bone tissue turnover and positively correlated with the incidence of low bone mineral density in healthy postmenopausal women [32]. Selenium may play an important role in cells, especially at doses higher than those required for the maximal expression of selenoproteins. It can induce cell-cycle inhibition, apoptosis, immune function or the prevention of bone resorption through the inactivation of osteoclasts. These processes can provide potential protection against rheumatoid arthritis, osteoarthritis, or osteoporosis [31].

2. Synthesis of Hydroxyapatites Doped with Selenite and Selenate Ions

HA doped with selenium ions can be obtained in two ways: through synthesis, during which ions are incorporated into the HA structure [33–47], or by ion exchange, where soaking in a selenium salt solution results in the exchange of ions in the HA structure [47].

Theoretically, there are two positions in the unit cell of the HA crystal in which it is possible to incorporate selenite (SeO_3^{2-}) or selenate (SeO_4^{2-}) ions: into the structural channels of OH groups along the *c*-axis or in the orthophosphate site [29]. SeO_4^{2-} ions have a structure geometrically similar to the PO_4^{3-} ion, although they are much larger and measure 249 pm in diameter compared to the diameter of 238 pm of the PO_4^{3-} ion [42,43,48]. SeO_3^{2-} ions have a similar diameter to that of PO_4^{3-} ions, measuring 239 pm; however, they differ in their geometric arrangement and have a flat trigonal pyramid structure [43,48,49] (see Figure 3). Looking at the size of SeO_3^{2-} and SeO_4^{2-} ions, their incorporation into the structure of HA is possible, but, as shown in the model diagram by Kolmas et al., only in place of phosphate ions [40]. Moreover, the authors noticed that, in the case of PO_4^{3-} ion substitution with SeO_3^{2-} or SeO_4^{2-} ions, we substitute a triple charge ion with a double charge ion which, in turn, leads to the simultaneous removal of Ca^{2+} and OH^- ions according to Equation (1) [43]:

$$Ca_{10}(PO_4)_6(OH)_2 + xSeO_n^{2-} \rightarrow Ca_{10-x}(PO_4)_{6-x}(SeO_n)_x(OH)_{2-x} + xPO_4^{3-} + xCa^{2+} + xOH^- \quad (1)$$

where *x* is the content of selenium oxyanions, and n may be 3 or 4 depending on whether a selenite or selenate ion has been substituted.

Studies on the adsorption of selenium ions to the surface of HA crystals have examined both the adsorption of selenite and selenate ions [50–52]. These studies have confirmed that these ions are incorporated in the place of phosphate groups, but it was surprising that SeO_3^{2-} or SeO_4^{2-} ions do not stay on the surface, but diffuse into the interior to a depth of a few nanometres [51]. Moreover, the sorption capacity of the selenite ions was significantly higher than that of selenate ions [52].

During Se-HA synthesis, selenium-doped HA was most frequently obtained (both in the form of SeO_3^{2-} and SeO_4^{2-}) using the wet method with a co-precipitation reaction.

The obtained powders contained various amounts of selenium [33–47], most often up to 10% by weight [33,36,37,40,41,43,44,46]. It should be noted that the reaction efficiency was often lower than 100% [33,36,40,41,43,44,46]. Ma et al. obtained a SeO_3-HA series starting from a small concentration of 3% of Se-substituted phosphate ions up to the almost full replacement of P ions with Se ions using a molar ratio of Se:P at 100:1 during the synthesis [45].

It is worth noting that the SeO_3-HA obtained in the studies [34,38,39] was used to prepare biocomposites containing silk fibres [34] or lysozyme [39]. It was possible to incorporate between 6 and 30% of selenium ions relative to phosphorus ions into such materials.

Zhang et al. [42] slightly modified the wet method. The precipitated crystals were treated hydrothermally for 36 h at 160 °C. By so doing, selenium ions were incorporated in a molar ratio of Se:P ranging from 0.001 to 0.421 [42]. The solvothermal method of heating for 10 h at 120 °C was also applied by Sun et al. [35]. The reaction was carried out in a Teflon-lined reactor with the addition of PEG 20000 and oleic acid in substrate proportions that allowed a series of samples to be obtained that contained between 0% and 55% of phosphate ions replaced with selenite ions [35].

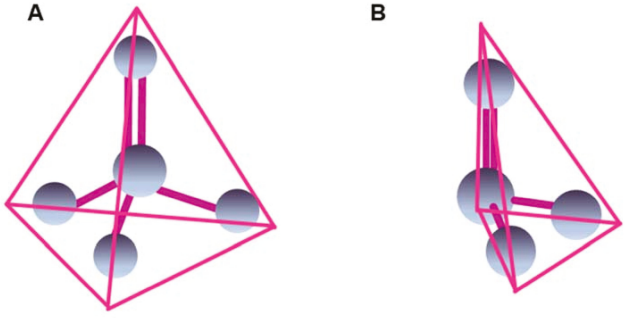

Figure 3. Tetrahedral (**A**) and trigonal pyramid (**B**) arrangements of phosphate and selenite (**A**) and selenite (**B**) ions.

In the studies [33,37,40], a dispersion agent was used in the wet method in the form of either sodium polyacrylate [37,40] or PEG [33]. In turn, the post-precipitation method, in which the surface phosphate groups are exchanged with selenium ions, was used by Uskokovic et al. [47]. They immersed previously precipitated HA crystals in a sodium selenite solution (pH ~10) while maintaining the solid phase content within the range of 10–40% w/w for a period of 48 h. In this way, a maximum of 0.36% by weight of selenium was incorporated into the hydroxyapatite structure [47].

In the case of surface HA coating, the PLD (pulsed laser deposition) application of powders, consisting of a mixture of HA and selenium powder, is used [53,54]. In such coatings made on titanium or silicon, the plan was to incorporate up to 2.7% of selenium [53,54]. The apatite material was applied using the PLD method under reduced pressure in a steam atmosphere, heating the carrier up to 460 °C using a laser with a wavelength of 193 nm [53,54].

HA coatings can also be obtained by soaking carried out in a simulated body fluid (SBF) doped with selenate ions [55].

3. Physicochemical Examination of Hydroxyapatites Doped with Selenate and Selenite Ions

In order to confirm the HA structure during the incorporation of selenium ions, the samples were analysed using powder diffractometry (PXRD). Based on the resulting diffractograms, the size of the obtained crystallites, the crystallinity, as well as the size of the unit cell of the obtained crystals, were also calculated. The morphology of the obtained crystals can be described using images taken via transmission and scanning electron microscopy (TEM and SEM). In order to confirm the incorporation of SeO_3^{2-} and SeO_4^{2-} ions into the HA structure, spectra were performed by using medium-infrared spectroscopy, Raman spectroscopy, and nuclear magnetic resonance imaging. Elemental analysis of the samples was performed using energy-dispersive X-ray spectroscopy (EDS), X-ray fluorescence spectroscopy (XRF) and X-ray photoelectron spectroscopy (XPS), as well as the titration method.

3.1. Powder Diffractometry (PXRD)

In each of the discussed studies, it was confirmed, based on a comparison of the obtained results with a reference sample containing no selenium ions and/or with a model HA diffractogram originating from ICDD and JCPDS databases, that monophasic material was obtained with a preserved $P6_3/_m$ crystallographic system characteristic of HA.

In the study [43], diffractograms obtained for samples doped with selenate and selenite ions were compared with a diffractogram of standard HA and it was shown that the former have weakly separated wide reflections and that some of them are too wide to be distinguishable. Based on the Scherrer equation, the crystal dimensions were estimated using the reflexes (002) and (130/310) along the *c* and *a* axis, respectively. It was found that, after the introduction of selenite and selenate ions, the size of the crystals was similar to the size of crystals of biological apatites in bone tissue [43]. However, a decrease in the size of crystallites in comparison to pure HA was observed in the study [36], with dimensions of below 10 nm. The crystallinity of the obtained HA was highest for pure HA and lowest for SeO_3-HA [41].

The powder diffraction method was also used in [34,37–39,44,46] to confirm the obtaining of monophasic HA material. The widening of reflections was observed as selenite concentration increased, which indicates a decrease in the size of crystallites, as well as a decrease in crystallinity [34,38]. The sizes of the SeO_3-HA crystallites, calculated using the same method as in [46], are approximately 20 nm and are not much smaller than in pure, unsubstituted HA. A decrease in crystallite size along the *c* axis with an increase in Se concentration was also observed in the HA-lysozyme composites [39].

Ma et al. [45] attempted the almost total exchange of phosphate ions for selenite. Based on a comparison with the reference diffractogram, the behaviour of the hydroxyapatite monophase was determined to be highest at an Se:P ratio of below 10 [45]. At higher concentrations, reflections characteristic of calcium selenite were observed [45]. In the samples in which the HA structure was preserved, the lines were significantly widened.

Similar results were achieved by Wei et al. [33]. They observed the reflections from the HA phase on the diffractogram in samples with a molar Se:P ratio of a maximum of 0.3 (Figure 4). In samples with a Se:P value > 1, reflections from calcium selenite were observed. The paper also describes samples that were heated at a temperature range from 700 to 1200 °C, which resulted in the sharpening of reflections, proving that the crystallinity of samples increased. In some samples heated at temperatures between 1100 and 1200 °C, the occurrence of the β-TCP phase was noticed [33].

Zhang et al. also confirmed the production of SeO_3-HA in all samples using the PXRD method. The calculated crystallite size decreased from 45.3 to 17.4 nm [42]. As in other studies, it was noticed that the reflections became wider with increasing selenium concentrations. The results obtained with the PXRD method were additionally confirmed by the SAED electron diffraction method [42].

Samples of SeO_3-HA obtained by the solvothermal method, with 15–40% of the phosphate ions being exchanged for selenite, have reflections typical of HA [35]. In the sample with 55% P exchanged for Se, additional reflections were noted from the calcium selenite [35].

Uskokovic et al. [47] confirmed the achievement of a monophasic hydroxyapatite material for samples with concentrations of SeO_3^{2-} ions ranging from 0.1% to 1.9%. However, the sample with SeO_3^{2-} concentration of 3% additionally contained reflections from the calcium pyrophosphate phase (β-$Ca_2P_2O_7$), which became visible only after calcination at 800 °C. The widening of reflections with increased SeO_3^{2-} ion content was also noticed [47]. The authors suggest that the decrease in crystallinity with an increase in the content of selenium ions is caused by an uneven dissolution rate in various environments. In an acidic environment, much more Ca^{2+} ions than PO_4^{3-} ones are released, while in an alkaline environment, this mechanism is reversed. However, during the formation of HA, the first stage is the creation of a phosphate-based lattice with incorporated calcium ions, and this process is promoted by a higher concentration of phosphate ions. In turn, the replacement of some of phosphate ions with selenium ions during synthesis reduces the concentration of PO_4^{3-} ions, which causes the disturbance of the structure growth and as a result, the macro structure

is disturbed (long-range order). In addition, this may hinder recrystallization, as a result of which the amorphous particles change into larger crystalline structures. The result of this is that the transformation and preservation of the amorphous structure is inhibited. The authors see another possible cause of structural disruption, i.e., only a few double-charged SeO_3^{2-} ions are incorporated into the crystal structure.

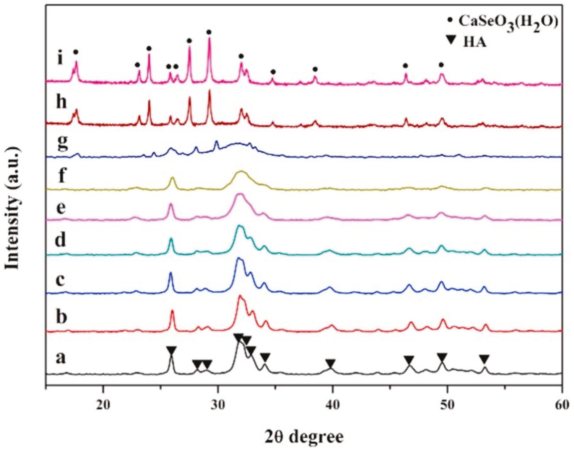

Figure 4. XRD patterns of the pure HA and Se-HA samples with different Se/P ratios: (**a**) HA; (**b**) Se/P = 0.05; (**c**) Se/P = 0.08; (**d**) Se/P = 0.1; (**e**) Se/P = 0.3; (**f**) Se/P = 0.5; (**g**) Se/P = 1; (**h**) Se/P = 3; and (**i**) Se/P = 5. Reprinted from [33] with permission from Elsevier.

Based on the above-described diffractograms, the crystallite size for samples obtained by both co-precipitated and post-precipitated methods [47]. In both types of samples, the incorporation of selenite ions causes a decrease in the size of crystallites, but this is not correlated with the content of these ions in the sample [47].

Coatings obtained by soaking in SBF were analysed using the PXRD method and they were then compared with the reference HA diffractogram [55]. The reflections for the obtained HA and SeO_4-HA coatings are typical of amorphous HA; they have wide lines with a position characteristic of the HA phase. Since the width of the reflections on the diffractogram of the SeO_4-HA coating does not differ from the reflections of the HA coating, the authors claim that both materials have a similar crystallinity.

3.2. Examinations Using Electron Microscopy Methods (SEM, TEM)

Electron microscopy is a frequently used method when analysing materials with a crystalline structure, since it allows for an evaluation of the morphology and size of the crystals. The materials obtained in [36,43] had plate-shaped nanometre crystals; their dimensions did not exceed 10 nm in width and 30 nm in length [43]. The crystals were characterized by a strong tendency to form dense agglomerates. In turn, Wang et al. obtained crystallites similar in shape to needles during the synthesis of SeO_3-HA, through the linear aggregation of single crystallites [38]. The dimensions of such nanoparticles were determined, based on TEM images, to be 20–30 nm in width and 150–200 nm in length [38,44,46]. Examinations of the size of nanoparticles using the dynamic light scattering (DLS) method indicated that there was a minimal increase in particle size in samples containing selenium ions, that it caused by a high tendency to agglomerate [38,56].

In the study [37], the synthesis method was modified by adding a dispersant, which enabled the formation of needle-shaped crystals with dimensions of below 100 nm, as confirmed by DLS and TEM measurements.

TEM and SEM images of a composite based on SeO_3-HA and silk fibres showed that in the samples without selenite ions, the crystals agglomerated as polycrystalline bamboo-shaped needle bundles [34], while the sample containing 6% selenium also contained needle-shaped crystals; however, they were more clustered and proteins derived from silk fibres covered the surface of the polycrystal like a thin film. For samples with higher concentrations of selenium, a related ribbon structure with the appearance of a large grid was observed [34]. Structural disorders were also noticed in the form of separated large crystals. Simultaneous SEM images confirmed that silk fibres covered the surface of polycrystalline HA, forming a porous grid structure [34].

In contrast, HA-lysozyme composites [39] obtained by Wang et al. had narrow, sharp needles which tended to agglomerate; the dimensions, measured based on TEM images, were 10–25 nm in width and 120–150 nm in length.

Photographs taken using the field emission scanning electron microscopy (FE-SEM) method show the very irregular surfaces of composites that can be formed during the drying process, when the water molecules evaporate from the loosely adhesive interface. Images taken with this method also indicate the agglomeration of nanocomplexes.

Needle crystals were obtained in the study [40]. It was also observed that an increase in selenium content increased the size of the crystals and intensified their agglomeration [40].

The shape of the 150–200 nm long needles was recorded in TEM images by Wei et al. [33]. The authors compared samples with the Se:P molar ratios of 0.3 and 0.5, and noticed that an amorphous fraction appeared on the surface of crystals in a sample with a higher selenium content, which was confirmed by results obtained using the PXRD method.

Zhang et al. obtained rod-like crystals using the hydrothermal method, and based on SEM and TEM images, their length and width were measured to be 50 and 12 nm, respectively [42].

However, the use of the solvothermal method resulted in rod-like nanoparticles with dimensions of 8 to 150 nm [35]. Low concentrations of selenium (up to 15%) exchanged with P caused the rods to narrow and the ends to tighten, while an increase in the content of incorporated selenium to 40% caused a change in shape, where the rods transformed into needles of up to 100 nm in length. The authors of the study [35] also verified that the reaction temperature had an influence on the morphology of the nanoparticles. After reducing the reaction temperature to 100 °C, the obtained nanoparticles were shaped like rods. On the other hand, gradually raising the temperature to 200 °C resulted in the particles maintaining their length but gradually becoming narrower.

Uskokovic et al. compared images of pure HA and SeO_3-HA recorded using the TEM method, and noted that pure HA is composed of two types of crystals with particles of approximately 5 nm and elongated crystals with dimensions of 10–15 nm × 50–100 nm [47]. The coexistence of the two forms is indicative of aggregative crystal growth and is the result of the tendency to grow mainly along the *c* axis of the crystal. In contrast, SeO_3-HA obtained using the wet method had homogeneous grains measuring 20–50 nm in diameter. This is probably due to the fact that SeO_3^{2-} ions block the aggregation of small particles into more crystalline needles, which causes the resulting SeO_3-HA to be less crystalline than pure HA.

The HA and SeO_3-HA coatings obtained by the PLD method on Ti and Si materials were analysed by SEM [54]. The researchers described the surface morphology as being typical of HA, consisting of spherically shaped aggregates; moreover, the similarity of the HA and SeO_3-HA coatings indicated a similar mechanism of formation by globular groupings.

Coatings deposited using SBF doped with selenium ions were analysed based on field emission FE-SEM images [55]. The researchers noticed the first calcium phosphate compounds after four days. It turned out that, after 14 days of soaking, the whole surface was covered with semicircular compact SeO_4-HA with a homogeneous morphology. When comparing the coatings, the authors noticed that their thickness increased with longer soaking times, and that the coating based on Se-doped SBF was more homogeneous [55].

3.3. Examinations Using Mid-Infrared Spectroscopy (FT-IR)

HA samples doped with selenium were analysed using mid-infrared spectroscopy in the range of 4000–400 cm^{-1} [36,38,43,45,46]. Based on the reference spectrum of hydroxyapatite, the occurrence of HA-specific bands was confirmed (see Table 1). Additionally, Kolmas et al. [36,43] recorded two bands at 767 cm^{-1} and 840 cm^{-1} on mid-infrared spectra for HA doped with SeO_3^{2-} ions, the intensity of which increased with the content of selenite ions (Figure 5). These bands were assigned to symmetrical and asymmetrical vibrations of the Se–O bond of selenite ions in HA crystals. In turn, a band at approximately 505 cm^{-1} was attributed to bending vibrations [43]. For the HA doped with selenate ions, an additional band at 910 cm^{-1} was recorded that was not observed on the pure HA spectrum, which was attributed to the Se-O stretching vibrations of the SeO_4^{2-} group. Based on the location of these bands, the authors confirmed that selenite and selenate ions had become incorporated into the structure of HA crystals.

Table 1. Main FT-IR bands of HA [36,38,43,45,46].

Bands (Wavenumber cm^{-1})	Assignment
3700–2500	ν_3 and ν_1 stretching modes of hydrogen-bonded H_2O molecules
3570	stretching modes of structural hydroxyl groups
1630–1640	Bending modes of hydrogen-bonded H_2O molecules
1200–900	ν_3 and ν_1 of PO_4^{3-}
605–500	ν_4 PO_4^{3-}
475–470	ν_2 PO_4^{3-}

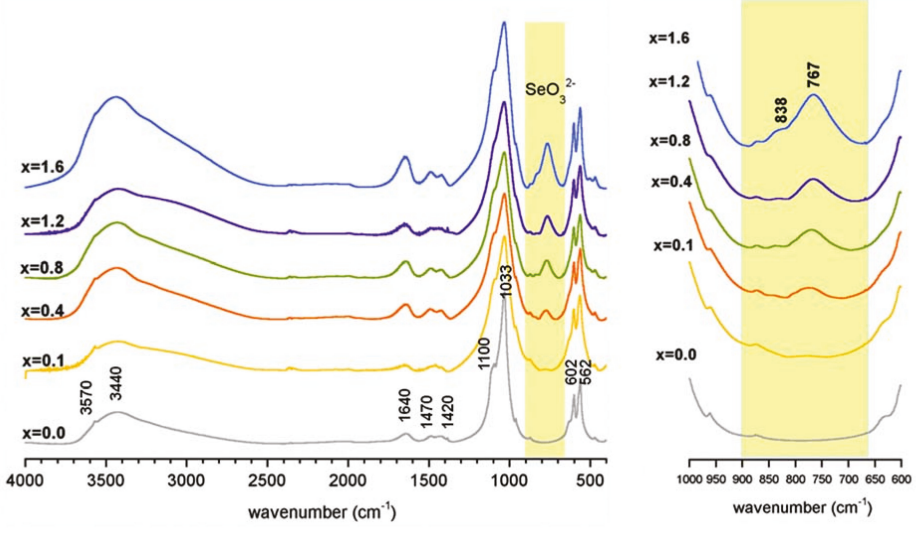

Figure 5. The FT-IR transmission spectra of the studied selenite-doped HA (HA-$x$$SeO_3$) and HA undoped. Reprinted from [43] with permission from Elsevier.

Wang et al. [46] recorded signals assigned to the phosphate and hydroxyl groups in the spectra, confirming that they were receiving SeO_3-HA. The authors distinguished 1460 and 1420 cm^{-1} signals, indicating the presence of carbonates in the samples. Moreover, the signal at 784 cm^{-1} confirmed the incorporation of the SeO_3^{2-} ions, while the 874 cm^{-1} signal was assigned to selenite and carbonate ions. All bands derived from selenite and carbonate ions increased as the Se:P concentration increased.

In [38], the same bands were observed, but attention was paid to the significant reduction of the bands from the hydroxyl groups at 3570 and 630 cm^{-1} when compared with the pure HA spectrum.

Ma et al. [45] noted that, as the selenium ion content increased, there was a reduction in the strong bands attributed to the symmetrical and antisymmetric vibrations of the P–O bond in the 1200–900 cm^{-1} range, as well as in the bands of asymmetrical bending vibrations of the O–P–O bonds (bands at 604 and 567 cm^{-1}). They also noticed that, despite the incorporation of selenite ions, bands derived from phosphate groups were unaffected. However, the position of both the stretching and bending bands was obviously unaffected by the selenite substitutions. Similarly, when the Se:P ratio increased, the content of B-type carbonates decreased (bands at 1456 and 1413 cm^{-1}), while the intensity of the band at 1564 cm^{-1}, derived from A-type carbonates in the SeO_3-HA samples, was higher than the intensity of the bands derived from B-type carbonates. The most intense bands from selenite appeared in the 900–800 cm^{-1} range, and originated from antisymmetric stretching vibrations, while the 766 cm^{-1} band originating from the bending vibrations of O–Se–O bonds increased as the Se concentration also increased.

On the recorded FT-IR spectra, Zhang et al. observed bands that were typical of HA, which originated from phosphates, carbonates, water and hydroxyl groups. They additionally recorded bands at 869 cm^{-1} and 775 cm^{-1}, which they assigned to the antisymmetric stretching vibrations of SeO_4 tetrahedron and bending vibrations (ν_3) O–Se–O [42].

In the studies [33,35,40], it was observed that the intensity of the band originating from the structural vibrations of OH groups at 3570 cm^{-1} decreased as the Se concentration increased. The authors [35] assigned the bands 767 and 712 cm^{-1} to the symmetric stretching vibrations (ν_3) of the selenite group. Moreover, when the concentration of selenite ions increased, the 856 and 823 cm^{-1} signals corresponding to the ν_1 and ν_3 vibrations of the SeO_3^{2-} group became stronger.

The spectra also showed bands derived from C–H, $–CH_2^-$, and COO^- groups from oleic acid, which indicates that the samples were covered in this acid [35].

Liu et al. [40] observed a band originating from the vibrations of selenite groups at 766 cm^{-1}. This signal was observed for the first time with a sample containing a planned content of 3% Se, and it increased as the selenium content increased. There was also an increase in the intensity of the bands from CO_3^{2-} ions in the 1418–1566 cm^{-1} range, along with an increase in selenium content, which was probably caused by the facilitation of CO_3^{2-} group incorporation as the crystallinity of the samples decreased.

The examination of SeO_3-HA coatings obtained by the PDL method confirmed the occurrence of HA-specific water bands, as well as phosphate and carbonate groups. It was also observed that, as the coatings increased in terms of Se content, not only did the bands from carbonates decrease, but the main band from phosphate groups (antisymmetric stretching) also decreased and its half-width increased. There was also a simultaneous loss of definition in the bending bands from the PO_4^{3-} group, as well as shift of the main phosphate band from 1040 cm^{-1} for the pure HA coating to about 1063 cm^{-1} for the coating containing the highest concentration of selenium. This band shift was caused by a change in the length of bonds, which was a consequence of the incorporation of Se ions [54].

3.4. Examinations Using the Raman Spectroscopy Method

Studies on samples of hydroxyapatites doped with selenium ions, conducted using Raman spectroscopy, have been described by several authors.

When comparing coatings with pure HA and SeO_3-HA, obtained using the PLD method, in material doped with Se ions, signals that were characteristic of phosphates were confirmed: the they were strongest at 960 cm^{-1} from bending vibrations (ν_1), at about 1070 cm^{-1} from stretching vibrations (ν_3), at 590 cm^{-1} from bending vibrations (ν_2), at 430 cm^{-1} from bending vibrations (ν_2) and symmetric stretching bands (ν_1) and at 1064 cm^{-1} derived from carbonate groups. In addition, a band of approximately 830 cm^{-1} originating from the symmetric stretching vibrations of the SeO_3^{2-} groups was registered for the SeO_3-HA coatings [54].

Kolmas et al. recorded three bands at 911, 873, and 843 cm^{-1} for the sample doped with SeO_4^{2-} ions, which was assigned to selenate ions [43].

In contrast, Yilmaz et al. [55] examined the SeO_4-HA coating using Raman spectroscopy. In addition to the bands characteristic of phosphates at 1072, 961, 590, and 429 cm^{-1}, as well as bands originating from the substrate at 629, 270, 209, and 136 cm^{-1} in a sample soaked for 14 days in a 1.5 × SBF doped with Se ions, a weak signal from selenates was also observed at 764 cm^{-1} [55].

3.5. Examinations Using Nuclear Magnetic Resonance Spectroscopy (NMR)

Kolmas et al. [41] subjected the obtained samples of HA doped with SeO_3^{2-} and SeO_4^{2-} selenium ions to ssNMR examination. Spectra were recorded for the nuclei ^{31}P, ^{1}H, and ^{77}Se.

The ^{31}P spectra were recorded using two techniques: one-pulse (Bloch-decay, BD) and 1H→31P cross-polarization (CP). One signal characteristic of hydroxyapatite samples at about 3 ppm was recorded on the spectra. It was noted that the signal in the ^{31}P BD NMR spectra was narrowest for the pure HA sample and widest for the SeO_3-HA sample; moreover, because the line width was correlated with the crystallinity of the sample, this was indicative of its reduction in the selenium-doped samples.

The signal in the ^{31}P CP NMR spectra was deconvoluted into two components: narrow, derived from phosphate groups inside the crystal located near the protons of structural hydroxyl groups, and broad, derived from phosphate groups located near to the water-rich environment (especially from phosphors from the hydrated surface layer) [41,57]. The wide component was relatively the most intense in the spectrum of the sample containing SeO_3^{2-}, indicating a more extensive hydrated surface layer and, thus, a more developed surface. In all of the recorded ^{1}H MAS NMR spectra, two signals can be distinguished at about 0 and 5.4 ppm. The signal at about 0 ppm comes from structural hydroxyl groups. The OH groups form columns in the channels, but they are so far apart that it is impossible to create hydrogen bonds between them. In spectra registered for samples doped with selenium, the chemical shift of this signal moved toward positive values, which were highest in the sample containing selenites. The widening of the signal in the Se-HA samples was also observed to be more significant than the signal from pure HA. The authors suggest that, due to the incorporation of selenium ions into the hydroxyapatite structure, the column structure of the OH group became disturbed, resulting in the formation of weak hydrogen bonds. The content of structural hydroxyl groups was calculated, and it was observed that there was a significant loss of HA crystals with incorporated selenite ions (49% OH groups relative to stoichiometric HA) and selenate (63%) when compared to pure HA (77%). It was also proven that this reduction in the content of structural hydroxyl groups was related to the decreased size of the crystals [43,57] due to the absorption of water from the crystals' surface into the columns of the hydroxyl groups. Thus, the authors postulate that the reason for the loss of structural hydroxyl groups is two-fold: not only are OH groups removed during substitution, but also water is present in the OH columns [41].

The signal at about 5.4 ppm is attributed to water adsorbed onto the surface of the crystals. The spectra for the ^{77}Se nucleus were recorded using the $^{1}H→^{77}Se$ CP technique. The obtained spectra for the HA containing selenates showed two intense signals at 1045 ppm, and a much weaker one at 1027 ppm. Furthermore, for the sample containing selenites, there was an analogously strong signal at 1310 ppm and a weaker one at 1325 ppm. It was proven that the strong signals on both spectra originated from selenium ions embedded in the crystalline lattice of the crystal, while the lower intensity signals were derived from selenates and selenites in the hydrated surface layer.

4. Biological Examinations of Hydroxyapatite Materials Doped with Selenium

Biological examinations of HA materials containing selenium have focused primarily on the determination of their antibacterial, anticancer, and cytotoxic effects, as well as their influence on the development of bone tissue. In addition to in vitro studies, some research groups have also

conducted experiments using an in vivo animal model (mice or rats). Below, we will try to illuminate the results and conclusions from the studies.

4.1. Antibacterial Activity

Studies to determine the antibacterial activity of SeO_3-HA and SeO_4–HA were carried out on the following bacterial strains: *Staphylococcus aureus*, *Pseudomonas aeruginosa*, *Staphylococcus epidermidis*, *Escherichia coli*, and *Salmonella enteritidis*. This is because they are the bacteria that contribute most often to infections during orthopaedic surgery. *S. aureus* is of particular note, as it is a very common pathogen that causes infections during bone implantation due to the ease of biofilm formation and the presence of numerous antibiotic-resistant strains.

Measurements of antibacterial activity have typically been performed through determining the optical density of the bacterial suspension, counting the CFUs attached to the material, determining the area of inhibition using the disk diffusion method, or evaluating biofilm formation. The measurements were taken after the bacteria had been incubating for an appropriate length of time on the growth medium in the presence of the examined materials.

In the case of *S. aureus*, all of the studies [47,53,54,58,59] observed that SeO_3-HA materials significantly reduced bacterial viability, inhibiting both their growth and biofilm formation, when compared to the control and samples with pure HA. According to the study by Rodríguez-Valencia [54], the introduction of 0.6 wt % of selenium ions into the HA structure was already sufficient to inhibit the formation of an *S. aureus* biofilm (as well as *P. aeruginosa*) (Figure 6).

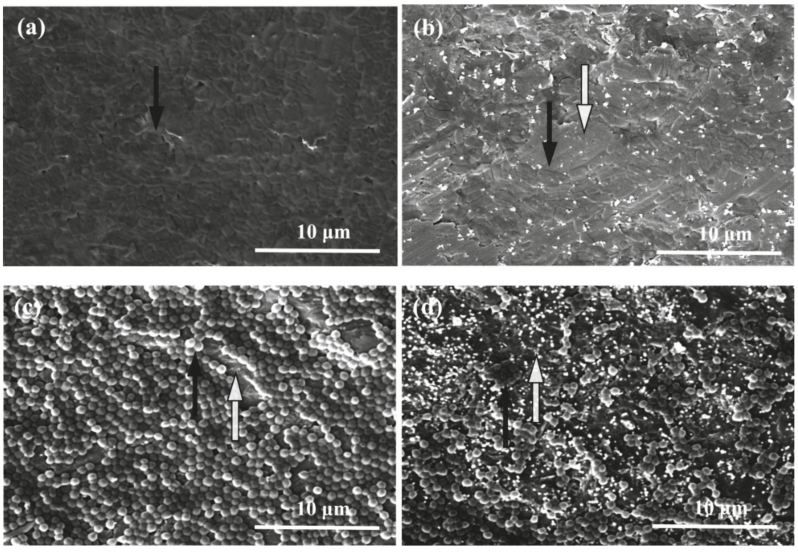

Figure 6. SEM micrographs of the aspect of the biofilm after inoculating *P. aeruginosa* (**a** and **b**) and *S. aureus* (**c** and **d**) on the RHA2.5Se (**b** and **d**) coatings compared to HA (**a** and **c**). White arrows indicate non-colonized areas and black ones indicate the shape of an exemplar of that bacterium. Reprinted from [54] with permission from John Wiley and Sons.

Additionally, according to Uskokovic [47], despite the antibacterial effect of the SeO_3-HA material on *S. aureus*, these properties were lost over time and the bacterial population returned to a level similar to that observed in the negative control group. This may indicate that those *S. aureus* bacteria that survived their initial exposure to SeO_3-HA did not later show susceptibility to SeO_3^{2-} ions, which allowed the population to rebuild.

The results of studies carried out on *E. coli* bacteria are interesting. These bacteria are characterized by their ability to reduce SeO_3^{2-} ions to Se^0, which they can then use to synthesize the amino acids selenocysteine and selenomethionine. Due to this fact, the level of SeO_3^{2-} ion concentration will determine whether *E. coli* growth is stimulated or inhibited. According to the study carried out by Kolmas [58], a selenium content of 3.6 wt % in the HA structure was insufficient to inhibit the growth of *E. coli*. In turn, according to Murugan [59], there was a decrease in the functioning and lifespan of bacteria at all applied concentrations of SeO_3-HA, which was further confirmed by the study of Uskokovic [47], in which *E. coli* bacteria were still sensitive to the examined biomaterial 72 h after the start of incubation at the highest level of selenium content in the analysed SeO_3-HA material (1.92 wt % and 3 wt %).

It is worth emphasizing that studies performed on both *E. coli* and *S. aureus* [47,59] indicate that the SeO_3-HA material has a stronger effect on these strains than on the first of the mentioned strains. This may be due to the presence of a thinner layer of peptidoglycan in the cell wall in Gram-negative bacteria, which makes it easier for the active substance to penetrate inside the cell.

According to Rodríguez-Valencia [53], as the selenium content in SeO_3-HA increased, there was a gradual increase in its antibacterial activity against *S. epidermidis* and a gradual inhibition of biofilm formation until it completely disappeared 72 h after the start of incubation. This was confirmed by the study of Yilmaz [55], in which a significant decrease in optical density was observed after 72 h of incubation in a sample with an SeO_4_HA-coated titanium implant, as compared with a sample with an uncoated implant, one with a pure HA coated implant and the control sample.

Antimicrobial activity was also tested for the strains *P. aeruginosa* and *S. enteritidis*. The results of the studies confirmed the effectiveness of SeO_3-HA in inhibiting the growth of these microorganisms by [47,54].

In conclusion, the studies carried out confirmed that HA material containing selenium has an antibacterial effect on individual bacterial strains. The antibacterial effect of this biomaterial is based on inducing the formation of reactive oxygen species in a bacterial cell. According to Kramer and Seko [60,61], oxidation and reduction reactions which occur during selenium metabolism lead to the formation of hydrogen peroxide and superoxide (i.e., reactive oxygen species), which, in turn, contribute to oxidative stress and damage to the bacterial cell wall. It is worth noting that the antibacterial effect of SeO_3-HA is stronger for Gram-negative bacteria than it is for Gram-positive ones [47,59], while the adsorption of antibiotics on the surface of SeO_3-HA (e.g., vancomycin) increases the obtained antibacterial properties [47].

4.2. Anticancer, Cytotoxic, and Osteoinductive Effects

The main assumption during the synthesis of hydroxyapatite materials doped with selenium is that biomaterial will be obtained that will effectively inhibit the development of bone cancers, while showing no cytotoxic activity on healthy tissue. Another important feature of this material is its ability to induce osteogenesis in order to stimulate bone tissue reconstruction at the site of a bone defect.

In vitro studies were performed on healthy mouse cells (mouse MC3T3-E1 preosteoblasts and mouse fibroblasts collected from the lungs), healthy human cells (human foetal hFOB osteoblasts, bone marrow stromal cells (BMSC) and human fibroblasts), mouse cancer cells (murine ATCC osteosarcoma cells and K7M2), and human cancer cells (human MG−63 osteosarcoma cells, Saos-2, and MNNG/HOS). In vivo studies were performed on Wistar rats and BALB/c mice.

4.2.1. In Vitro Studies

In vitro tests on healthy cells primarily allowed for an evaluation of the biocompatibility of the discussed material, as well as its osteogenic properties. A study on biocomposites constructed from SeO_3-HA and silk fibrin (SF/Se-HA), carried out by Wang [34] on BMSC cells, clearly indicated that the presence of selenium in the biomaterial increased the intensity of cell population growth on

days one to seven from the start of the study compared to the control group and SF/HA sample, in which a relatively slow increase in cell population growth was observed. In addition, after seven days of incubation, the observed cell density was highest for the biomaterial samples with the highest selenium content. An increase in selenium content resulted in an increase in the rate of osteoblast proliferation, which was additionally confirmed by Vekariya's study [62]. In turn, the study on the effect of SeO_3-HA materials on MC3T3-E1 cells, carried out by Jianpeng [35], allowed for an assessment of cytotoxicity with respect to healthy cells. They analysed the effect of two SeO_3-HA materials with a ratio of Se:(P + Se) of 0.05 and 0.1, respectively (using different concentrations of the examined materials). In this case, not only was no cytotoxic activity observed in the sample containing the material with the highest selenium concentration, but it was also found to have a greater beneficial effect on the viability of MC3T3-E1 cells than in the case of pure HA samples. Rodríguez-Valencia's studies [53,54] confirmed the lack of cytotoxic activity of SeO_3-HA, where cell viability in the samples containing SeO_3-HA was at a similar or even a higher level than in the pure HA samples. The morphology of the MC3T3-E1 cells also did not change with incubation time [35,54]; numerous filopodia and lamellipodia could be observed in the cell structure, which enabled them to spread on the surface of the biomaterial [54]. This confirmed the biocompatibility of SeO_3-HA material with mouse preosteoblasts cells. The activity of osteoblasts was also analysed in studies carried out by Rodríguez-Valencia [53] and Uskokovic [47]. It was shown that osteoblastic activity also increased with incubation time and with increased selenium content in HA materials. Differences in the results were due to the selenium concentrations in the HA material, where osteoblastic activity was highest at higher selenium concentrations. For the first study, this was observed for sample containing the highest concentration (2.7 wt %) of selenium in the HA, while in the second study, this activity was highest at a concentration of 1.23 wt % and decreased when the selenium content increased any higher than this value. At the highest selenium concentration used (3 wt %), osteoblastic activity was significantly inhibited when compared with the pure HA sample, abnormalities in the cells' structure were visible and some of them died within the first 24 h of incubation. This was due to the effect of selenium on ROS generation and, thus, on the level of oxidative stress in osteoblasts. A suitable amount of selenium enabled the maintenance of oxidative stress at a level where it was able to exert a beneficial effect on osteoblastic activity; however, too much of this element had the effect of increasing oxidative stress to a level at which apoptotic pathways were activated [63–66].

In vitro tests carried out on cancer cells facilitated the determination of the anticancer efficacy of the examined biomaterials. In virtually every case, these tests were carried out in parallel with studies on healthy cells, which led to a fuller picture of the biomaterial activity. Studies conducted by Wang [34,46] and Uskokovic [47] showed that SeO_3-HA material had no effect on the viability and proliferation of healthy cells, while it inhibited the growth and reduced the viability of cancer cells (compared to the control group or HA sample). The effect of SeO_3-HA on osteosarcoma cells was stronger at higher selenium levels. The studies of Kolmas [36] and Yilmaz [55] confirmed the abovementioned effect of SeO_3-HA (and SeO_4-HA) on cancer cells; however, their results also indicated inhibition of growth and the reduction of viability of healthy cells. According to Kolmas [36], this was due to the so-called "burst release" of selenium ions from the biomaterial surface during the first 10 h following the beginning of the study, leading to a high concentration of selenium ions and, thus, causing the effective reduction of viability of both cancer cells and healthy osteoblasts.

Wang [46] confirmed that the anticancer effect of SeO_3-HA is due to the induction of apoptosis in cancer cells. In order to illuminate the mechanism of its anticancer activity, both Wang [46] and Wang [37] (convergence of names) performed a number of studies. They both measured the fluorescence intensity of the ROS marker to determine whether SeO_3-HA causes an increase in the amount of reactive oxygen species generated. The results of both studies confirmed the above dependence. In other words, they found that Se-HA enhanced the formation of intracellular ROS, which in turn induced apoptosis and activated caspases. Caspase-3 is a key factor in the apoptosis process and is activated by caspase-8 and caspase-9, which initiate two different apoptotic pathways:

the caspase-8 extrinsic and the caspase-9 intrinsic apoptotic pathways. In his study, Wang [37] confirmed the presence of activated caspase-3 and caspase-8 and caspase-9 in samples with a high selenium content (not only in the sample with Se-HA, but also in the one with Na_2SeO_3), which clearly indicated that that caspase-dependent apoptosis was associated with the presence of high selenium content (see Figure 7).

Finally, it is worth mentioning the study performed by Kolmas [43], which tested the toxicity of HA material doped with SeO_3^{2-} or SeO_4^{2-} ions in *Vibrio fisheri* bacteria and *Spirostomum ambiguum* protozoa. The results indicated that SeO_3^{2-} ions were toxic to a certain degree for both microorganisms, while this effect was not visible in the case of SeO_4^{2-} ions, which may indicate that selenate ions (VI) are less toxic than selenite ions (IV).

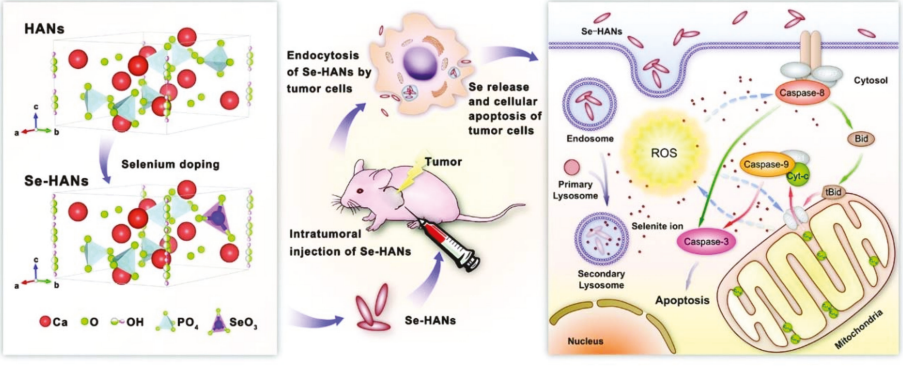

Figure 7. Preparation and working principle of antitumor nanoparticles. Se-HANs were fabricated using selenite to replace phosphate of HANs. Intratumoral injection of Se-HANs was performed on the xenograft osteosarcoma model. Se-HANs were internalized into tumor cells by nonspecific endocytosis and rapidly degraded in the acidic lysosome to release selenium. Cell apoptosis was activated by a primary, selenium-induced, caspase-dependent apoptosis pathway synergistically orchestrated with the ROS generation. Reprinted from [37] with permission. Copyright (2016) American Chemical Society.

4.2.2. In Vivo Studies

In in vivo studies on Wistar rats, Wang [44] applied the examined biomaterials in previously prepared skull bone defects. These materials were a biocomposite made of hydroxyapatite and chitosan (HA/Ch) and the biocomposite SeO_3-HA/Ch. The control group was made up of rats with a cranial bone defect, and no biomaterials were applied in this group. No complications were observed with the graft, and all of the rats survived until the day of euthanasia (which took place four, eight, or 12 weeks after implantation). The histological examination showed that there was inflammation within the graft or necrosis of the tissue, which was indicative of the biocompatibility of the material with the tissue (this was due, inter alia, to the high porosity of the material). The scaffolding created by the implant began to partially degrade eight weeks after implantation. It was replaced by newly-formed bone tissue, which, however, was less abundant than in the control group. Twelve weeks after implantation, an increasing number of bone connections between the host bone and the implant could be observed in groups with SeO_3-HA/Ch and HA/Ch biomaterials. In addition, in the case of SeO_3-HA/Ch, larger quantities of stromal cells, ossein, and fibrous cartilage cells were visible within the defect. Furthermore, it should be noted that characteristic polymorphonuclear cells were present, which supported the formation of new bones in the sample with SeO_3-HA/Ch [67]. In addition, for the SeO_3-HA/Ch group, the formation of new blood vessels was visible (neovascularization). The determination of calcein in all of the implantable materials tested was performed 12 weeks after

implantation. The introduction of selenium into the structure resulted in the recruitment of progenitor cells and osteoclasts, which had a positive effect on scaffold degradation and bone remodelling. However, it is difficult to obtain a complete bone-width between the material and the host bone by osteogenesis and neovascularization. According to [68,69], a significant amount of time is needed to bind HA to the host bone, so more research is needed to confirm this. Basing their results on the number of bone beams, Wang [37] also stated that bone quality was higher in the SeO_3-HA/Ch group, since this parameter was highest in this sample.

In turn, Wang [37] carried out an in vivo study on osteosarcoma cells in BALB/c mice. In addition to applying SeO_3-HA materials with different levels of selenium content, control groups were prepared, which were HA solutions with various amounts of Na_2SeO_3 added. For the sample of SeO_3-HA material with the highest selenium content, the author found that cancer growth was inhibited and the volume and weight of tumours were reduced. The control group sample with an identical selenium concentration gave a similar result. Although all of the mice survived until the end of the experiment without any visible changes in body weight, the analysis of various biochemical parameters (AST, BUN, CREA, and LDH) indicated differences between the various groups in terms of systemic toxicity. It should be taken into account that in vivo toxicity may have decreased under the influence of selenium ions by inducing apoptosis in cancer cells, impairing the metabolism of these cells and protecting healthy tissues. On the other hand, too high a dose of selenium may cause side effects in terms of organ function in the examined mice, thus leading to increased toxicity. The toxicity level was lowest in the SeO_3-HA group with the highest selenium content, which was indicated by significantly reduced biochemical parameters. This may be explained by the gradual release of selenium from the SeO_3-HA material, which was additionally regulated by the acidic pH of the cancer tissue environment. Therefore, the concentration of selenium in the tumour was high, with a small quantity of selenium ions leaking out of the cancerous tissue. For the control group, where Na_2SeO_3 was mixed with HA, the whole substance immediately decomposed and spread beyond the cancer tissue into healthy tissues, which caused an increase in toxicity. Studies on healthy BALB/c mice confirmed the lack of toxicity of SeO_3-HA materials in comparison with the HA/Na_2SeO_3 control sample, which showed a significant increase in systemic toxicity. This means that the use of SeO_3-HA material enables the avoidance of selenium toxicity because it is gradually released from the material. Wang [37] also confirmed that the mechanism of the activity of SeO_3-HA materials in the in vivo model was analogous to that presented in in vitro studies.

Finally, it is worth mentioning that Wang [38] also showed the beneficial anticancer effects of SeO_3-HA material on hepatocellular carcinoma cells in a study on BALB/c mice, which increased the survival of the mice and improved their biochemical parameters.

5. Conclusions and Future Perspectives

Hydroxyapatite that contains selenium ions is a material with high application potential. The studies presented in this review have demonstrated that it is possible to introduce both IV and VI selenium ions into the interior of the crystals, preserving the hexagonal structure of the HA. The obtained crystals are nanocrystalline, with a strongly-developed specific surface and a tendency to form large agglomerations. IV and VI selenite ions can also be located in the hydrated surface layer and strongly adsorb onto the surface of HA crystals. Se-HA was successfully used to form composites with silk fibres, sodium alginate and lysozyme. The studies demonstrated that it has the ability to cover metallic implants. Biological tests confirmed the antibacterial activity of SeO_3-HA materials; however, it had a stronger effect on Gram-negative strains than Gram-positive ones. In vitro studies indicated the beneficial effect of apatite materials containing selenium on osteoblastic activity. However, it is worth noting that high concentrations of selenium caused a significant increase in the toxicity levels of normal cells. In vitro cancer cell research, supported by in vivo tests, clearly confirmed the inhibition of growth and the reduction of vitality.

These promising results obtained for hydroxyapatite materials containing selenium mean that the subject is still relevant. It is possible to find some attempts in the literature to synthesize co-substituted hydroxyapatites, e.g., those containing selenium IV ions along with Mn^{2+} manganese, Zn^{2+} zinc or Fe^{3+} iron ions [59,70,71]. There have also been attempts to use Se-HA to create systems for the delivery of medicinal substances to bone tissue, e.g., antiretroviral drugs (from the group of bisphosphonates) or antibiotics [36].

The future steps of the studies on Se-HA materials should be focused on appropriate selenium concentration causing low toxicity towards normal cells and sufficient toxicity towards cancer cells. Moreover, the physicochemical studies on selenium-doped materials should be continued. For example, thermal stability of Se-HA is not yet analysed. Next, bioceramics based on Se-HA materials should be developed.

The future research should also focus on multifunctional composite materials containing selenium-doped HA which could be used as drug delivery systems.

Acknowledgments: This work was supported by the research programme (UMO-2016/22/E/ST5/00564) of the National Science Center, Poland. Figure 7 was prepared using Vesta (K. Momma and F. Izumi, "VESTA 3 for three-dimensional visualization of crystal, volumetric and morphology data," J. Appl. Crystallogr., 44, 1272-1276 (2011).

Conflicts of Interest: The authors declare no conflict of interest.

References

1. Habraken, W.; Habibovic, P.; Epple, M.; Bohner, M. Calcium phosphates in biomedical applications: Materials for the future? *Mater. Today* **2016**, *19*, 69–87. [CrossRef]
2. Dorozhkin, S.V.; Epple, M. Biological and medical significance of calcium phosphates. *Angew. Chem. Int. Ed. Engl.* **2002**, *41*, 3130–3146. [CrossRef]
3. Miyazaki, T.; Kawashita, M. Electrochemical deposition of hydroxyapatite and its biomedical applications. In *Hydroxyapatite Coatings for Biomedical Applications*; Zhang, S., Ed.; CRC Press: Boca Raton, FL, USA, 2013; pp. 31–54.
4. Palazzo, B.; Sidoti, M.C.; Roveri, N.; Tampieri, A.; Sandri, M.; Bertolazzi, L.; Galbusera, F.; Dubini, G.; Vena, P.; Contro, R. Controlled drug delivery from porous hydroxyapatite grafts: An experimental and theoretical approach. *Mater. Sci. Eng. C* **2005**, *25*, 207–213. [CrossRef]
5. Sakae, T.; Nakada, H.; John, P.L. Historical review of biological apatite crystallography. *J. Hard Tissue Biol.* **2015**, *24*, 111–122. [CrossRef]
6. Kay, M.I.; Young, R.A.; Posner, A.S. Crystal structure of hydroxyapatite. *Nature* **1964**, *204*, 1050–1052. [CrossRef] [PubMed]
7. Šupová, M. Substituted hydroxyapatites for biomedical applications: A review. *Ceram. Int.* **2015**, *41*, 9203–9231. [CrossRef]
8. Szurkowska, K.; Kolmas, J. Hydroxyapatites enriched in silicon—Bioceramic materials for biomedical and pharmaceutical applications. *Prog. Nat. Sci. Mater. Int.* **2017**, *27*, 401–409. [CrossRef]
9. Kolmas, J.; Piotrowska, U.; Kuras, M.; Kurek, E. Effect of carbonate substitution on physicochemical and biological properties of silver containing hydroxyapatites. *Mater. Sci. Eng. C* **2017**, *74*, 124–130. [CrossRef] [PubMed]
10. Kieliszek, M.; Błażejak, S. Selenium: Significance and outlook for supplementation. *Nutrition* **2013**, *29*, 713–718. [CrossRef] [PubMed]
11. Fairweather-Tait, S.J.; Collings, R.; Hurst, R. Selenium bioavailability: Current knowledge and future research requirements. *Am. J. Clin. Nutr.* **2010**, *91*, 1484S–1491S. [CrossRef] [PubMed]
12. Lenz, M.; Lens, P.N.L. The essential toxin: The changing perception of selenium in environmental sciences. *Sci. Total Environ.* **2009**, *407*, 3620–3633. [CrossRef] [PubMed]
13. Navarro-Alarcon, M.; Cabrera-Vique, C. Selenium in food and the human body: A review. *Sci. Total Environ.* **2008**, *400*, 115–141. [CrossRef] [PubMed]
14. Wood, S.M.; Beckham, C.; Yosioka, A.; Darban, H.; Watson, R.R. β-carotene and selenium supplementation enhances immune response in aged humans. *Integr. Med.* **2000**, *2*, 85–92. [CrossRef]

15. Broome, C.S.; McArdle, F.; Kyle, J.A.M.; Andrews, F.; Lowe, N.M.; Hart, C.A.; Arthur, J.R.; Jackson, M.J. An increase in selenium intake improves immune function and poliovirus handling in adults with marginal selenium status. *Am. J. Clin. Nutr.* **2004**, *80*, 154–162. [CrossRef] [PubMed]
16. Hoffmann, F.W.; Hashimoto, A.C.; Shafer, L.A.; Dow, S.; Berry, M.J.; Hoffmann, P.R. Dietary selenium modulates activation and differentiation of CD4(+) T cells in mice through a mechanism involving cellular free thiols. *J. Nutr.* **2010**, *140*, 1155–1161. [CrossRef] [PubMed]
17. Ashrafi, M.R.; Shabanian, R.; Abbaskhanian, A.; Nasirian, A.; Ghofrani, M.; Mohammadi, M.; Zamani, G.R.; Kayhanidoost, Z.; Ebrahimi, S.; Pourpak, Z. Selenium and intractable epilepsy: Is there any correlation? *Pediatr. Neurol.* **2007**, *36*, 25–29. [CrossRef] [PubMed]
18. Burk, R.F.; Hill, K.E. Selenoprotein p—Expression, functions, and roles in mammals. *Biochim. Biophys. Acta (BBA)—Gen. Subj.* **2009**, *1790*, 1441–1447. [CrossRef] [PubMed]
19. Hawkes, W.C.; Turek, P.J. Effects of dietary selenium on sperm motility in healthy men. *J. Androl.* **2001**, *22*, 764–772. [PubMed]
20. Ursini, F.; Heim, S.; Kiess, M.; Maiorino, M.; Roveri, A.; Wissing, J.; Flohé, L. Dual function of the selenoprotein PHGPx during sperm maturation. *Science* **1999**, *285*, 1393–1396. [CrossRef] [PubMed]
21. Rayman, M.P. Selenium and human health. *Lancet* **2012**, *379*, 1256–1268. [CrossRef]
22. Contempré, B.; de Escobar, G.M.; Denef, J.-F.; Dumont, J.E.; Many, M.-C. Thiocyanate induces cell necrosis and fibrosis in selenium- and iodine-deficient rat thyroids: A potential experimental model for myxedematous endemic cretinism in Central Africa. *Endocrinology* **2004**, *145*, 994–1002. [CrossRef] [PubMed]
23. Helmersson, J.; Ärnlöv, J.; Vessby, B.; Larsson, A.; Alfthan, G.; Basu, S. Serum selenium predicts levels of F2-isoprostanes and prostaglandin F2α in a 27 year follow-up study of Swedish men. *Free Radic. Res.* **2005**, *39*, 763–770. [CrossRef] [PubMed]
24. Holben, D.H.; Smith, A.M. The diverse role of selenium within selenoproteins. *J. Am. Diet. Assoc.* **1999**, *99*, 836–843. [CrossRef]
25. Ju, W.; Li, X.; Li, Z.; Wu, G.R.; Fu, X.F.; Yang, X.M.; Zhang, X.Q.; Gao, X.B. The effect of selenium supplementation on coronary heart disease: A systematic review and meta-analysis of randomized controlled trials. *J. Trace Elem. Med. Biol.* **2017**, *44*, 8–16. [CrossRef] [PubMed]
26. Thomas, J.P.; Geiger, P.G.; Girotti, A. Lethal damage to endothelial cells by oxidized low density lipoprotein: Role of selenoperoxidases in cytoprotection against lipid hydroperoxide- and iron-mediated reactions. *J. Lipid Res.* **1993**, *34*, 479–490. [PubMed]
27. Czeczot, H.; Scibior, D.; Skrzycki, M.; Podsiad, M. Glutathione and GSH-dependent enzymes in patients with liver cirrhosis and hepatocellular carcinoma. *Acta Biochim. Pol.* **2006**, *53*, 237–242. [PubMed]
28. Schomburg, L. Dietary selenium and human health. *Nutrients* **2017**, *9*, 22. [CrossRef] [PubMed]
29. Moreno-Reyes, R.; Egrise, D.; Nève, J.; Pasteels, J.L.; Schoutens, A. Selenium deficiency-induced growth retardation is associated with an impaired bone metabolism and osteopenia. *J. Bone Miner. Res.* **2001**, *16*, 1556–1563. [CrossRef] [PubMed]
30. Xu, Z.S.; Wang, X.Y.; Xiao, D.M.; Hu, L.F.; Lu, M.; Wu, Z.Y.; Bian, J.S. Hydrogen sulfide protects MC3T3-E1 osteoblastic cells against H_2O_2-induced oxidative damage—Implications for the treatment of osteoporosis. *Free Radic. Biol. Med.* **2011**, *50*, 1314–1323. [CrossRef] [PubMed]
31. Zeng, H.; Cao, J.J.; Combs, G.F. Selenium in bone health: Roles in antioxidant protection and cell proliferation. *Nutrients* **2013**, *5*, 97–110. [CrossRef] [PubMed]
32. Hoeg, A.; Gogakos, A.; Murphy, E.; Mueller, S.; Köhrle, J.; Reid, D.M.; Glüer, C.C.; Felsenberg, D.; Roux, C.; Eastell, R.; et al. Bone turnover and bone mineral density are independently related to selenium status in healthy euthyroid postmenopausal women. *J. Clin. Endocrinol. Metab.* **2012**, *97*, 4061–4070. [CrossRef] [PubMed]
33. Wei, L.; Pang, D.; He, L.; Deng, C. Crystal structure analysis of selenium-doped hydroxyapatite samples and their thermal stability. *Ceram. Int.* **2017**, *43*, 16141–16148. [CrossRef]
34. Wang, Y.; Hao, H.; Zhang, S. Biomimetic coprecipitation of silk fibrin and calcium phosphate: Influence of selenite ions. *Biol. Trace Elem. Res.* **2017**, *178*, 338–347. [CrossRef] [PubMed]
35. Sun, J.; Zheng, X.; Li, H.; Fan, D.; Song, Z.; Ma, H.; Hua, X.; Hui, J. Monodisperse selenium-substituted hydroxyapatite: Controllable synthesis and biocompatibility. *Mater. Sci. Eng. C* **2017**, *73*, 596–602. [CrossRef] [PubMed]

36. Kolmas, J.; Pajor, K.; Pajchel, L.; Przekora, A.; Ginalska, G.; Oledzka, E.; Sobczak, M. Fabrication and physicochemical characterization of porous composite microgranules with selenium oxyanions and risedronate sodium for potential applications in bone tumors. *Int. J. Nanomed.* **2017**, *12*, 5633–5642. [CrossRef] [PubMed]
37. Wang, Y.; Wang, J.; Hao, H.; Cai, M.; Wang, S.; Ma, J.; Li, Y.; Mao, C.; Zhang, S. In vitro and in vivo mechanism of bone tumor inhibition by selenium-doped bone mineral nanoparticles. *ACS Nano* **2016**, *10*, 9927–9937. [CrossRef] [PubMed]
38. Yanhua, W.; Hao, H.; Li, Y.; Zhang, S. Selenium-substituted hydroxyapatite nanoparticles and their in vivo antitumor effect on hepatocellular carcinoma. *Colloids Surf. B Biointerfaces* **2016**, *140*, 297–306. [CrossRef] [PubMed]
39. Wang, Y.; Hao, H.; Zhang, S. Lysozyme loading and release from Se doped hydroxyapatite nanoparticles. *Mater. Sci. Eng. C* **2016**, *61*, 545–552. [CrossRef] [PubMed]
40. Liu, Y.; Ma, J.; Zhang, S. Synthesis and thermal stability of selenium-doped hydroxyapatite with different substitutions. *Front. Mater. Sci.* **2015**, *9*, 392–396. [CrossRef]
41. Kolmas, J.; Kuras, M.; Oledzka, E.; Sobczak, M. A solid-state NMR study of selenium substitution into nanocrystalline hydroxyapatite. *Int. J. Mol. Sci.* **2015**, *16*, 11452–11464. [CrossRef] [PubMed]
42. Zhang, W.; Chai, Y.; Cao, N.; Wang, Y. Synthesis and characterization of selenium substituted hydroxyapatite via a hydrothermal procedure. *Mater. Lett.* **2014**, *134*, 123–125. [CrossRef]
43. Kolmas, J.; Oledzka, E.; Sobczak, M.; Nałęcz-Jawecki, G. Nanocrystalline hydroxyapatite doped with selenium oxyanions: A new material for potential biomedical applications. *Mater. Sci. Eng. C* **2014**, *39*, 134–142. [CrossRef] [PubMed]
44. Wang, Y.; Lv, P.; Ma, Z.; Zhang, J. Enhanced healing of rat calvarial critical size defect with selenium-doped lamellar biocomposites. *Biol. Trace Elem. Res.* **2013**, *155*, 72–81. [CrossRef] [PubMed]
45. Ma, J.; Wang, Y.; Zhou, L.; Zhang, S. Preparation and characterization of selenite substituted hydroxyapatite. *Mater. Sci. Eng. C* **2013**, *33*, 440–445. [CrossRef] [PubMed]
46. Wang, Y.; Ma, J.; Zhou, L.; Chen, J.; Liu, Y.; Qiu, Z. Dual functional selenium-substituted hydroxyapatite. *Interface Focus* **2012**, *2*, 378–386. [CrossRef] [PubMed]
47. Uskokovic, V.; Iyer, M.A.; Wu, V.M. One ion to rule them all: The combined antibacterial, osteoinductive and anticancer properties of selenite-incorporated hydroxyapatite. *J. Mater. Chem. B* **2017**, *5*, 1430–1445. [CrossRef] [PubMed]
48. Renard, F.; Montes-Hernandez, G.; Ruiz-Agudo, E.; Putnis, C.V. Selenium incorporation into calcite and its effect on crystal growth: An atomic force microscopy study. *Chem. Geol.* **2013**, *340*, 151–161. [CrossRef]
49. Aurelio, G.; Fernández-Martínez, A.; Cuello, G.J.; Román-Ross, G.; Alliot, I.; Charlet, L. Structural study of selenium(IV) substitutions in calcite. *Chem. Geol.* **2010**, *270*, 249–256. [CrossRef]
50. Duc, M.; Lefevre, G.; Fedoroff, M.; Jeanjean, J.; Rouchaud, J.C.; Monteil-Rivera, F.; Dumonceau, J.; Milonjic, S. Sorption of selenium anionic species on apatites and iron oxides from aqueous solutions. *J. Environ. Radioact.* **2003**, *70*, 61–72. [CrossRef]
51. Monteil-Rivera, F.; Masset, S.; Dumonceau, J.; Fedoroff, M.; Jeanjean, J. Sorption of selenite ions on hydroxyapatite. *J. Mater. Sci. Lett.* **1999**, *18*, 1143–1145. [CrossRef]
52. Monteil-Rivera, F.; Fedoroff, M.; Jeanjean, J.; Minel, L.; Barthes, M.-G.; Dumonceau, J. Sorption of selenite (SeO_3^{2-}) on hydroxyapatite: An exchange process. *J. Colloid Interface Sci.* **2000**, *221*, 291–300. [CrossRef] [PubMed]
53. Rodríguez-Valencia, C.; Freixeiro, P.; Serra, J.; Ferreirós, C.M.; González, P.; López-Álvarez, M. In vitro evaluation of the antibacterial and osteogenic activity promoted by selenium-doped calcium phosphate coatings. *Biomed. Mater.* **2017**, *12*, 015028. [CrossRef] [PubMed]
54. Rodriguez-Valencia, C.; Lopez-Alvarez, M.; Cochon-Cores, B.; Pereiro, I.; Serra, J.; Gonzalez, P. Novel selenium-doped hydroxyapatite coatings for biomedical applications. *J. Biomed. Mater. Res. A* **2013**, *101*, 853–861. [CrossRef] [PubMed]
55. Yilmaz, B.; Evis, Z.; Tezcaner, A.; Banerjee, S. Surface characterization and biocompatibility of selenium-doped hydroxyapatite coating on titanium alloy. *Int. J. Appl. Ceram. Technol.* **2016**, *13*, 1059–1068. [CrossRef]
56. Aksakal, B.; Say, Y.; Buyukpinar, Ç.; Bakirdere, S. Biodegradation of hydroxyapatite coated Rex-734 alloy with silver and selenium/chitosan substitutions: In vitro analysis. *Ceram. Int.* **2017**, *43*, 12609–12615. [CrossRef]

57. Pajchel, L.; Kolodziejski, W. Solid-state MAS NMR, TEM, and TGA studies of structural hydroxyl groups and water in nanocrystalline apatites prepared by dry milling. *J. Nanopart. Res.* **2013**, *15*, 1868. [CrossRef] [PubMed]
58. Kolmas, J.; Groszyk, E.; Piotrowska, U. Nanocrystalline hydroxyapatite enriched in selenite and manganese ions: Physicochemical and antibacterial properties. *Nanoscale Res. Lett.* **2015**, *10*, 278. [CrossRef] [PubMed]
59. Murugan, N.; Kavitha, L.; Shinyjoy, E.; Rajeswari, D.; Vimala, K.; Kannan, S.; Gopi, D. Smart rose flower like bioceramic/metal oxide dual layer coating with enhanced anti-bacterial, anti-cancer, anti-corrosive and biocompatible properties for improved orthopedic applications. *RSC Adv.* **2015**, *5*, 85831–85844. [CrossRef]
60. Kramer, G.F.; Ames, B.N. Mechanims of mutagenicity and toxicity of sodium selenite (Na_2SeO_3) in *Salmonella typhimurium*. *Mutat. Res. Fundam. Mol. Mech. Mutagen.* **1988**, *201*, 169–180. [CrossRef]
61. Seko, Y.; Imura, N. Active oxygen generation as a possible mechanism of selenium toxicity. *Biomed. Environ. Sci.* **1997**, *10*, 333–339. [PubMed]
62. Vekariya, K.K.; Kaur, J.; Tikoo, K. Alleviating anastrozole induced bone toxicity by selenium nanoparticles in SD rats. *Toxicol. Appl. Pharmacol.* **2013**, *268*, 212–220. [CrossRef] [PubMed]
63. Taskin, E.; Dursun, N. The protection of selenium on adriamycin-induced mitochondrial damage in rat. *Biol. Trace Elem. Res.* **2012**, *147*, 165–171. [CrossRef] [PubMed]
64. Qi, H.P.; Wei, S.Q.; Gao, X.C.; Yu, N.N.; Hu, W.Z.; Bi, S.; Cui, H. Ursodeoxycholic acid prevents selenite-induced oxidative stress and alleviates cataract formation: In vitro and in vivo studies. *Mol. Vis.* **2012**, *18*, 151–160. [PubMed]
65. Rooban, B.N.; Sasikala, V.; Gayathri Devi, V.; Sahasranamam, V.; Abraham, A. Prevention of selenite induced oxidative stress and cataractogenesis by luteolin isolated from *Vitex negundo*. *Chem. Biol. Interact.* **2012**, *196*, 30–38. [CrossRef] [PubMed]
66. Rajamannan, N.M. Oxidative-mechanical stress signals stem cell niche mediated LRP5 osteogenesis in eNOS(−/−) null mice. *J. Cell. Biochem.* **2012**, *113*, 1623–1634. [CrossRef] [PubMed]
67. Zhang, W.; Wang, X.; Wang, S.; Zhao, J.; Xu, L.; Zhu, C.; Zeng, D.; Chen, J.; Zhang, Z.; Kaplan, D.L.; et al. The use of injectable sonication-induced silk hydrogel for VEGF165 and BMP-2 delivery for elevation of the maxillary sinus floor. *Biomaterials* **2011**, *32*, 9415–9424. [CrossRef] [PubMed]
68. Andreas, S.S.; Parag, K.J.; Wasim, S.K. Clinical applications of mesenchymal stem cells in the treatment of fracture non-union and bone defects. *Curr. Stem Cell Res. Ther.* **2012**, *7*, 127–133.
69. Bauer, T.W.; Togawa, D. Bone graft substitutes: Towards a more perfect union. *Orthopedics* **2003**, *26*, 925–926. [CrossRef] [PubMed]
70. Zhang, W.; Xu, X.; Chai, Y.; Wang, Y. Synthesis and characterization of Zn^{2+} and SeO_3^{2-} co-substituted nano-hydroxyapatite. *Adv. Powder Technol.* **2016**, *27*, 1857–1861. [CrossRef]
71. Alshemary, A.Z.; Engin Pazarceviren, A.; Tezcaner, A.; Evis, Z. Fe^{3+}/SeO_4^{2-} dual doped nano hydroxyapatite: A novel material for biomedical applications. *J. Biomed. Mater. Res. B Appl. Biomater.* **2018**, *106*, 340–352. [CrossRef] [PubMed]

crystals

MDPI

Review

Transition Metal Selenite Halides: A Fascinating Family of Magnetic Compounds

Peter S. Berdonosov *, Elena S. Kuznetsova and Valery A. Dolgikh

Department of Chemistry of Lomonosov Moscow State University, Moscow 119991, Russia; e.kuznetsova@inorg.chem.msu.ru (E.S.K.); dolgikh@inorg.chem.msu.ru (V.A.D.)
* Correspondence: berdonosov@inorg.chem.msu.ru; Tel.: +7-495-939-3504

Received: 12 March 2018; Accepted: 2 April 2018; Published: 4 April 2018

Abstract: The problem of searching for low-dimensional magnetic systems has been a topical subject and has attracted attention of the chemistry and physics community for the last decade. In low-dimensional magnetic systems, magnetic ions are distributed anisotopically and form different groups such as dimers, chains, ladders, or planes. In 3D frameworks, the distances between magnetic ions are equal in all directions while in low-dimensional systems the distances within groups are different from those between groups. The main approach of searching for desired systems is a priori crystal chemical design expecting the needed distribution of transition metal ions in the resulting structure. One of the main concepts of this structural design is the incorporation of the *p*-element ions with stereochemically active electron pairs and ions acting as spacers in the composition. Transition metal selenite halides, substances that combine SeO_3^{2-} groups and halide ions in the structure, seem to be a promising object of investigation. Up to now, there are 33 compounds that are structurally described, magnetically characterized, and empirically tested on different levels. The presented review will summarize structural peculiarities and observed magnetic properties of the known transition metal selenite halides. In addition, the known compounds will be analyzed as possible low-dimensional magnetic systems.

Keywords: selenite; selenite halide; crystal structure; transition metal; magnetic structure

1. Introduction

In recent decades, approaches for the search for and synthesis of low-dimensional magnets, that is, the systems with magnetic ions distributed anisotropically in the crystal structure and forming different types of groups as dimers, trimers, tetramers or isolated plaquette units, chains of ions, ladders, or planes, have been attracting considerable interest from the physics and chemistry research communities. Such geometric distribution of magnetic ions may lead to exotic magnetic states such as spin liquids or geometric magnetic spin frustrations which are hot topics in the physics of condensed matter [1,2]. In the usual three-dimensional structures, the magnetic exchange between magnetic ions is equal in all directions whereas in low-dimensional systems the exchange within the above-mentioned groups is much stronger than between the groups.

The interest in low-dimensional magnetic systems has resulted, on the one hand, from their fundamental importance as model objects for the verification of theoretical predictions in condensed matter physics theory and on the other hand, from their possible applications, for example, for tunable heat conduction discussed in [3]. Until now, the compounds studied from this point of view in inorganic chemistry are usually limited to oxide systems, chalcogenide compounds, and sometimes halides [2]. Currently, one of the main avenues for the search for low-dimensional magnetic compounds is the targeted synthesis of new compounds using the a priori structure design suggesting a special distribution of magnetic transition metal ions in the final crystal structure. It should be kept in mind

that a structural sublattice of ions could be different from the real magnetic exchange path but the probability to find a low-dimensional magnetic sublattice in a low-dimensional crystal structure should be higher. The structural influence of stereochemically active electron pairs of *p*-elements in the middle oxidation states, such as Bi(III), Pb(II), Te(IV), Se(IV) etc. appears to be an unattractive synthesis concept in the search for low-dimensional magnetic systems. A lone electron pair is non-bonding and plays a role of the additional ligand for the central ion. According to the Valence Shell Electron Pair Repulsion theory [4,5] such ions in the oxidation state +4 should have a stereochemically active electron pair which distorts the selenium environment. As a result, one side of the ion is not bonded to other atoms in the crystal structure and electron pairs form cavities or holes in the crystal structure. According to [6], the volume of the non-bonding pair of electrons is compatible to that of the O^{2-} ion. Sometimes [7] ions with electron pairs are referred to as 'chemical scissors' which are "cutting through" the 3D crystal structure. The resulting structure cavity may be extended even to a layer by introducing the additional terminating ions (spacers), for example, halide ions.

By now, many transition metal selenite halides have been synthesized and characterized. The majority of these compounds contain copper in the oxidation state +2. Some compounds in the mentioned group have been characterized magnetically by different techniques. In accordance with the above-mentioned concept, it appears useful to summarize the information about the known compounds including their crystal structures and magnetic characterization, which will be the subject of the present review.

Usually the selenite group SeO_3^{2-} possesses a pyramidal shape (C_{3v} symmetry in the free state) with distances Se–O are about 1.73 Å and O–Se–O angles are 103° [8]. In addition, the SeO_3^{2-} group may be described as a pseudo-tetrahedral anion with the lone electron pair acting as an invisible ligand in the crystal structures. The observation of lone electron pairs in selenites is one of their structural peculiarities. In the solid state, the C_{3v} symmetry of SeO_3^{2-} groups is distorted due to the differences in the connectivity. In contrast to sulfur, the +4 oxidation state is more stable for selenium due to the small value of redox potential SeO_4^{2-}/SeO_3^{2-} 0.05 V which is positive in alkaline solutions whereas the corresponding value for SO_4^{2-}/SO_3^{2-} is much lower −0.93 V. This makes selenites more stable in solutions compared to sulfites [8,9]. Tellurium has a larger radius and may form not only TeO_3^{2-} tellurite groups but display higher coordination numbers, 3 + 1 for example. Moreover, tellurites often tend to form polyions with different compositions and geometry [7,10].

Combining the transition ions, selenite, or tellurite groups with halide ions within one structure may lead to the novel crystal structures and different magnetic properties [11–15]. It is easy to note that up to now transition metal tellurite halide compounds are more explored. There are two factors which account for this. First one is the oxidizing activity of selenites. In water solution, the reduction potential SeO_3^{2-}/Se is −0.336 V [9]. For this reason, it will be difficult to combine Ti^{3+}, V^{3+} ions with selenites, while tellurites tend to be more stable. Another reason for tellurites being more studied is the stability of tellurium dioxide in the air and consequently its facile synthetic preparation. Selenium dioxide is air- and moisture-sensitive, hence all preparative procedures with it are usually performed under dry conditions (i.e., argon or nitrogen filled glove boxes), in order to avoid the formation of hydrates or hydroselenites. As it will be shown below, chlorides are the most representative group among halides, whereas iodides were obtained in one case only. The reason for this seems to be lying in the oxidizing effect of the selenite groups.

Usually, transition metal ions are responsible for the magnetic behavior of substances. From this point of view, 3d metals in middle oxidation states are most attractive as 4d and 5d metals in low oxidation states may bind together and the magnetic moment of metal ions disappears [16]. The literature search shows that up to now there are no data about crystal structures and magnetic properties of 4d and 5d transition metal selenite halides (taking into account that compound $Pb_2NbO_2(SeO_3)_2Cl$ [17] contains Nb in the oxidation state +5 and d^0 configuration). Therefore, in this review we will describe crystal structures and some reported magnetic properties of 3d metal selenite halides, that is, compounds containing both SeO_3^{2-} groups and halide ions.

2. Crystal Structures and Magnetic Properties Overview

Here we will describe the crystal structures of complex transition metal selenite halides with known magnetic properties. The term "halide ions" will refer to chlorides, bromides, and sometimes iodides. Fluoride compounds usually show different behavior and tendencies due to the peculiarities of fluorine and fluorides sometimes are closer to pure oxide compounds. Moreover, the literature data about selenite fluorides or oxofluorides of d-metals are rather limited and describe only a small number of compounds [18–21].

Below, we will pay special attention to the transition metal M–M ions distances in the structures. It should be noted, that this is an oversimplified way of considering the spin interactions. For a precise estimation, the geometry of d-orbitals and their interactions with the orbitals of bridged atoms should be examined. Nevertheless, it seems that presented simple model may be used at least for crystal chemical design of 3d-metal selenite halide compounds, as in the case of very long M–M distances the probability of spin interactions exchange should be lower.

2.1. Composition $M^{II}{}_5(SeO_3)_4X_2$

The group of compounds under consideration contains 6 different compositions and exists up to now only for Fe, Co, Ni, and Cu. Compositions and some crystallographic information are given in Table 1. As can be seen from Table 1, the crystal structures for these compounds are different in compositions and cell symmetries.

The substances may be divided into several groups according to their common composition and structural relations.

The first group of transition metal selenite halides may be described by the composition $M^{II}{}_5(SeO_3)_4X_2$ (substances 1–5 in Table 1) [22–25]. While cobalt and nickel compounds are similar in some forms, copper compounds' crystal structures are different. The crystal structure of $Cu_5(SeO_3)_4Cl_2$ is presented in Figure 1 as the projection on *ab* plane.

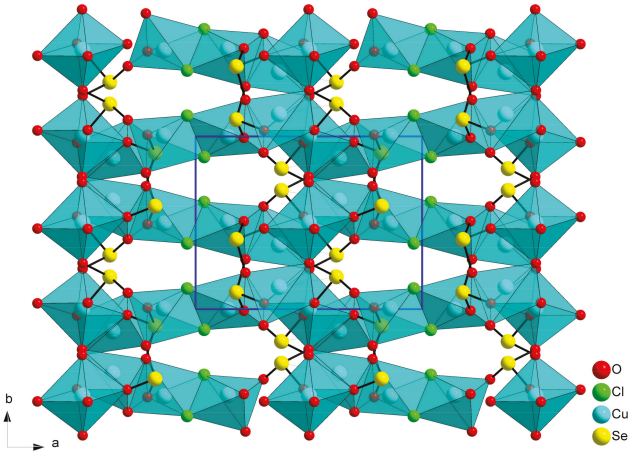

Figure 1. Projection of the $Cu_5(SeO_3)_4Cl_2$ crystal structure on ab plane according to [22]. Copper polyhedra are shown.

The crystal structure of $Cu_5(SeO_3)_4Cl_2$ [20] may be presented as a three-dimensional framework of corner- and edge-shared polyhedra [CuO_5], [CuO_6], and [CuO_3Cl_2]. It is easy to see in Figure 1 that the framework of Cu polyhedra contains wide holes where selenium atoms are located. Due to the pyramidal shape and the presence of the E-pairs in SeO_3^{2-} groups copper polyhedra do not polymerize in more dense packing. According to the structural data, Cu–Cu distances in the crystal

structure of $Cu_5(SeO_3)_4Cl_2$ are in the range of 3.15–3.30 Å and one distance value is about 3.6 Å. One may conclude that spin–spin interactions between Cu^{2+} ions may be observed in this compound.

Field-cooled magnetization measurements data show spontaneous polarization below the critical temperature of $T_C \approx 45$ K. Below this point almost linear magnetization increase and saturation at low temperatures are observed. The heat capacity temperature dependence demonstrates a λ-type anomaly at 44.1(2) K thus confirming magnetization measurements results. The Curie–Weiss temperature calculated from the approximation of experimental data has a value of −151(4) K and indicates predominantly antiferromagnetic spin-exchange interactions. Thus, a long-range antiferromagnetic order occurs in $Cu_5(SeO_3)_4Cl_2$ at 44.1(2) K.

However, field dependent magnetization measurements at 1.87 K reveal a hysteresis loop, indicating the presence of weak ferromagnetic interactions. This is a common phenomenon occurred in complex magnetic systems based on Cu^{2+} ions where low-dimensional magnetic interactions take place. The complexity of exchange paths is due to the numerous distortions of coordination polyhedra in the crystal structure. Analysis of interconnections between copper, chlorine, and oxygen atoms in the $Cu_5(SeO_3)_4Cl_2$ structure revealed two main types of magnetic exchange paths: the first one is the antiferromagnetic path between copper atoms connected via the oxygen atom; the Cu–O–Cu angle value exceeds 90°. The second path is the ferromagnetic path between copper atoms interacting via a chlorine atom. The Cu–Cl–Cu angle is almost 90°—such bonding angles typically support ferromagnetic spin-exchange interactions [22].

Due to the Jahn–Teller effect, the surrounding of Cu^{2+} differs from that of Co^{2+} and Ni^{2+}, and this is the reason for differences between cobalt and nickel compounds and the copper ones. Similar compounds for cobalt and nickel have common structures at least in one form (Table 1, substances 2, 3 and 5 [23,25]). All three metal atoms in the compounds under discussion have a distorted octahedral coordination (Figure 2a). Two atoms have a $[MO_5X]$ (X = Cl and Br) coordination and one M atom has a $[MO_4X_2]$ coordination with the oxygen atoms in the square plane. The O–O edge-sharing $[MO_5X]$ polyhedra form chains which are connected via common halogen vertexes into layers in the crystal structures of cobalt and nickel compounds. A three-dimensional structure appears when such layers are bridged by $[MO_4X_2]$ polyhedrons and SeO_3^{2-} groups (Figure 2a). The crystal structures of $Co_5(SeO_3)_4X_2$ and $Ni_5(SeO_3)_4Br_2$ have M–M distances in the range of 3.10–3.37 Å for $Co_5(SeO_3)_4Cl_2$ [23], 3.07–3.40 Å for $Co_5(SeO_3)_4Br_2$ [23], and 3.03–3.39 Å for $Ni_5(SeO_3)_4Br_2$ [25].

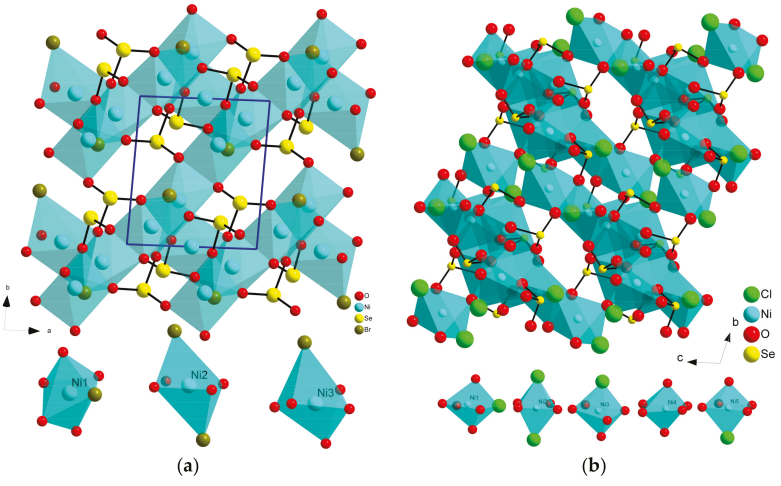

Figure 2. The $Ni_5(SeO_3)_4Br_2$ framework crystal structure (**a**) and $Ni_5(SeO_3)_4Cl_2$ structure (**b**). Coordination surroundings of the Ni atoms are depicted at the bottom part of the pictures.

Table 1. Compositions and crystallographic data for transition metals selenite halides with described magnetic properties.

#	Composition	Space Group	Z	Cell Constants				Ref.
				a, Å	b, Å	c, Å	Angles, °	
1	$Cu_5(SeO_3)_4Cl_2$	$P2_1/c$	2	10.9104(8)	8.3134(6)	7.5490(6)	β = 90.715(6)	[22]
2	$Co_5(SeO_3)_4Cl_2$	P-1	1	6.4935(8)	7.7288(8)	7.7443(10)	α = 66.051(11) β = 73.610(11) γ = 81.268(9)	[23]
3	$Co_5(SeO_3)_4Br_2$	P-1	1	6.4897(9)	7.7574(10)	7.7552(10)	α = 66.850(13) β = 73.960(12) γ = 81.350(11)	[23]
4	$Ni_5(SeO_3)_4Cl_2$	P-1	2	8.076(2)	9.288(2)	9.376(2)	α = 101.97(3) β = 105.60(3) γ = 91.83(3)	[24]
5	$Ni_5(SeO_3)_4Br_2$	P-1	1	6.430(3)	7.632(3)	7.658(3)	α = 68.017(16) β = 74.181(16) γ = 81.465(19)	[25]
6	$Sr_2Co(SeO_3)_2Cl_2$	$P2_1/n$	2	5.3400(10)	6.4279(6)	12.3220(10)	β = 92.440(10)	[26]
7	$Sr_2Ni(SeO_3)_2Cl_2$	$P2_1/n$	2	5.3254(11)	6.4363(13)	12.197(2)	β = 92.53(3)	[26]
8	$Sr_2Cu(SeO_3)_2Cl_2$	$P2_1/n$	2	5.22996(3)	6.50528(4)	12.34518(7)	β = 91.3643(2)	[27]
9	$CaCu_2(SeO_3)_2Cl_2$	$C2/c$	4	12.759(3)	9.0450(18)	6.9770(14)	β = 91.03(3)	[28]
10	$SrCu_2(SeO_3)_2Cl_2$	$P2_1$	2	7.1630(14)	7.2070(14)	8.0430(16)	β = 95.92(3)	[27]
11	$PbCu_2(SeO_3)_2Cl_2$	$C2/c$	4	13.056(1)	9.5567(9)	6.9006(6)	β = 90.529(7)	[29]
12	$Bi_2Fe(SeO_3)_2OCl_3$	$P2_1/m$	2	8.570(2)	7.137(2)	8.604(2)	β = 107.090(3)	[30]
13	$Cu_3Bi(SeO_3)_2O_2Cl$	Pmmn	2	6.3540(4)	9.6350(5)	7.2330(4)		[31]
14	$Cu_3Bi(SeO_3)_2O_2Br$	Pmmn	2	6.3900(3)	9.6940(4)	7.2870(3)		[31]
15	$Cu_3Bi(SeO_3)_2O_2I$	Pmmn	2	6.4360(2)	9.7510(4)	7.3770(3)		[31]
16	$Cu_3Y(SeO_3)_2O_2Cl$	Pmmn	2	6.2991(1)	9.4411(1)	6.9724(1)		[32]
17	$Cu_3La(SeO_3)_2O_2Cl$	Pmmn	2	6.39407(18)	9.7310(3)	7.1547(2)		[33]
18	$Cu_3Nd(SeO_3)_2O_2Cl$	Pmmn	2	6.37775(10)	9.62685(16)	7.09341(11)		[31]
19	$Cu_3Sm(SeO_3)_2O_2Cl$	Pmmn	2	6.34616(4)	9.56090(7)	7.04377(5)		[34]
20	$Cu_3Eu(SeO_3)_2O_2Cl$	Pmmn	2	6.3384 (1)	9.5341(2)	7.0273(1)		[35]
21	$Cu_3Gd(SeO_3)_2O_2Cl$	Pmmn	2	6.3220(6)	9.501(1)	7.0202(8		[36]
22	$Cu_3Dy(SeO_3)_2O_2Cl$	Pmmn	2	6.313(1)	9.465(2)	6.987(2)		[36]
23	$Cu_3Ho(SeO_3)_2O_2Cl$	Pmmn	2	6.2999(6)	9.440(1)	6.9723(8)		[36]
24	$Cu_3Er(SeO_3)_2O_2Cl$	Pmmn	2	6.299(1)	9.432(3)	6.967(2)		[36]
25	$Cu_3Yb(SeO_3)_2O_2Cl$	Pmmn	2	6.28278(3)	9.39486(5)	6.93291(3)		[37]
26	$Cu_3Lu(SeO_3)_2O_2Cl$	Pmmn	2	6.2681(1)	9.3756(2)	6.9326(1)		[35]
27	$Cu_3La(SeO_3)_2O_2Br$	Pmmn	2	6.40071(5)	9.75675(7)	7.17800(5)		[33]
28	$Cu_3Nd(SeO_3)_2O_2Br$	Pmmn	2	6.382(2)	9.698(3)	7.091(2)		[36]
29	$Cu_3Sm(SeO_3)_2O_2Br$	Pmmn	2	6.348(1)	9.581(2)	7.079(2)		[36]
30	$Cu_3Gd(SeO_3)_2O_2Br$	Pmmn	2	6.337(1)	9.5515(8)	7.0540(9)		[36]
31	$NaCu_5(SeO_3)_2O_2Cl_3$	Pnma	4	17.769(7)	6.448(3)	10.522(4)		[38]
32	$KCu_5(SeO_3)_2O_2Cl_3$	Pnma	4	18.1691(6)	6.4483(2)	10.5684(4)		[39]
33	$Na_2Cu_7(SeO_3)_4O_2Cl_4$	P-1	1	7.446(2)	8.349(3)	9.137(3)	α = 110.335(7) β = 106.166(3) γ = 105.161(7)	[40]

In spite of the similarity of $Co_5(SeO_3)_4X_2$ (X = Cl and Br) compounds, the nickel chloride is not isostructural with the bromide one [24,41]. The unit cell for $Ni_5(SeO_3)_4Cl_2$ is about twice as

big in volume compared to that of the bromide. There are five Ni atoms in the structure which are octahedrally coordinated by oxygen atoms from SeO_3^{2-} groups or Cl^- ions. There are three types of $[NiO_5Cl]$ and one type of $[NiO_4Cl_2]$ octahedrons and a pure oxygen octahedron $[NiO_6]$ in the structure of $Ni_5(SeO_3)_4Cl_2$ (Figure 2b). Thus, the structure of $Ni_5(SeO_3)_4Cl_2$ features a condensed three-dimensional (3D) network built by Ni^{2+} ions interconnected by SeO_3^{2-} anions as well as Cl^- anions. The crystal structure of $Ni_5(SeO_3)_4Cl_2$ is presented in Figure 2b. It is interesting to mention that Ni–Ni distances in nickel selenite chloride vary from 2.94 up to 3.9 Å [41]. The existence of isostructural compounds for Co with Cl and Br may indicate that $Ni_5(SeO_3)_4Cl_2$ might form two polymorphs. It should be noted that tellurites of the similar composition $Ni_5(TeO_3)_4X_2$ (X = Cl, Br) [12] are isostructural to each other as well as to related cobalt compounds $Co_5(TeO_3)_4X_2$ (X = Cl, Br) [42], but differ from presented selenites. Magnetic properties were studied for $Ni_5(SeO_3)_4Cl_2$ as well as for isostructural compounds $Co_5(SeO_3)_4X_2$ (X = Cl and Br) and $Ni_5(SeO_3)_4Br_2$.

$Ni_5(SeO_3)_4Cl_2$ demonstrates antiferromagnetic properties, according to magnetic susceptibility measurements data. Long-range order takes place at approximately 4.5 K. Curie–Weiss temperature $\theta = -143(2)$ K indicates strong antiferromagnetic interactions between nickel atoms. Such strong interactions take place because of the very short Ni–Ni distances. Moreover, the crystal structure of $Ni_5(SeO_3)_4Cl_2$ is three-dimensional and the network is highly condensed. According to the magnetic measurements data there is no evidence of extraordinary or unusual magnetic behavior in this compound [22], but up to now no detailed study has been undertaken, therefore this problem is still of a certain interest.

Concerning $Co_5(SeO_3)_4X_2$ (X = Cl and Br) and $Ni_5(SeO_3)_4Br_2$, there are also antiferromagnetic transitions in the magnetic subsystems of these compounds (T_N = 18 K, 20 K and 46 K for $Co_5(SeO_3)_4Cl_2$, $Co_5(SeO_3)_4Br_2$, and $Ni_5(SeO_3)_4Br_2$, respectively) [23,25]. However, unlike $Ni_5(SeO_3)_4Cl_2$, magnetic measurements were performed using single crystal samples, and this allowed to carry out a more detailed investigation. In particular, the magnetic susceptibility measurements in oriented crystals revealed anisotropy—typical for the zero-field splitting—induced by the single-ion anisotropy of 3d-metal ions. This allowed defining ground states and electron transitions in these compounds at lower temperatures. Another peculiarity is that the magnetic ordering permeates only one subsystem in the complex magnetic system: a minority fraction is represented in $Co_5(SeO_3)_4X_2$ (X = Cl and Br) ordered subsystem while a magnetically ordered fraction dominates in $Ni_5(SeO_3)_4Br_2$.

2.2. Compositions $Sr_2M^{II}(SeO_3)_2Cl_2$ and $MM''_2(SeO_3)_2Cl_2$

The group of selenites with the composition $Sr_2M^{II}(SeO_3)_2Cl_2$ is presented by isostructural compounds for M^{II} = Co, Ni, and Cu [26,27] (compounds 6–8 in Table 1). The unit cell of these compounds contains one independent atom of Sr and one atom of M. The nearest coordination surrounding of Sr and M atoms comprise oxygen and chlorine atoms, whereas Se atoms have only oxygen atoms as neighbors. In all three compounds, strontium atoms are situated in distorted $[SrO_6Cl_3]$ 9-vertex polyhedra which form layers perpendicular to the [0 0 1] direction of the structure. D-metal ions are allocated in Jahn–Teller distorted octahedrons $[MO_4Cl_2]$. These polyhedra share common edges with layers of Sr polyhedra and form a 3D structure shown in Figure 3. The M–M distances in the represented structures are longer than 5 Å.

The substitution of one more strontium ion by a d-element ion for compounds $Sr_2M^{II}(SeO_3)_2Cl_2$ is possible for Cu^{2+} and produces $SrCu_2(SeO_3)_2Cl_2$ [27]. This compound is similar to the tellurites $SrCu_2(TeO_3)_2Cl_2$ [43] and $BaCu_2(TeO_3)_2Cl_2$ [44]. These compounds crystallize in the non-centrosymmetrical space group $P2_1$. The crystal structure of $SrCu_2(SeO_3)_2Cl_2$ is given in Figure 4. The asymmetric unit of $SrCu_2(SeO_3)_2Cl_2$ contains one Sr atom and two copper atoms. Sr atom is allocated in the $[SrO_6Cl_2]$ polyhedron and copper atoms are situated in distorted square pyramids $[CuO_4Cl]$ and $[CuO_3Cl_2]$. It seems that Jahn–Teller distortion in the compound under discussion is much stronger than for a copper atom surrounding in the case of $Sr_2Cu(SeO_3)_2Cl_2$ [27]. Such a strong distortion is impossible for cobalt and nickel and may explain why the same structures are not formed

for them. Both Se atoms in the structure are connected to the strontium or copper polyherda and play the role of an additional linker to form a framework. Copper polyhedra are connected by the common O–Cl edges and form dimers [$Cu_2O_4Cl_2$] (Figure 4). The distance of Cu–Cu in the dimer groups is 3.29 Å which is shorter than 3.35 Å in $SrCu_2(TeO_3)_2Cl_2$ [43].

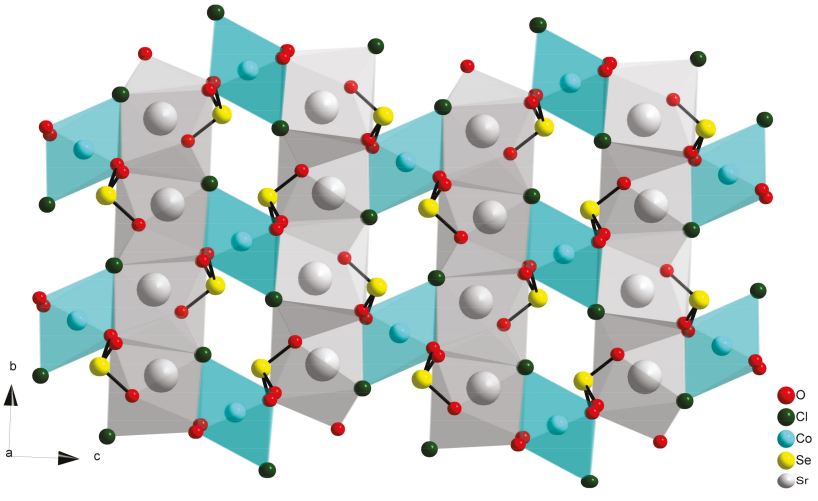

Figure 3. Layers of [SrO_6Cl_3] polyhedral connected by [MO_4Cl_2] octahedra and SeO_3^{2-} groups in the crystal structure of $Sr_2Co(SeO_3)_2Cl_2$ [26].

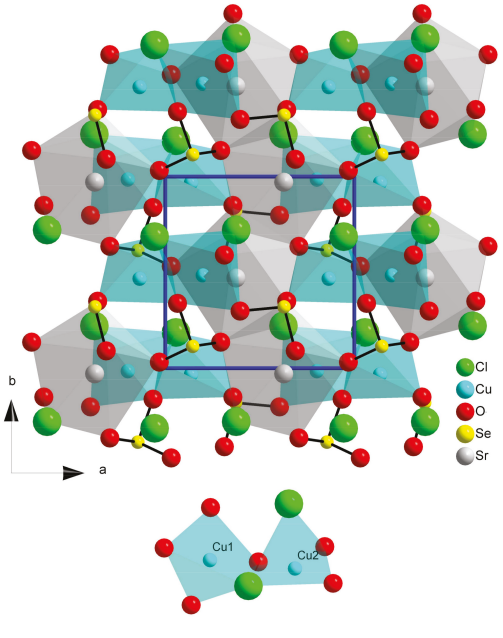

Figure 4. Crystal structure of $SrCu_2(SeO_3)_2Cl_2$ [27]. The [$Cu_2O_4Cl_2$] dimer is shown separately at the bottom part of the figure.

According to Shannon's data [45] the ionic radius of Sr^{2+} ions is close to that of Pb^{2+}. At the same time, according to the Periodic Table of the elements, calcium as an alkali earth metal may be a smaller analog of strontium. There were obtained compounds with compositions $CaCu_2(SeO_3)_2Cl_2$ and $PbCu_2(SeO_3)_2Cl_2$ [28,29] (Table 1 substances 9 and 11). It is apparent (Table 1) that both compounds are isostructural but have a different unit cell in comparison with $SrCu_2(SeO_3)_2Cl_2$ (Table 1 substance 10). At the same time, the tellurite compound $PbCu_2(TeO_3)_2Cl_2$ [29] is isostructural to $SrCu_2(SeO_3)_2Cl_2$ [27]. This phenomenon may be associated with differences in ionic radii of Se^{4+} and Te^{4+}. A bigger tellurium atom is more compatible with strontium or lead, whereas the smaller selenium atom is the reason for the formation of the related calcium and lead compounds.

The differences in the crystal structures of these two types of compounds are shown in Figure 5, using $PbCu_2(YO_3)_2Cl$ (Y = Se, Te) as an example. The crystal structures of $CaCu_2(SeO_3)_2Cl_2$ and $PbCu_2(SeO_3)_2Cl_2$ contain two different copper atoms in a strongly squeezed tetrahedral [CuO_4] and octahedral [CuO_4Cl_2] environments. In the case of octahedrally coordinated copper atoms, two oxygen atoms are situated at distances about 2.6 Å and [CuO_2Cl_2] may be considered as a magnetic plaquette. Calcium or lead atoms are situated in the 8-vertex polyhedrons [MO_4Cl_4]. Selenium atoms share common O vertexes of copper and calcium or lead polyhedra and are situated next to the holes of the framework formed by them. From data presented in [28,29] it may be seen that Cu–Cu distances are relatively long. In case of the Ca compound the distances are 3.85–4.12 Å, and for the Pb compound the distances are 3.93–4.06 Å.

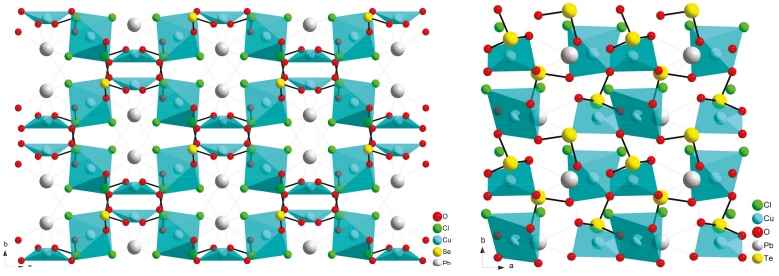

(**a**) (**b**)

Figure 5. Copper polyhedra in the crystal structures of $PbCu_2(SeO_3)_2Cl$ (**a**) and $PbCu_2(TeO_3)_2Cl$ (**b**).

Within this wide variety of compositions, magnetic properties are known only for $CaCu_2(SeO_3)_2Cl_2$ [28], $PbCu_2(SeO_3)_2Cl_2$ [29], $SrCu_2(SeO_3)_2Cl_2$, and $Sr_2Cu(SeO_3)_2Cl_2$ [46]. Results of magnetic susceptibility measurements in the wide temperature range for $CaCu_2(SeO_3)_2Cl_2$ indicate the low-dimensional character of magnetic behavior with predominant antiferromagnetic interactions for this compound (Figure 6). Antiferromagnetic ordering takes place at approximately 6 K. The $\chi(T)$ curve approximation resulted in a uniform spin-1/2 chain model for the magnetic structure. A strong intrachain exchange coupling of ~133 K and frustrated interchain couplings realized via the two non-equivalent superexchange paths take place in the magnetic structure (Figure 7). It is worth mentioning that structural and magnetic chains are not the same in $CaCu_2(SeO_3)_2Cl_2$: due to the peculiar crystal structure, the spin chains run in the direction almost perpendicular to that of the structural chains (Figure 8).

$PbCu_2(SeO_3)_2Cl_2$ is isostructural to $CaCu_2(SeO_3)_2Cl_2$ and its magnetic behavior is somewhat similar to that of the calcium compound (Figure 9). It can be approximated by a uniform spin-1/2 chain model with interchain interactions. As in the calcium compound, magnetic chains do not coincide with the structural ones (Figure 10). However, the interchain couplings in $PbCu_2(SeO_3)_2Cl_2$ and $CaCu_2(SeO_3)_2Cl_2$ are rather different: the larger value of the interchain exchange integral in $PbCu_2(SeO_3)_2Cl_2$ results in an increase of Neel temperature (13 K in $PbCu_2(SeO_3)_2Cl_2$ versus 6 K in $CaCu_2(SeO_3)_2Cl_2$).

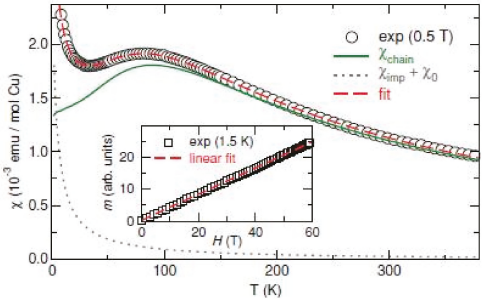

Figure 6. Magnetic susceptibility measured for $CaCu_2(SeO_3)_2Cl_2$ (circles) and the uniform spin-1/2 chain model fit (dashed line). Heisenberg chain (solid line) and impurity (dotted line) contributions to the fitted curve are shown. The inset shows the high-field magnetization curve (squares) with a linear fit (dashed line) Reprinted figure with permission from [28] Copyright (2011) by the American Physical Society.

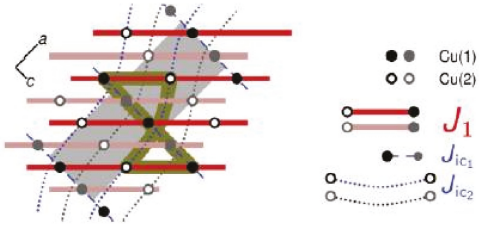

Figure 7. Spin model for $CaCu_2(SeO_3)_2Cl_2$. Filled and empty circles show the Cu(1) and Cu(2) positions, respectively. Bold lines and circles denote atoms in the front plane, whereas gray circles and shaded lines correspond to the atoms lying in the back plane. The planes are connected by Jic1 couplings only. A closed loop (bold line) having an odd number of AFM couplings indicates that the spin model is frustrated. The unit cell is depicted by the gray rectangle. Reprinted figure with permission from [28] Copyright (2011) by the American Physical Society.

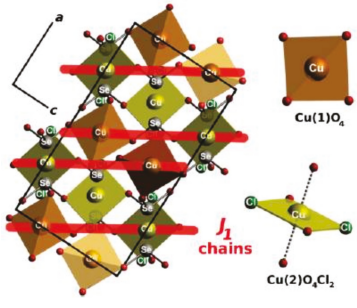

Figure 8. (left) Crystal structure of $CaCu_2(SeO_3)_2Cl_2$. The structural chains run along [10^-1] (not shown), whereas the magnetic chains range along ∼[201], as shown by bold (red) lines. Small unlabeled spheres denote O atoms. (right) Local environment of Cu(1) and Cu(2). The magnetically active $Cu(1)O_4$ and $Cu(2)O_2Cl_2$ plaquettes are highlighted. Reprinted figure with permission from [28] Copyright (2011) by the American Physical Society.

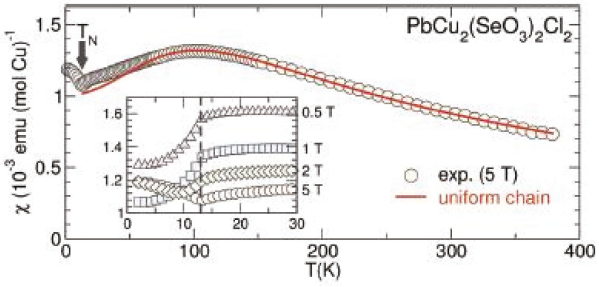

Figure 9. Magnetic susceptibility of $PbCu_2(SeO_3)_2Cl_2$ (circles) and the fit (solid line) using a uniform Heisenberg chain model with J_1 = 160 K, g = 1.97, and the temperature independent contribution $\chi_0 = 2 \times 10^{-5}$ emu (mol Cu)$^{-1}$. The kink at 13 K indicates long-range magnetic ordering. Inset: field dependence of χ(T). The strong dependence of χ on the magnetic field above T_N is an extrinsic effect (ferromagnetic impurity). Reproduced from Ref. [29] with permission from the Royal Society of Chemistry.

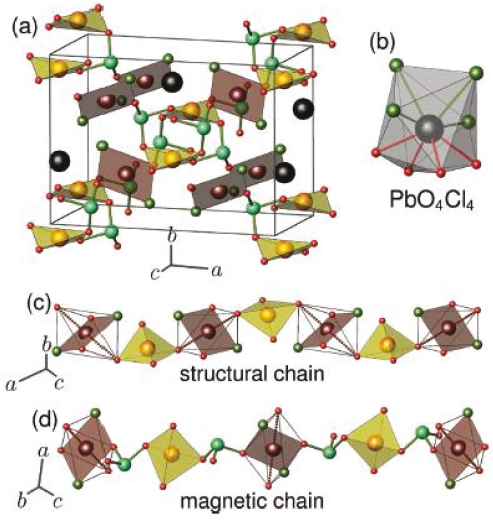

Figure 10. Crystal structure of $PbCu_2(SeO_3)_2Cl_2$. (**a**) The unit cell. Magnetic $Cu(1)O_4$ and $Cu(2)O_2Cl_2$ plaquettes are shown as light and dark filled polyhedra. Se–O bonds and Pb atoms are denoted by lines and large black spheres, respectively. (**b**) The coordination polyhedron of Pb. (**c**) Structural chains, formed by cornersharing $Cu(1)O_4$ distorted plaquettes and $Cu(2)O_4Cl_2$ octahedra (empty octahedra, with filled $Cu(2)O_2Cl_2$ plaquettes; long Cu(2)-O contacts are shown with thick dashed lines). (**d**) Magnetic chains. The nearest-neighbor superexchange J_1 runs via Cu(1)–O$\cdots$O–Cu(2) paths, along the edge of a SeO_3 pyramid (Se–O bonds are shown with lines). Reproduced from Ref. [29] with permission from the Royal Society of Chemistry.

Though $Sr_2Cu(SeO_3)_2Cl_2$ has a different structure from MM"$(SeO_3)_2Cl_2$ compounds, its magnetic behavior can also be described in terms of the Heisenberg uniform spin chain with strong interchain interactions (J $\approx$ 104–106 K). Unlike $CaCu_2(SeO_3)_2Cl_2$ and $PbCu_2(SeO_3)_2Cl_2$, in $Sr_2Cu(SeO_3)_2Cl_2$ there is presumably no long-range order observed down to at least 2 K, and magnetic exchange paths lie through the structural chains built of copper polyhedra and SeO_3^{2-} groups [46]. Further

investigation is needed to establish the microscopic magnetic model and to define exchange paths in the magnetic subsystem.

A different case is with $SrCu_2(SeO_3)_2Cl_2$. Here, the most appropriate model is the one of slightly interacting dimers. This is due to the structural features including CuO_4 corner-shared plaquettes. In general, according to preliminary measurements data the magnetic behavior of $SrCu_2(SeO_3)_2Cl_2$ is similar to that of $SrCu_2(TeO_3)_2Cl_2$. Nevertheless, further research should be undertaken in order to reveal special features inherent to this phase.

2.3. Compound $Bi_2Fe(SeO_3)_2OCl_3$

As seen from the above-mentioned data, the majority of selenite halides with described magnetic properties were studied in compounds featuring copper in the oxidation state 2+ which have S = 1/2. An example of a compound where ions with larger spin values may form magnetic sublattice is selenite oxochloride of iron and bismuth $Bi_2Fe(SeO_3)_2OCl_3$ [30] (Table 1 compound 12). The main feature of the crystal structure of this compound is the existence of the zig-zag chains of corner-shared [FeO_6] octahedra which are decorated by [BiO_4Cl_3], [BiO_3Cl_3] polyhedra and SeO_3^{2-} groups as shown in Figure 11. The selenium atoms are connected to the oxygen atoms from different [FeO_6] octahedra and an additional link chain. Different iron octahedron chains are bound by Bi-polyhedra into the layer in the ab plane of the structure as depicted in Figure 11. Finally, the distance between nearest Fe^{3+} ions in the chain is about 3.56 Å and between Fe^{3+} ions from different chains and layers are 8.570(2) and 8.604(2) Å. According to this structure's peculiarity, it may be suggested that the compound will be magnetically quasi-one-dimensional.

An extensive study is required to establish the character of magnetic behavior in this compound. The temperature dependence of magnetic susceptibility displays broad maximum at T ≈ 130 K, which indicates the formation of the short-range magnetic order (Figure 12). At lower temperature T_N = 13 K, long-range antiferromagnetic ordering sets in, and this is confirmed by means of magnetization and specific heat measurements as well as by Mössbauer spectra. ESR spectroscopy data point out the quasi-1D nature of magnetic interactions. The first-principle calculations allowed defining of the main spin-exchange paths in the magnetic structure based on weakly interacted spin-5/2 zig-zag chains with strong intrachain interactions (Figure 13). Thus, a compound with a higher spin magnetic system has been demonstrated to be a low-dimensional magnet.

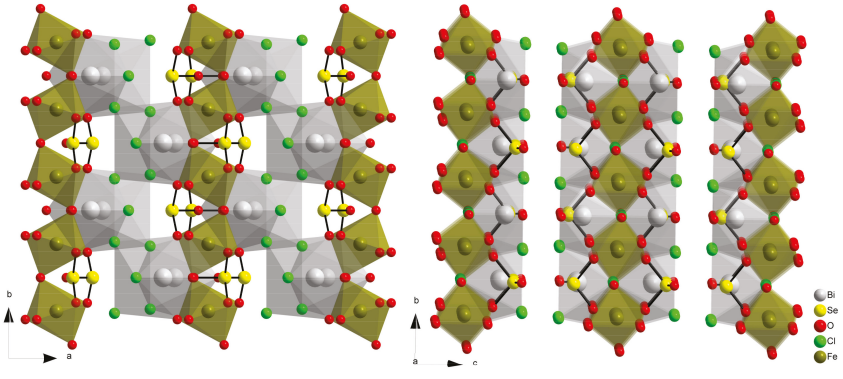

Figure 11. The view on [FeO_6] octahedra chains decorated by Bi polyhedra and SeO_3^{2-} groups in the crystal structure of $Bi_2Fe(SeO_3)_2OCl_3$.

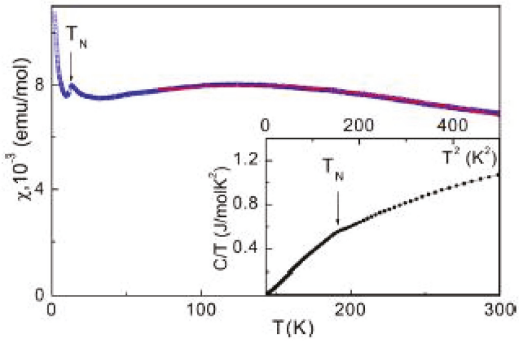

Figure 12. Temperature dependence of magnetic susceptibility in $Bi_2Fe(SeO_3)_2OCl_3$. The solid line represents the fit in a Heisenberg S = ∞ antiferromagnetic chain model. The inset represents the temperature dependence of specific heat on the C/T vs. T^2 scale. Reprinted with permission from [30] Copyright (2014) American Chemical Society.

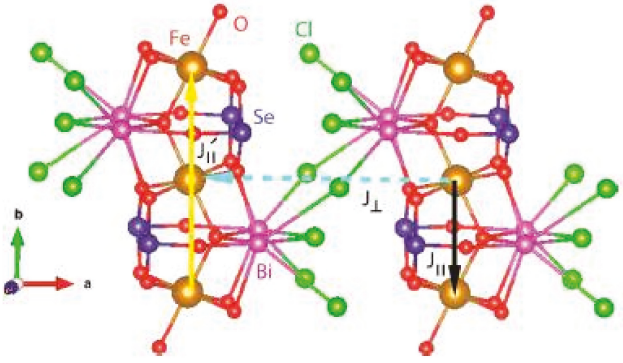

Figure 13. Exchange paths for various magnetic interactions $J_{\parallel}$ (in black), $J_{\parallel}'$ (in cyan), and $J_{\perp}$ (in gold) in $Bi_2Fe(SeO_3)_2OCl_3$. Reprinted with permission from [30]. Copyright (2014) American Chemical Society.

2.4. Francisite Like Compounds $Cu_3M(SeO_3)_2O_2X$

The Table 1 shows that the most representative group of compounds with the same structure symmetry and relative cell constants is formed by compounds with common composition $Cu_3M(SeO_3)_2O_2X$ [31–37] (Compounds 13–30 Table 1). All these compounds are isostructural to the rare nature mineral Francisite $Cu_3Bi(SeO_3)_2O_2Cl$ [47]. Later, its synthetic analogs for Cl, Br, and I were prepared in laboratory conditions [31]. It was shown that rare Earth metals may form compounds with francisite-like structures [32–36]. The crystal structure of francisite contains two copper ions positions with square planar oxygen atom coordination. Bismuth or rare Earth metal ions are in distorted cubic surroundings $[MO_8]$. The square planes $[CuO_4]$ form kagome-like nets in the crystal structure (Figure 14). As can be seen in the Figure 14 selenite groups connect $[CuO_4]$ planes and $[MO_8]$ cubes into the 3D framework with the channels running along [0 0 1] direction. Halide atoms are situated inside these channels. The nearest distance from Cl atom is Cu–Cl which is more than 3 Å for $Cu_3Bi(SeO_3)_2O_2Cl$ (Figure 14). The most recent studies have shown that francisite-like compounds may be formed for all are Earth Metals from La up to Lu and Y in case of chlorides [35,36] and for La till Gd in case of bromides [36]. This phenomenon may be explained by the halide ion size factor where bigger bromide ions could not be combined with smaller Rare Earths and the structure could

not be formed [36]. The Kagome net in the francisite-like structures is not planar and form waves as shown in Figure 15. The main attractive structural feature of francisite-like compounds is that the variation of M^{3+} ion may affect Cu–Cu distance in the Kagome nets. One would expect that Cu–Cu contact distances should decrease with decreasing Ln^{3+} ionic radii. The experimental data summarized for chlorides in Figure 16. support such an approach but Cu1-Cu2-Cu1 angle of the net shows a more complex dependence. There are two Cu–Cu distances in the net. The Cu–Cu distances in chloride compounds are within the range of 3.13–3.23 Å. Figure 16 shows that the differences in the Cu–Cu distances decrease together with decreasing of Ln^{3+} radii. The variation of M^{3+} and of halide ions provides an opportunity for the copper sublattice tuning. Substitution of selenium by tellurium produced the compound $Cu_3Bi(TeO_3)_2O_2Cl$ [48]. However, the copper Kagome net in the tellurite is more distorted and one copper atom has become pyramidally coordinated [CuO_4Cl]. The existence of such a wide group of compounds with similar structures, together with the possibility to examine the influence of the f-element magnetic nature on the magnetic behavior of the copper ions sublattice stimulate the research of this group of substances.

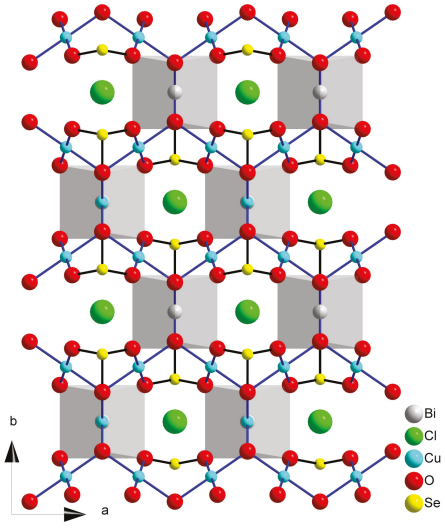

Figure 14. The crystal structure of $Cu_3Bi(SeO_3)_2Cl$. [BiO_8] distorted cubes are shown.

The discussion of the magnetic properties of the francisite family representatives should be started with the consideration of the synthetic analogs of this mineral with the composition $Cu_3Bi(SeO_3)_2O_2X$ (X = Cl, Br). According to magnetic susceptibility measurements data, antiferromagnetic ordering in spin-1/2 copper subsystem takes place at 23.5(5) K [31] and 27.4(5) K [49] for $Cu_3Bi(SeO_3)_2O_2Cl$ and $Cu_3Bi(SeO_3)_2O_2Br$, respectively. The magnetic ground state can be described as distorted kagome layers in ab plane, coupled antiferromagnetically. It should be noted that the layers exhibit a canted ferromagnetic spin arrangement. Applying an external magnetic field triggers a metamagnetic transition in both compounds (BC $\approx$ 0.8 T) [49–51]. Many research groups contributed to the studies of the microscopic magnetic structure of the synthetic francisites. These fruitful structural, electromagnetic, and optical studies combined with the theoretical calculations resulted in discoveries of some interesting features of the francisite-like compounds [49–61]. Thus, a structural transition was detected in $Cu_3Bi(SeO_3)_2O_2Cl$, but surprisingly it was not observed in $Cu_3Bi(SeO_3)_2O_2Br$. Moreover, the origin of this transition is still not clear [59–61]. The most recent publications suggest spin-flip-induced multiferroic behavior in $Cu_3Bi(SeO_3)_2O_2Cl$ [57,59] and this might be a consequence of a structural transformation. However, this requires further clarification.

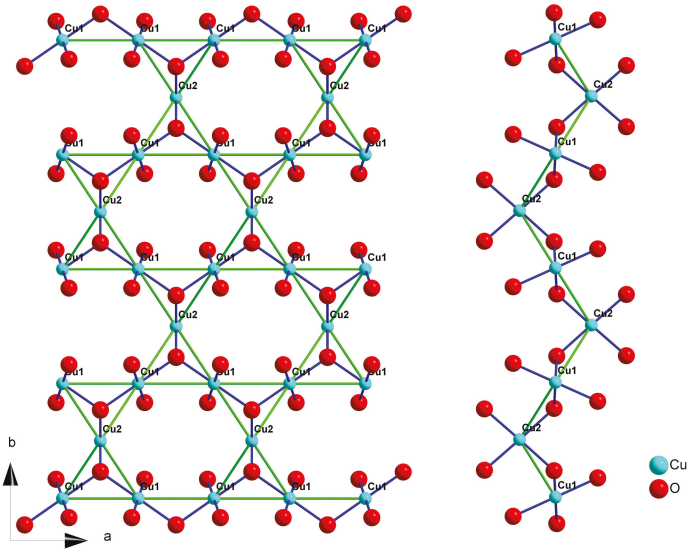

Figure 15. The copper-oxygen net in the crystal structure of Francisite-like compounds crystal structure shown in different direction. Cu–Cu contacts are marked as green. The right part of the figure shows the buckled nature of the kagome net.

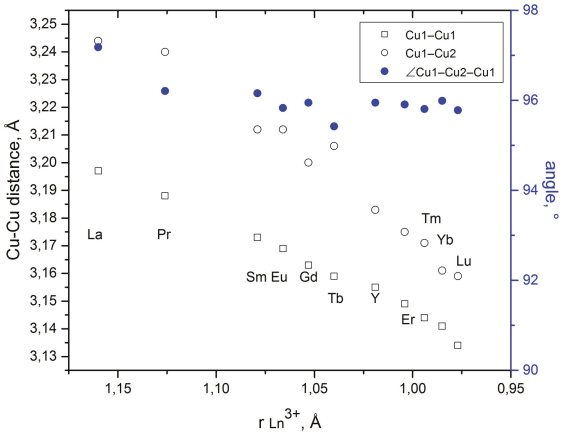

Figure 16. The variation of Cu1-Cu1, Cu1-Cu2, and ∠Cu1-Cu2-Cu1 angles as function of ionic REM radii for $Cu_3Ln(SeO_3)_2O_2Cl$ compounds.

The compounds of composition $Cu_3M(SeO_3)_2O_2X$ (M = La–Lu, X = Cl, Br) may be divided into two groups: the first one containing nonmagnetic rare earth ions such as Y^{3+}, La^{3+}, Eu^{3+}, and Lu^{3+}, and the second one featuring magnetic M^{3+} ions. Representatives of the first group demonstrate magnetic behavior similar to that of $Cu_3Bi(SeO_3)_2O_2X$ (X = Cl, Br) [32,33,35]. χ(T) and M(H) curves typical for francisite-like compounds with non-magnetic rare earth ions are shown in Figure 17. The presence of two magnetic ions in one crystal structure leads to a much more complicated magnetic behavior. It manifests itself in the appearance of the second sharp maximum on the magnetic susceptibility curve at $T < T_N$, as well as on the heat capacity temperature dependence

curve (Figure 18). Up to now a detailed study has been undertaken for only two representatives, which are $Cu_3Sm(SeO_3)_2O_2Cl$ [34] and $Cu_3Yb(SeO_3)_2O_2Cl$ [37]. In both compounds, the magnetic system undergoes the spin-reorientation transition influenced by the rare earth ion's magnetic moment. Exchange paths in the samarium compound are shown in Figure 19.

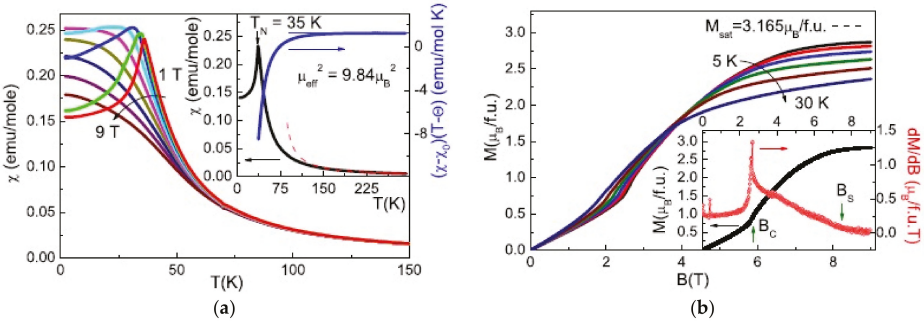

Figure 17. (**a**) The temperature dependence of the magnetic susceptibility of $Cu_3Y(SeO_3)_2O_2Cl$ at applied field strengths of 1–9 T, with a field step of 1 T. The inset represents the temperature dependence of the magnetic susceptibility at 0.1 T along with the Curie constant as a function of temperature. The dotted line represents an extrapolation of the Curie-Weiss type dependence from the high temperature region. (**b**) The field dependence of the magnetization in $Cu_3Y(SeO_3)_2O_2Cl$ over the temperature range of 5–30 K in steps of 5 K. The inset shows the field dependence of the magnetization at 2 K and its field derivative. Reprinted figure with permission from [32] Copyright (2014) by the American Physical Society.

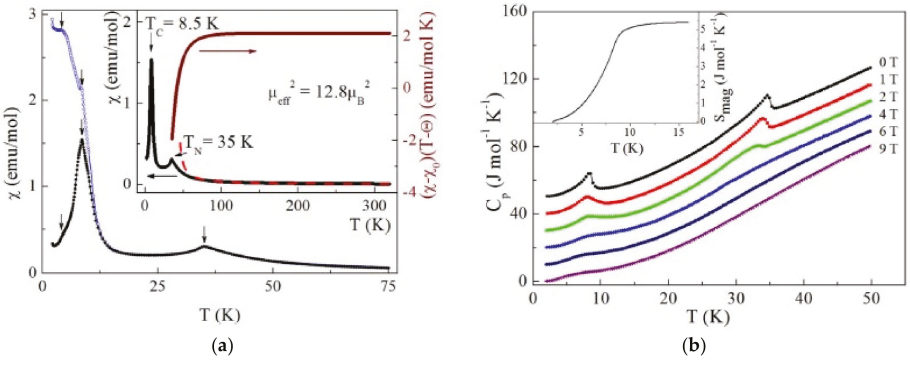

Figure 18. (**a**) The temperature dependences of magnetic susceptibility in $Cu_3Sm(SeO_3)_2O_2Cl$ in ZFC (squares) and FC (circles) regimes taken at B = 0.02 T. Inset: The ZFC curve in the range 2–320 K and its fit (dash). Also shown is the temperature dependence of Curie constant $C = (\chi - \chi_0)(T - \Theta)$. (**b**) The temperature dependences of specific heat in selected magnetic fields for $Cu_3Sm(SeO_3)_2O_2Cl$. Inset: Temperature dependence of magnetic entropy S_{mag} Reprinted figures with permission from [34]. Copyright (2016) by the American Physical Society.

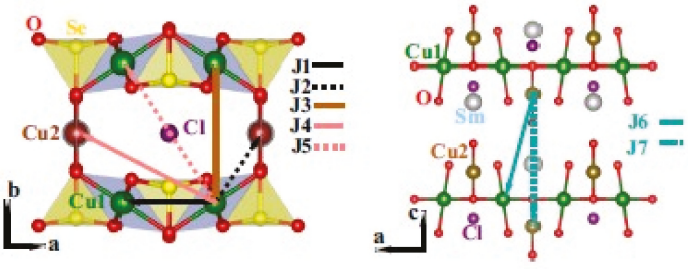

Figure 19. The exchange paths for various magnetic interactions in $Cu_3Sm(SeO_3)_2O_2Cl$. Reprinted figure with permission from [34]. Copyright (2016) by the American Physical Society.

Thus, a series of isostructural compounds have similar magnetic properties, which may be described in terms of a quasi-2D model. In all these compounds an antiferromagnetic transition in the copper subsystem occurs at $T_N \approx 31$–41 K. In case of $Cu_3M(SeO_3)_2O_2Cl$ (M = Y, La, Eu, Lu) it can be seen that the linear decrease of the ionic radii of M^{3+} leads to the decrease of the unit cell parameters (Table 1), as well as to the increase of T_N and the critical field of metamagnetic transition (Table 2). Further research in this field will enable establishing the relationships between the chemical composition, the crystal structure, and the magnetic properties of compounds in this family.

Table 2. Néel temperatures of antiferromagnetic ordering and metamagnetic transitions critical field values for $Cu_3M(SeO_3)_2O_2Cl$ (M = Y, La, Eu, Lu) and $Cu_3M(SeO_3)_2O_2Br$ (M = Bi, La).

	T_N, K	BC, T	Ref.
$Cu_3Bi(SeO_3)_2O_2Br$	27.4	0.8	[49]
$Cu_3La(SeO_3)_2O_2Cl$	31.2	2.4	[33]
$Cu_3La(SeO_3)_2O_2Br$	34.3	2.45	[33]
$Cu_3Eu(SeO_3)_2O_2Cl$	36	2.6	[35]
$Cu_3Y(SeO_3)_2O_2Cl$	36.3	2.6	[32]
$Cu_3Lu(SeO_3)_2O_2Cl$	38	3.0	[35]

2.5. Ilinskite Like Compounds $MCu_5(SeO_3)_2O_2Cl_3$

To the best of our knowledge, the most recently described group of selenite halide d-metal compounds for which structural and physical properties characterization was reported, are copper compounds with alkali metals $MCu_5(SeO_3)_2O_2Cl_3$ M = Na and K [38,39,62,63] and two isostructural halides $Na_2Cu_7(SeO_3)_4O_2X_4$ X = Cl and Br [40,64,65] while the chloride is only magnetically characterized (compounds 31–33 in Table 1). The first group comprises compounds derived from the naturally occurring mineral ilinskite $NaCu_5(SeO_3)_2O_2Cl_3$ [62]. There were obtained synthetic compounds with the same composition and structure for sodium and potassium [38,39,63]. The four copper atoms in the structure may be divided in the two types of planar coordination: $[CuO_4]$ and $[CuO_3Cl]$ (Figure 20a). In $NaCu_5(SeO_3)_2O_2Cl_3$ and $KCu_5(SeO_3)_2O_2Cl_3$ these plaquettes form well-defined layers in the *bc* plane. The layers are bridged by SeO_3^{2-} groups and interleaved by the M^+ ions. The authors of Ref. [36] reported that the pure sodium compound is less stable due to the alkali metal ion size effect. Sodium atoms have five nearest neighbors [(O + 2Cl) + 2Cl] whereas potassium is surrounded by five oxygen and four chlorine atoms. In both compounds there is a group of Cu–Cu distances in the range of 2.85–3.28 Å. The magnetic behavior of $KCu_5(SeO_3)_2O_2Cl_3$ was studied in [63] and may be described by a model of a system built by corner-sharing Cu4 tetrahedra. A part of the Cu sublattice with shortest distances is given in Figure 20b.

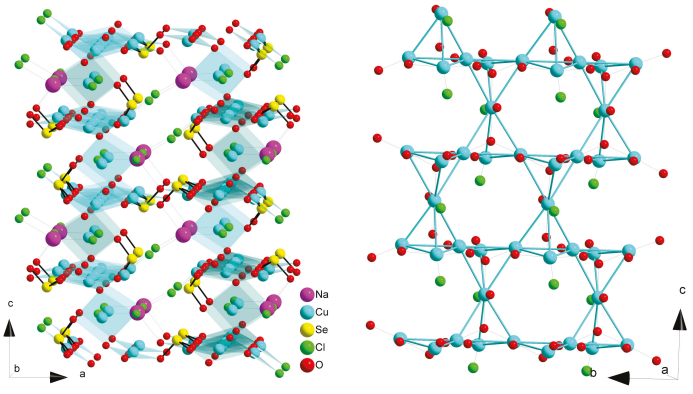

(**a**) (**b**)

Figure 20. The crystal structure of $NaCu_5(SeO_3)_2O_2Cl_3$. Two types of $[CuO_4]$ and $[CuO_3Cl]$ plaquettes are shown (**a**); A fragment of the corner shared Cu_4 tetrahedra sublattice layer in the crystal structure of ilinskite like compounds (**b**).

In spite of the fact that the main motifs of the ilinskite structure are in general similar to those of other copper selenite halides, magnetic behavior of $KCu_5(SeO_3)_2O_2Cl_3$ is drastically different [63]. The χ(T) curve shows broad maximum at T $\approx$ 50 K, but there is no evidence for any long-range order down to 2 K (Figure 21a). The absence of a λ-type anomaly on the Cp(T) curve confirms this (Figure 21b). The negative value of the Curie–Weiss temperature reflects the predominant antiferromagnetic interactions in the magnetic copper sublattice.

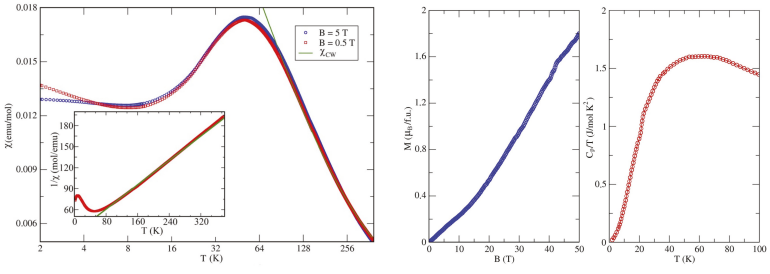

(**a**) (**b**)

Figure 21. (**a**) Magnetic susceptibility χ(T) for $KCu_5O_2(SeO_3)_2Cl_3$ obtained at different values of the external magnetic field in the field-cooling regime. The inset shows the Curie–Weiss approximation in the 100–380 K temperature range with the parameters θ = 60 K and C = 2.3 emu K/mol, as denoted by the green line. (**b**) The magnetization curve measured at T = 1.5 K. (left) Temperature dependence of the specific heat, C_p(T)/T, for $KCu_5O_2(SeO_3)_2Cl_3$ measured in zero field. Reproduced from [63] under Creative Commons Attribution 4.0 International License. To view a copy of this license, visit http://creativecommons.org/licenses/by/4.0/.

Application of DFT calculations combined with thermodynamic measurements resulted in a suggestion of a possible microscopic model of spin interactions in $KCu_5(SeO_3)_2O_2Cl_3$. The magnetic structure can be interpreted as layers of corner-sharing tetrahedra Cu_4 with numerous magnetic interactions between copper atoms. Most of the exchange couplings take place between nearest neighbors, and this would lead to a strong frustration effect, but the influence of non-magnetic SeO_3^{2-} groups results in the reduction of frustration. Dissimilar interactions render the system quasi-1D. Thus,

the magnetic behavior can be described in terms of non-frustrated one-dimensional units (spin ladders or tubes) with only weak and frustrated couplings between these units.

2.6. Compound $Na_2Cu_7(SeO_3)_4O_2Cl_4$

Compound $Na_2Cu_7(SeO_3)_4O_2Cl_4$ [40,65] is an example of a unique structure. There are four independent Cu crystallographic sites. These atoms form heptanuclear clusters (Figure 22 left panel). The Cu–Cu distances in the clusters are in the range of 2.96–3.25 Å. Every cluster is formed by the two tetrahedra connected by a common vertex. Copper atoms in the vertices have the square planar surrounding [CuO_4], two atoms in tetrahedra have the planar coordination [CuO_3Cl] and finally one copper atom is surrounded by four oxygen atoms and one chlorine atoms forming [CuO_4Cl] triangular bipyramid. $Na_2Cu_7(SeO_3)_4O_2Cl_4$ displays a three-dimensional network built by isolated $[Cu_7O_{14}Cl_4]^{18-}$ clusters connected by SeO_3^{2-} groups (right panel of Figure 22), in which Na^+ ions are located inside the vacancies. The same structure was found for the bromide analog $Na_2Cu_7(SeO_3)_4O_2Br_4$ [64] taking into account that Cu–O and Na–O distances are elongated compared to the chloride compound.

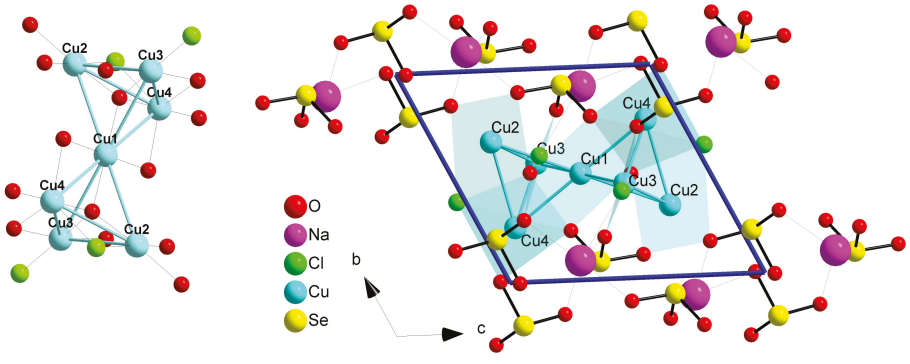

Figure 22. $[Cu_7O_{14}Cl_4]^{18-}$ cluster (left) and the copper polyhedra with SeO_3^{2-} groups in the crystal structure of $Na_2Cu_7(SeO_3)_4O_2Cl_4$ (right) [40].

In $Na_2Cu_7(SeO_3)_4O_2Cl_4$, antiferromagnetic long-range ordering takes place below $T_N \approx 5$ K. The Curie–Weiss temperature value is indicative of predominant antiferromagnetic interactions between the copper atoms. Field dependent magnetization measurements data specify the spin-flip magnetic transition. The presence of a hysteresis loop may be attributed to the ferromagnetic ground state. A magnetization plateau was observed in the magnetization curve, corresponding likely to the 3/7 magnetization plateau suggested by theoretical prediction in a reverse triangular spin-bipyramid. This data allowed proposal of a geometrical model for possible spin arrangements in magnetic sublattice.

The existence of a group with an odd number of possible spin interactions should lead to the spin-frustration effect within such groups. For $Na_2Cu_7(SeO_3)_4O_2Cl_4$ this effect was indeed found [40]. A frustration effect was evaluated using the empirical frustration parameter f:

$$f = \frac{|\Theta_{CW}|}{T_N}$$

The value of f > 10 indicates a strong frustration effect. For the above-mentioned compound this value is calculated to be 13.6, and it is comparable with those calculated for similar known compounds with a magnetic frustration.

3. Conclusions and Outlook

We have attempted to show that interesting magnetic interactions in 3-D metal selenite halides appear due to the influence of lone pairs of SeO_3^{2-} groups and the affinity of halide ions to bind with metal ions instead of selenium. In addition to the described compounds there are a lot of selenite halides with promising crystal structures. Some of such compounds were mentioned by us previously. For example, the compound $Cu_5(SeO_3)_4Br_2$ [64] (Table 3) shows dimorphism and crystallizes in α form which is isostructural to $Cu_5(SeO_3)_4Cl_2$ [22] whereas β form is close to $Co_5(SeO_3)_4X_2$ X = Cl, Br [23] and $Ni_5(SeO_3)_4Br_2$ [25]. Both α and β polymorphs show 3-D Cu–Cu frameworks with Cu–Cu distances 3.16–3.61 and 3.10–3.44 Å, respectively. Such values suggest the magnetic exchange between copper ions in $Cu_5(SeO_3)_4Br_2$. A similar situation may be observed in case of $Na_2Cu_7(SeO_3)_4O_2Br_4$ [64] (Table 3), an analog of the frustrated chloride compound [40]. $Na_2Cu_7(SeO_3)_4O_2Br_4$ demonstrates the same isolated $[Cu_7O_{14}Br_4]^{18-}$ clusters with Cu–Cu distances 2.96–3.27 Å close to those in $Na_2Cu_7(SeO_3)_4O_2Cl_4$ [40].

Another alkali metal copper selenite chloride $K[Cu_3O](SeO_3)_2Cl$ [65] possesses a very interesting, unprecedented structure (Table 3). The unit cell of $K[Cu_3O](SeO_3)_2Cl$ contains three Cu^{2+} ions, two in $[CuO_4]$ plane coordination and squeezed tetrahedra and one $[CuO_4Cl]$ polyhedron. Copper atoms are situated in the range 2.94–3.35 Å and form layers in the structure of $K[Cu_3O](SeO_3)_2Cl$. The layer may be presented as formed by edge shared pairs of Cu_4 tetrahedrons which are connected into the layer in ab plane of the crystal structure Figure 23. Distances between copper atoms from different layers are about 6 Å. The system of magnetic exchange of vertex shared tetrahedra was studied in [63]. Compound $K[Cu_3O](SeO_3)_2Cl$ possess different type of tetrahedra connection but it may be expected that magnetic exchange will be found in this compound.

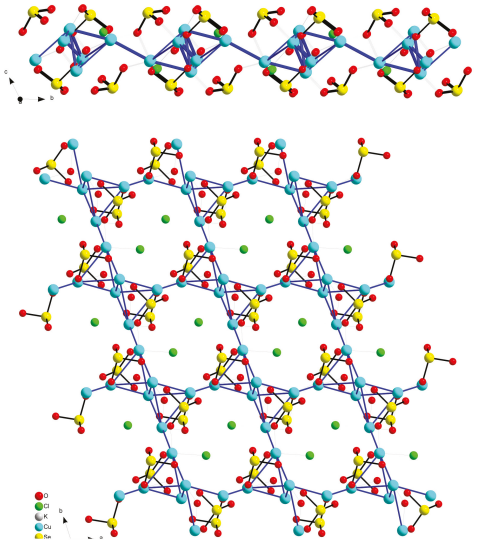

Figure 23. The presentation of the copper-oxygen layer decorated by SeO_3^{2-} groups in different directions in the crystal structure of the $K[Cu_3O](SeO_3)_2Cl$ [65]. Blue lines represent Cu–Cu contacts.

Table 3. Compositions and crystallographic data for transition metals selenite halides with possible magnetic exchange between d-metal ions.

#	Composition	Space Group	Z	Cell Constants				Ref.
				a, Å	b, Å	c, Å	Angles, °	
1	α-$Cu_5(SeO_3)_4Br_2$	$P2_1/c$	2	11.1089(18)	8.3233(13)	7.5668(12)	β = 90.893(3)	[64]
2	β-$Cu_5(SeO_3)_4Br_2$	P-1	1	6.2096(13)	7.8553(16)	7.9006(17)	α = 65.538(6) β = 83.111(7) γ = 75.291(7)	[64]
3	$Na_2Cu_7(SeO_3)_4O_2Br_4$	P-1	4	7.7657(3)	8.3750(3)	9.2626(4)	α = 110.227(2) β = 104.897(2) γ = 107.195(3)	[64]
4	$K[Cu_3O](SeO_3)_2Cl$	P-1	2	7.6821(5)	8.1179(5)	8.7836(6)	α = 113.193(3) β = 108.735(4) γ = 98.245(4)	[65]
5	$Cu_3(SeO_3)_2Cl_2$	C2/m	2	8.9333(12)	6.2164(7)	7.5815(12)	β = 110.238(13)	[66]
6	$Cu_3(SeO_3)_2Cl_2$	P-1	2	6.1240(4)	7.7880(5)	8.5170(6)	α = 92.755(4) β = 95.735(4) γ = 92.853(4)	[15]
7	$Cu_5O_2(SeO_3)_2Cl_2$	$P2_1/c$	2	6.030(1)	13.744(3)	5.562(1)	β = 95.75(1)	[67,68]
8	β-$Cu_5O_2(SeO_3)_2Cl_2$	$P2_1/c$	2	5.3982(5)	8.0543(8)	11.1277(10)	β = 99.258(2)	[69]
9	$Cu_7O_2(SeO_3)_2Cl_6$	$P2_1/c$	4	10.958(9)	14.483(5)	10.494(14)	β = 113.61(7)	[70]
10	$Cu_9O_2(SeO_3)_4Cl_6$	I2/m	2	14.170(3)	6.262(1)	12.999(3)	β = 113.05(1)	[71,72]
11	$Cu_9O_2(SeO_3)_4CI_6$	$P2_1/n$	2	12.922(3)	6.262(2)	14.042(4)	β = 112.88(2)	[73]
12	$Cu^ICu^{II}_4O(SeO_3)Cl_5$	$P2_1/m$	2	9.203(3)	6.232(2)	9.557(3)	β = 91.970(8)	[74]
13	$Co_4(SeO_3)_3Cl_2$	Pnma	4	7.9751(1)	14.4048(2)	9.7103(2)		[75]
14	$Co_3(Se_2O_5)_2Cl_2$	C2/m	2	7.1973(10)	13.9961(19)	5.8334(9)	β = 107.524(16)	[75]
15	$Ba_2Co(SeO_3)_2Cl_2$	Pnnm	2	6.7635(4)	12.6454(7)	5.3866(3)		[76]
16	$Fe_6Ca_2(SeO_3)_9Cl_4$	$P6_3/m$	2	12.118(2)		12.703(4)		[77]
17	$CoNd_{10}(SeO_3)_{12}Cl_8$	P2/c	4	15.699(2)	15.7002(2)	19.171(2)	β = 113,995(5)	[78]

Table 3. *Cont.*

#	Composition	Space Group	Z	Cell Constants				Ref.
				a, Å	b, Å	c, Å	Angles, °	
18	$CoSm(SeO_3)_2Cl$	P-1	4	7.123(1)	8.8895(2)	12.162(2)	α = 72.25(1) β = 71.27(1) γ = 72.08(1)	[79]
19	$CuGd(SeO_3)_2Cl$	P-1	4	7.043(4)	9.096(4)	12.010(7)	α = 70.84(4) β = 73.01(4) γ = 70.69(4)	[79]
20	$MnSm(SeO_3)_2Cl$	P-1	2	7.008(2)	7.241(2)	8.034(2)	α = 86.90(3) β = 71.57(3) γ = 64.33(3)	[79]
21	$Cu^{I}Cu^{II}{}_5PbO_2(SeO_3)_2Cl_5$	C2/m	4	18.468(2)	6.1475(8)	15.314(2)	β = 119.284(2)	[80]
22	$KCdCu_7O_2(SeO_3)_2Cl_9$	$P6_3/mmc$	2	8.7805(8)		15.521(2)		[81]
23	$KPb_{1.5}Cu_6Zn(SeO_3)_2O_2Cl_{10}$	Pnnm	4	9.132(2)	19.415(4)	13.213(3)		[82]
24	$MnBi(SeO_3)_2Cl$	P-1	2	7.0926(8)	7.2695(6)	8.0160(8)	α = 88.226(4) β = 72.005(3) γ = 64.560(4)	[83,84]
25	$(Pb_2Cu^{2+}{}_9O_4)(SeO_3)_4(Cu^{+}Cl_2)Cl_5$	C2/m	2	18.605(17)	6.204(6)	12.673(12)	β = 109.869(17)	[85]
26	$(PbCu^{2+}{}_5O_2)(SeO_3)_2(Cu^{+}Cl_2)Cl_3$	C2/m	2	18.4956(4)	6.14540(10)	15.2985(4)	β = 119.3111(10)	[85]
27	$(Pb_xCu^{2+}{}_{(6-x)}O_2)(SeO_3)_2(Cu^{+}Cl_2)K_{(1-x)}Cl_{(4-x)}$	C2/m	1	15.1158(11)	6.1853(4)	9.2672(9)	β = 95.965(5)	[85]
28	$Pb_2VO_2(SeO_3)_2Cl$	$P2_1$	2	8.333(3)	5.3171(16)	10.710(4)	β = 111.701(5)	[86]
29	$Pb_5Cu(SeO_3)_4Cl_4$	C2/c	4	24.917(3)	5.5060(10)	14.242(2)	β = 101.770(10)	[87]

In addition to the listed compounds, some other selenite halide 3d-metals have been described in the literature and structurally characterized. These are $Cu_3(SeO_3)_2Cl_2$ [15,66], $Cu_5O_2(SeO_3)_2Cl_2$ [67–69], $Cu_7O_2(SeO_3)_2Cl_6$ [70], $Cu_9O_2(SeO_3)_4Cl_6$, [71–73], $Cu^{I}Cu^{II}{}_4O(SeO_3)Cl_5$ [74], $Co_4(SeO_3)_3Cl_2$ [75], and the diselenite cobalt compound $Co_3(Se_2O_5)_2Cl_2$ [75]. Symmetries and cell constants for these compounds are listed in Table 3. As follows from the listed data these compounds frequently form polymorphs and some of them were found in nature as copper minerals Georgbokiite [67,68,88], Parageorgbokiite [69], Nicksobolevite [70], and Chloromenite [72] while in the laboratory conditions other crystal polymorphs may be obtained. These compounds, if they will be obtained in the phase-pure form or as crystals suitable for measurements, appear as good objects for metal–metal ions magnetic exchange studies. The majority of the listed compounds show M–M distances in the range of 2.9–3.4 Å. Taking into account these distances, a complex nature of the magnetic exchange in the compounds under consideration may be expected. From the crystallographic point of view, the most attractive compounds are layered monoclinic C2/m modifications of $Cu_3(SeO_3)_2Cl_2$ [66] and cobalt diselenite chloride $Co_3(Se_2O_5)_2Cl_2$ [75], where chains of $[CoO_4Cl_2]$ octahedra are divided by diselenite $Se_2O_5{}^{2-}$ groups in the crystal structure Figure 24. The compound $Cu^{I}Cu^{II}{}_4O(SeO_3)Cl_5$ [74] is a good example of a structure where Cu^{2+} ions form complex chains in the crystal structure separated by chains constructed by $[Cu^{I}Cl_3]^{2-}$ triangles, as shown in Figure 25.

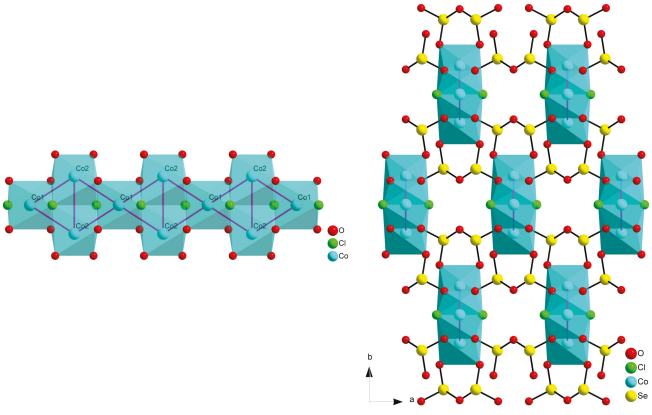

Figure 24. The chain built by $[CoO_4Cl_2]$ octahedra in the crystal structure of $Co_3(Se_2O_5)Cl_2$ (left) and view on chains interconnected by diselenite groups (right) [75].

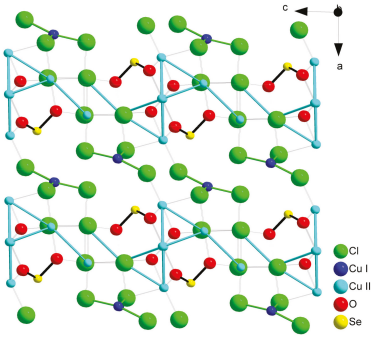

Figure 25. The complex chains of Cu^{2+} ions in the structure of $Cu^{I}Cu^{II}{}_4O(SeO_3)Cl_5$ [74] separated by $[Cu^{I}Cl_3]^{2-}$ groups and decorated by $SeO_3{}^{2-}$ groups.

As a 3d transition metal, zinc forms a selenite chloride known as mineral Sophiite with the composition $Zn_2(SeO_3)Cl_2$ [89] and its synthetic polymorph [90] but due to its $3d^{10}$ electron configuration it cannot possess magnetic properties.

Recently, a new tellurite-selenite chloride of iron with the composition $Fe[(Te_{1.5}Se_{0.5})O_5]Cl$ has been prepared and structurally characterized [91]. The composition of this compound is close to that of $FeTe_2O_5Cl$ [13] that shows a unique structure and possesses interesting magnetic properties, see for example [92–95]. The mixed selenite tellurite chloride of iron (III) shows the different structure [91] which is layered and contains dimers of the $[FeO_5Cl]$ octahedra, linked via common O–O edges, and mixed $[Te_3SeO_{10}]^{4-}$ tetramers. The Fe–Fe distance in the $[Fe_2O_8Cl_2]$ dimers is 3.30 Å and suggests some kind of magnetic exchange at least between Fe–Fe ions in these groups.

In addition to the above-mentioned compounds and compositions, some more complex mixed cation selenite halides have been described in the literature and may attract attention due to the possible low dimensional magnetism of 3d metal ions sublattice (Table 3 substances 15–29) [76–87]. Some of them were found in nature as minerals [80–82]. Among the listed compounds, the compounds of Mn^{2+} $MnSm(SeO_3)_2Cl$ [79] and $MnBi(SeO_3)_2Cl$ [84] deserve mentioning. The magnetic behavior of Mn^{2+} ions with S = 5/2 as well as of chromium (III) compounds in selenite halides was not described at all. To the best of our knowledge even selenites of chromium are less explored than the iron analogues. According to the literature data [96] diselenites $M_2(Se_2O_5)_3$ M = Fe, Cr crystallize in the same structures and behave as three-dimensional isotropic antiferromagnets with the weak antiferromagnetic coupling of M^{3+} ions at relatively high temperatures, but at low temperature $Fe_2(Se_2O_5)_3$ possesses a long range AF order while $Cr_2(Se_2O_5)_3$ does not, according to [96].

As was mentioned in the introduction, selenites (selenium (IV) compounds) are strong oxidants. The compound $Pb_2VO_2(SeO_3)_2Cl$ (Table 3 compound 28) [86] is the only example of vanadium selenite halides, but in this compound the V atom is in the oxidation state +5 and has no valence electrons and could not display any magnetic interaction. For this reason, there is no data about the selenite halide compounds with V or Ti in low oxidation states, as well as with Fe^{2+} or Mn^{3+}. At the same time, an anhydrous selenite of Mn(II) and Mn(III), namely, $Mn_3O(SeO_3)_3$ is known [97] suggesting the possibility to obtain manganese selenite halides. As it was demonstrated for Bi compounds with the francisite type of structures, the properties may be varied within one structure type by changing the halide ion (chloride for bromide). This serves as an attractive approach to find new compounds because bromides may sometimes show different structures and magnetic properties compared to chlorides, as evidenced for example by $Ni_5(SeO_3)_4Cl_2$ and $Ni_5(SeO_3)_4Br_2$ [24,25]. It is obvious that selenite iodides are difficult to prepare due to the possible facile oxidation of the iodide ions, but the existence of $Pb_3(SeO_3)_2I_2$ [98] and $Cu_3Bi(SeO_3)_2O_2I$ [31] demonstrates the possibility to find proper synthesis conditions and therefore opens further opportunities for future research.

The existence of the wide range of compounds for which it is possible to expect low-dimensional magnetic interactions gives reason for chemists to develop synthetic methods suitable for the preparation of these substances in the phase-pure form or as large single crystals.

In conclusion, we would like to underline again that 3d transition metal selenites, as well as closely related tellurites, are a promising and attractive family of inorganic compounds with rich crystal chemistry and possible occurrence of low-dimensional magnetic subsystems with a wide variety of topologies.

Acknowledgments: This work was supported by the Russian Foundation for Basic Research (RFBR) (Grants 16-03-00463a and 18-52-52005MHTa). S.S., University of Antwerp, and R.A.G. are acknowledged for discussion of the manuscript.

Author Contributions: All authors wrote parts of this work. P.S.B. coordinated the project.

Conflicts of Interest: The authors declare no conflict of interest.

References

1. Schiffer, P. Condensed-matter physics: Magnetic frustration squeezed out. *Nature* **2002**, *420*, 35–38. [CrossRef] [PubMed]
2. Balents, L. Spin liquids in frustrated magnets. *Nature* **2010**, *464*, 199–208. [CrossRef] [PubMed]
3. Hess, C. Heat conduction in low-dimensional quantum magnets. *Eur. Phys. J. Spec. Top.* **2007**, *151*, 73–83. [CrossRef]
4. Gillespie, R.J.; Hargittai, I. *The VSEPR Model of Molecular Geometry*; Prentice-Hall: Upper Saddle River, NJ, USA, 1991; 6990p, ISBN 978-0205123698.
5. Gillespie, R.J. The VSEPR model revisited. *Chem. Soc. Rev.* **1992**, *21*, 59–69. [CrossRef]
6. Galy, J.; Meunier, G.; Andersson, G.; Åstrtöm, A. Stéréochimie des Eléments Comportant des Paires Non Liées: Ge (II), As (III), Se(IV), Br (v), Sn (II), Sb(III), Te (IV), I (V), Xe(VI), Tl (I), Pb (II), et Bi (III) (Oxydes, Fluorures et Oxyfluorures). *J. Solid State Chem.* **1975**, *13*, 142–159. [CrossRef]
7. Mao, J.-G.; Jiang, H.-L.; Kong, F. Structures and Properties of Functional Metal Selenites and Tellurites. *Inorg. Chem.* **2008**, *47*, 8498–8510. [CrossRef] [PubMed]
8. Wickleder, M.S.; Logemann, C. Compounds Containing the Chalcogen Oxygen E–O Bond (E = S, Se, Te). In *Handbook of Chalcogen Chemistry: New Perspectives in Sulfur, Selenium and Tellurium*, 2nd ed.; Devillanova, F.A., du Mont, W.W., Eds.; RSC Publishing: Cambridge, UK, 2013; Volume 1, pp. 307–345. ISBN 978-1-84973-623-7.
9. Vanýsek, P. Electrochemical series. In *CRC Handbook of Chemistry and Physics*, 97th ed.; W.M. Haynes CRC Press: Boca Raton, FL, USA, 2016; pp. 5-78–5-84. ISBN 978-1-4987-5429-3.
10. Christy, A.G.; Mills, S.J.; Kampf, A.R. A review of the structural architecture of tellurium oxycompounds. *Mineral. Mag.* **2016**, *80*, 415–545. [CrossRef]
11. Johnsson, M.; Törnroos, K.W.; Mila, F.; Millet, P. Tetrahedral Clusters of Copper(II): Crystal Structures and Magnetic Properties of $Cu_2Te_2O_5X_2$ (X = Cl, Br). *Chem. Mater.* **2000**, *12*, 2853–2857. [CrossRef]
12. Johnsson, M.; Törnroos, K.W.; Lemmens, P.; Millet, P. Crystal Structure and Magnetic Properties of a New Two-Dimensional S = 1 Quantum Spin System $Ni_5(TeO_3)_4X_2$ (X = Cl, Br). *Chem. Mater.* **2003**, *15*, 68–73. [CrossRef]
13. Becker, R.; Johnsson, M.; Kremer, R.K.; Klauss, H.-H.; Lemmens, P. Crystal Structure and Magnetic Properties of $FeTe_2O_5X$ (X = Cl, Br): A Frustrated Spin Cluster Compound with a New Te(IV) Coordination Polyhedron. *J. Am. Chem. Soc.* **2006**, *128*, 15469–15475. [CrossRef] [PubMed]
14. Becker, R.; Johnsson, M.; Kremer, R.; Lemmens, P. Crystal structure and magnetic properties of $Cu_3(TeO_3)_2Br_2$—A layered compound with a new Cu(II) coordination polyhedron. *J. Solid State Chem.* **2005**, *178*, 2024–2029. [CrossRef]
15. Millet, P.; Bastide, B.; Johnsson, M. $Cu_3(SeO_3)_2Cl_2$: A new oxochloride of copper(II) and selenium(IV). *Solid State Commun.* **2000**, *113*, 719–723. [CrossRef]
16. Lemmens, P.; Millet, P. Spin—Orbit—Topology, a triptych. In *Quantum Magnetism*; Lecture Notes in Physics; Schollwöck, U., Richter, J., Farnell, D.J.J., Bishop, R.F., Eds.; Springer: Berlin/Heidelberg, Germany, 2004; Volume 645, pp. 433–477. ISBN 978-3-540-40066-0. [CrossRef]
17. Cao, X.-L.; Hu, C.-L.; Xu, X.; Kong, F.; Mao, J.-G. $Pb_2TiOF(SeO_3)_2Cl$ and $Pb_2NbO_2(SeO_3)_2Cl$: Small changes in structure induced a very large SHG enhancement. *Chem. Commun.* **2013**, *49*, 9965–9967. [CrossRef] [PubMed]
18. Hu, S.; Johnsson, M.; Law, J.M.; Bettis, J.L., Jr.; Whangbo, M.-H.; Kremer, R.K. Crystal Structure and Magnetic Properties of the S = 1/2 Quantum Spin System $Cu_7(TeO_3)_6F_2$ with Mixed Dimensionality. *Inorg. Chem.* **2014**, *53*, 4250–4256. [CrossRef] [PubMed]
19. Hu, S.; Johnsson, M. Synthesis and crystal structure of two synthetic oxofluoride framework compounds—$Co_2TeO_3F_2$ and $Co_2SeO_3F_2$. *Dalton Trans.* **2012**, *41*, 12786–12789. [CrossRef] [PubMed]
20. Orive, J.; Balda, R.; Fernández, J.; Lezamad, L.; Arriortua, M.I. Low temperature red luminescence of a fluorinated Mn-doped zinc selenite. *Dalton Trans.* **2013**, *42*, 12481–12494. [CrossRef] [PubMed]
21. Liang, M.-L.; Ma, Y.-X.; Hu, C.-L.; Kong, F.; Mao, J.-G. $A(VO_2F)(SeO_3)$ (A = Sr, Ba) and $Ba(MOF_2)(TeO_4)$ (M = Mo, W): First examples of alkali-earth selenites/tellurites with a fluorinated d^0-TM octahedron. *Dalton Trans.* **2018**, *47*, 1513–1519. [CrossRef] [PubMed]

22. Zhang, D.; Berger, H.; Kremer, R.K.; Wulferding, D.; Lemmens, P.; Johnsson, M. Synthesis, Crystal Structure, and Magnetic Properties of the Copper Selenite Chloride $Cu_5(SeO_3)_4Cl_2$. *Inorg. Chem.* **2010**, *49*, 9683–9688. [CrossRef] [PubMed]
23. Becker, R.; Prester, M.; Berger, H.; Lin, P.H.; Johnsson, M.; Drobac, D.; Zivkovic, I. Crystal structure and magnetic properties of two new cobalt selenite halides: $Co_5(SeO_3)_4X_2$ (X = Cl, Br). *J. Solid State Chem.* **2007**, *180*, 1051–1059. [CrossRef]
24. Shen, Y.-L.; Mao, J.-G.; Jiang, H.-L. Synthesis, crystal structure and magnetic property of a new nickel selenite chloride: $Ni_5(SeO_3)_4Cl_2$. *J. Solid State Chem.* **2005**, *178*, 2942–2946. [CrossRef]
25. Jiang, H.-L.; Mao, J.-G. New Members in the $Ni_{n+1}(QO_3)_nX_2$ Family: Unusual 3D Network Based on Ni_4ClO_3 Cubane-like Clusters in $Ni_7(TeO_3)_6Cl$. *Inorg. Chem.* **2006**, *45*, 7593–7599. [CrossRef] [PubMed]
26. Berdonosov, P.S.; Olenev, A.V.; Kuznetsov, A.N.; Dolgikh, V.A. A group of new selenite-chlorides of strontium and d-metals (Co, Ni): Synthesis, thermal behavior and crystal chemistry. *J. Solid State Chem.* **2009**, *182*, 77–82. [CrossRef]
27. Berdonosov, P.S.; Olenev, A.V.; Dolgikh, V.A. Strontium–copper selenite–chlorides: Synthesis and structural investigation. *J. Solid State Chem.* **2009**, *182*, 2368–2373. [CrossRef]
28. Janson, O.; Tsirlin, A.A.; Osipova, E.S.; Berdonosov, P.S.; Olenev, A.V.; Dolgikh, V.A.; Rosner, H. $CaCu_2(SeO_3)_2Cl_2$: Spin-1/2 Heisenberg chain compound with complex frustrated interchain couplings. *Phys. Rev.* **2011**, *B83*, 144423. [CrossRef]
29. Berdonosov, P.S.; Janson, O.; Olenev, A.V.; Krivovichev, S.V.; Rosner, H.; Dolgikh, V.A.; Tsirlin, A.A. Crystal structures and variable magnetism of $PbCu_2(XO_3)_2Cl_2$ with X = Se, Te. *Dalton Trans.* **2013**, *42*, 9547–9554. [CrossRef] [PubMed]
30. Berdonosov, P.S.; Kuznetsova, E.S.; Dolgikh, V.A.; Sobolev, A.V.; Presniakov, I.A.; Olenev, A.V.; Rahaman, B.; Saha-Dasgupta, T.; Zakharov, K.V.; Zvereva, E.A.; et al. Crystal Structure, Physical Properties, and Electronic and Magnetic Structure of the Spin S = 5/2 Zigzag Chain Compound $Bi_2Fe(SeO_3)_2OCl_3$. *Inorg. Chem.* **2014**, *53*, 5830–5838. [CrossRef] [PubMed]
31. Millet, P.; Bastide, B.; Pashchenko, V.; Gnatchenko, S.; Gapon, V.; Ksarid, Y.; Stepanov, A. Syntheses, crystal structures and magnetic properties of francisite compounds $Cu_3Bi(SeO_3)_2O_2X$ (X = Cl, Br and I). *J. Mater. Chem.* **2001**, *11*, 1152–1157. [CrossRef]
32. Zakharov, K.V.; Zvereva, E.A.; Berdonosov, P.S.; Kuznetsova, E.S.; Dolgikh, V.A.; Clark, L.; Black, C.; Lightfoot, P.; Kockelmann, W.; Pchelkina, Z.V.; et al. Thermodynamic properties, electron spin resonance, and underlying spin model in $Cu_3Y(SeO_3)_2O_2Cl$. *Phys. Rev.* **2014**, *B90*, 214417. [CrossRef]
33. Markina, M.M.; Zakharov, K.V.; Zvereva, E.A.; Denisov, R.S.; Berdonosov, P.S.; Dolgikh, V.A.; Kuznetsova, E.S.; Olenev, A.V.; Vasiliev, A.N. Static and dynamic magnetic properties of two synthetic francisites $Cu_3La(SeO_3)_2O_2X$ (X = Br and Cl). *Phys. Chem. Miner.* **2017**, *44*, 277–285. [CrossRef]
34. Zakharov, K.V.; Zvereva, E.A.; Markina, M.M.; Stratan, M.I.; Kuznetsova, E.S.; Dunaev, S.F.; Berdonosov, P.S.; Dolgikh, V.A.; Olenev, A.V.; Klimin, S.A.; et al. Magnetic, resonance, and optical properties of $Cu_3Sm(SeO_3)_2O_2Cl$: A rare-earth francisite compound. *Phys. Rev.* **2016**, *B94*, 054401. [CrossRef]
35. Zakharov, K.V.; Zvereva, E.A.; Kuznetsova, E.S.; Berdonosov, P.S.; Dolgikh, V.A.; Markina, M.M.; Olenev, A.V.; Shakin, A.A.; Volkova, O.S.; Vasiliev, A.N. Two new lanthanide members of francisite family $Cu_3Ln(SeO_3)_2O_2Cl$ (Ln = Eu, Lu). *J. Alloys Comp.* **2016**, *685*, 442–447. [CrossRef]
36. Berdonosov, P.S.; Dolgikh, V.A. Copper Lanthanide Selenite Oxohalides with Francisite Structure: Synthesis and Structural Characteristics. *Russ. J. Inorg. Chem.* **2008**, *53*, 1353–1358. [CrossRef]
37. Markina, M.M.; Zakharov, K.V.; Ovchenko, E.A.; Berdonosov, P.S.; Dolgikh, V.A.; Kuznetsova, E.S.; Olenev, A.V.; Klimin, S.A.; Kashchenko, M.A.; Budkin, I.V.; et al. Interplay of rare-earth and transition-metal subsystems in $Cu_3Yb(SeO_3)_2O_2Cl$. *Phys. Rev.* **2017**, *B94*, 134422. [CrossRef]
38. Krivovichev, S.V.; Filatov, S.K.; Vergasova, L.P. The crystal structure of ilinskite, $NaCu_5O_2(SeO_3)_2Cl_3$, and review of mixed-ligand CuO_mCl_n coordination geometries in minerals and inorganic compounds. *Miner. Petrol.* **2013**, *107*, 235–242. [CrossRef]
39. Kovrugin, V.M.; Siidra, O.I.; Colmont, M.; Mentré, O.; Krivovichev, S.V. Emulating exhalative chemistry: Synthesis and structural characterization of ilinskite, $Na[Cu_5O_2](SeO_3)_2Cl_3$, and its K-analogue. *Miner. Petrol.* **2015**, *109*, 421–430. [CrossRef]

40. Tang, Y.; Guo, W.; Zhang, S.; Xiang, H.; Cui, M.; He, Z. $Na_2Cu_7(SeO_3)_4O_2Cl_4$: A selenite chloride compound with Cu7 units showing spin-frustration and a magnetization plateau. *Dalton Trans.* **2016**, *45*, 8324–8326. [CrossRef] [PubMed]
41. Yun, Y.; Wan, W.; Rabbani, F.; Su, J.; Xu, H.; Hovmöler, S.; Johnsson, M.; Zou, X. Phase identification and structure determination from multiphase crystalline powder samples by rotation electron diffraction. *J. Appl. Cryst.* **2014**, *47*, 2048–2054. [CrossRef]
42. Becker, R.M.; Prester, H.; Berger, M.; Johnsson, D.; Drobac, I. Zivkovic Crystal structure and magnetic properties of the new cobalt tellurite halide $Co_5(TeO_3)_4X_2$ (X = Cl, Br). *Solid State Sci.* **2007**, *9*, 223–230. [CrossRef]
43. Takagi, R.; Johnsson, M.; Kremer, R.K.; Lemmens, P. Crystal structure and magnetic properties of the coupled spin dimer compound $SrCu_2(TeO_3)_2Cl_2$. *J. Solid State Chem.* **2006**, *179*, 3763–3767. [CrossRef]
44. Feger, C.R.; Kolis, J.W. Synthesis and Characterization of Two New Copper Tellurites, $Ba_2Cu_4Te_4O_{11}Cl_4$ and $BaCu_2Te_2O_6Cl_2$, in Supercritical H_2O. *Inorg. Chem.* **1998**, *37*, 4046–4051. [CrossRef] [PubMed]
45. Shannon, R.D. Revised effective ionic radii and systematic studies of interatomic distances in halides and chalcogenides. *Acta Cryst.* **1976**, *A32*, 751–767. [CrossRef]
46. Berdonosov, P.S.; Dolgikh, V.A.; Tsirlin, A.A.; Janson, O. Copper(II) selenate(IV) chlorides as low-dimensional magnets. In Proceedings of the 18th International Conference on Solid Compounds of Transition Elements, Lisbon, Portugal, 31 March–5 April 2012; p. 215.
47. .Pring, A.; Gatehouse, B.M.; Birch, W.D. Francisite, $Cu_3Bi(SeO_3)_2O_2Cl$, a new mineral from Iron Monarch, South Australia: Description and crystal structure. *Am. Mineral.* **1990**, *75*, 1421–1425.
48. Becker, R.; Johnsson, M. Crystal structure of $Cu_3Bi(TeO_3)_2O_2Cl$: A Kagomé lattice type compound. *Solid State Sci.* **2006**, *7*, 375–380. [CrossRef]
49. Pregelj, M.; Zaharko, O.; Günther, A.; Loidl, A.; Tsurkan, V.; Guerrero, S. Magnetic ground state and two-dimensional behavior in pseudo-kagome layered system $Cu_3Bi(SeO_3)_2O_2Br$. *Phys. Rev. B* **2012**, *86*, 144409. [CrossRef]
50. Miller, K.H.; Stephens, P.W.; Martin, C.; Constable, E.; Lewis, R.A.; Berger, H.; Carr, G.L.; Tanner, D.B. Infrared phonon anomaly and magnetic excitations in single-crystal $Cu_3Bi(SeO_3)_2O_2Cl$. *Phys. Rev.* **2012**, *B86*, 174104. [CrossRef]
51. Nikolaev, S.A.; Mazurenko, V.V.; Tsirlin, A.A.; Mazurenko, V.G. First-principles study of the magnetic ground state and magnetization process of the kagome francisites $Cu_3Bi(SeO_3)_2O_2X$ (X = Cl, Br). *Phys. Rev.* **2016**, *B94*, 144412. [CrossRef]
52. Miller, K.H.; Constable, E.; Berger, H.; Tanner, D.B.; Horvat, J. Complementary techniques for probing terahertz magnetic excitations in $Cu_3Bi(SeO_3)_2O_2Cl$. In Proceedings of the International Conference on Infrared, Millimeter, and Terahertz Waves, IRMMW-THz, Wollongong, NSW, Australia, 23–28 September 2012; pp. 1–2.
53. Wang, Z.; Schmidt, M.; Goncharov, Y.; Tsurkan, V.; Krug von Nidda, H.-A.; Loidl, A.; Deisenhofer, J. Terahertz spectroscopy in the pseudo-Kagome system $Cu_3Bi(SeO_3)_2O_2Br$. *Phys. Rev.* **2012**, *B86*, 174411. [CrossRef]
54. Pregelj, M.; Zaharko, O.; Zorko, A.; Gomilšek, M.; Sendetskyi, O.; Günther, A.; Ozerov, M.; Zvyagin, S.A.; Luetkens, H.; Baines, C.; et al. Controllable Broadband Absorption in the Mixed Phase of Metamagnets. *Adv. Funct. Mater.* **2015**, *25*, 3634–3640. [CrossRef]
55. Rousochatzakis, I.; Richter, J.; Zinke, R.; Tsirlin, A.A. Frustration and Dzyaloshinsky-Moriya anisotropy in the kagome francisites $Cu_3Bi(SeO_3)_2O_2X$ (X = Br, Cl). *Phys. Rev.* **2015**, *B91*, 024416. [CrossRef]
56. Zorko, A.; Gomilšek, M.; Pregelj, M.; Ozerov, M.; Zvyagin, S.A.; Ozarowski, A.; Tsurkan, V.; Loidl, A.; Zaharko, O. Electron spin resonance insight into broadband absorption of the $Cu_3Bi(SeO_3)_2O_2Br$ metamagnet. *AIP Adv.* **2016**, *6*, 056210. [CrossRef]
57. Wu, H.C.; Tseng, W.J.; Yang, P.Y.; Chandrasekhar, K.D.; Berger, H.; Yang, H.D. Anisotropic pressure effects on the Kagome $Cu_3Bi(SeO_3)_2O_2Cl$ metamagnet. *J. Phys. D Appl. Phys.* **2017**, *50*, 265002. [CrossRef]
58. Prishchenko, D.A.; Tsirlin, A.A.; Tsurkan, V.; Loidl, A.; Jesche, A.; Mazurenko, V.G. Antiferroelectric instability in the kagome francisites $Cu_3Bi(SeO_3)_2O_2X$ (X = Cl, Br). *Phys. Rev.* **2017**, *B95*, 0264102. [CrossRef]
59. Wu, H.C.; Chandrasekhar, K.D.; Yuan, J.K.; Huang, J.R.; Lin, J.-Y.; Berger, H.; Yang, H.D. Anisotropic spin-flip-induced multiferroic behavior in kagome $Cu_3Bi(SeO_3)_2O_2Cl$. *Phys. Rev.* **2017**, *B95*, 125121. [CrossRef]

60. Gnezdilov, V.; Pashkevich, Y.; Lemmens, P.; Kurnosov, V.; Berdonosov, P.; Dolgikh, V.; Kuznetsova, E.; Pryadun, V.; Zakharov, K.; Vasiliev, A. Lattice and magnetic instabilities in $Cu_3Bi(SeO_3)_2O_2X$ (X = Br, Cl). *Phys. Rev.* **2017**, *B96*, 115144. [CrossRef]
61. Constable, E.; Raymond, S.; Petit, S.; Ressouche, E.; Bourdarot, F.; Debray, J.; Josse, M.; Fabelo, O.; Berger, H.; de Brion, S.; et al. Magnetic and dielectric order in the kagome-like francisite $Cu_3Bi(SeO_3)_2O_2Cl$. *Phys. Rev.* **2017**, *B96*, 014413. [CrossRef]
62. Vergasova, L.P.; Semenova, T.F.; Shuvalov, R.R.; Filatov, S.K.; Anan'lyev, V.V. Ilinskite $NaCu_5O_2(SeO_3)_2Cl_3$—A new mineral of volcanic exhalations. *Trans. Russ. Acad. Sci.-Earth Sci. Sect.* **1997**, *353*, 641–644. (In Russian)
63. Badrtdinov, D.I.; Kuznetsova, E.S.; Verchenko, V.Y.; Berdonosov, P.S.; Dolgikh, V.A.; Mazurenko, V.V.; Tsirlin, A.A. Magnetism of coupled spin tetrahedra in ilinskite-type $KCu_5O_2(SeO_3)_2Cl_3$. *Sci. Rep.* **2018**, *8*, 2379. [CrossRef] [PubMed]
64. Charkin, D.O.; Kayukov, R.A.; Zagidullin, K.A.; Siidra, O.I. Chemical vapor transport and solid-state exchange synthesis of new copper selenite bromides. *Solid State Sci.* **2017**, *64*, 109–113. [CrossRef]
65. Kovrugin, V.M.; Colmont, M.; Mentré, O.; Siidra, O.I. Dimers of oxocentred $[OCu_4]^{6+}$ tetrahedra in two novel copper selenite chlorides, $K[Cu_3O](SeO_3)_2Cl$ and $Na_2[Cu_7O_2](SeO_3)_4Cl_4$, and related minerals and inorganic compounds. *Miner. Mag.* **2016**, *80*, 227–238. [CrossRef]
66. Becker, R.; Berger, H.; Johnsson, M. Monoclinic $Cu_3(SeO_3)_2Cl_2$: An oxohalide with an unusual CuO_4Cl trigonal–bipyramidal coordination. *Acta Cryst.* **2007**, *C63*, i4–i6. [CrossRef]
67. Krivovichev, S.V.; Shuvalov, R.R.; Semenova, T.F.; Filatov, S.K. Crystal chemistry of inorganic compounds based on chains of oxocentered tetrahedral III. Crystal structure of georgbokiite, $Cu_5O_2(SeO_3)_2Cl_2$. *Z. Kristallogr.* **1999**, *214*, 135–138. [CrossRef]
68. Galy, J.; Bonnet, J.J.; Andersson, S. The Crystal Structure of a New Oxide Chloride of Copper (II) and Selenium (IV): $Cu_5Se_2O_8Cl_2$. *Acta Chem. Scand.* **1979**, *A33*, 383–389. [CrossRef]
69. Krivovichev, S.V.; Filatov, S.K.; Burns, P.C.; Vergasova, L.P. The crystal structure of parageorgbokiite, β-$Cu_5O_2(SeO_3)_2Cl_2$. *Can. Miner.* **2007**, *45*, 929–934. [CrossRef]
70. Vergasova, L.P.; Semenova, T.F.; Krivovichev, S.V.; Filatov, S.K.; Zolotarev, A.A., Jr.; Ananiev, V.V. Nicksobolevite, $Cu_7(SeO_3)_2O_2Cl_6$, a new complex copper oxoselenite chloride from Tolbachik fumaroles, Kamchatka peninsula, Russia. *Eur. J. Mineral.* **2014**, *26*, 439–449. [CrossRef]
71. Krivovichev, S.V.; Filatov, S.K.; Semenova, T.F.; Rozhdestvenskaya, L.V. Crystal chemistry of inorganic compounds based on chains of oxocentered tetrahedral, I. Crystal structure of chloromenite, $Cu_9O_2(SeO_3)_4Cl_6$. *Z. Kristallogr.* **1998**, *213*, 645–649. [CrossRef]
72. Vergasova, L.; Krivovichev, S.; Semenova, T.; Filatov, S.; Ananiev, V. Chloromenite, $Cu_9O_2(SeO_3)_4Cl_6$, a new mineral from the Tolbachik volcano, Kamchatka, Russia. *Eur. J. Mineral.* **1999**, *11*, 119–123. [CrossRef]
73. Bastide, B.; Millet, P.; Johnsson, M.; Galy, J. Synthesis of copper(II) and selenium(IV) oxochlorides by chemical transport reaction: Crystal structure of $Cu_9O_2(SeO_3)_4Cl_6$. *Mater. Res. Bull.* **2000**, *35*, 847–855. [CrossRef]
74. Krivovichev, S.V.; Filatov, S.K.; Armbruster, T.; Pankratova, O.Y. Crystal Structure of $Cu(I)Cu(II)_4O(SeO_3)Cl_5$, a New Heterovalent Copper Compound. *Dokl. Chem.* **2004**, *399*, 226–228. [CrossRef]
75. Rabbani, F.; Svengren, H.; Zimmermann, I.; Hu, S.; Laine, T.; Hao, W.; Åkermark, B.; Åkermark, T.; Johnsson, M. Cobalt selenium oxohalides: Catalysts for water oxidation. *Dalton Trans.* **2014**, *43*, 3984–3989. [CrossRef] [PubMed]
76. Johnston, M.G.; Harrison, W.T.A. Barium cobalt chloride selenite, $Ba_2CoCl_2(SeO_3)_2$. *Acta Cryst.* **2002**, *E58*, i49–i51. [CrossRef]
77. Hu, S.; Johnsson, M. Synthesis and crystal structure of $Fe_6Ca_2(SeO_3)_9Cl_4$—A porous oxohalide. *Dalton Trans.* **2013**, *42*, 7859–7862. [CrossRef] [PubMed]
78. Hamida, M.B.; Wickleder, M.S. {$[CoCl_{2/2}O_{4/1}]$}-Dimere in der Kristallstruktur von $CoNd_{10}(SeO_3)_{12}Cl_8$. *Z. Kristallogr.* **2005**, *S22*, 141b.
79. Wickleder, M.S.; Hamida, M.B. $CoSm(SeO_3)_2Cl$, $CuGd(SeO_3)_2Cl$, $MnSm(SeO_3)_2Cl$, $CuGd_2(SeO_3)_4$ und $CuSm_2(SeO_3)_4$: Übergangsmetallhaltige Selenite von Samarium und Gadolinum. *Z. Anorg. Allg. Chem.* **2003**, *629*, 556–562. [CrossRef]
80. Krivovichev, S.V.; Filatov, S.K.; Burns, P.C.; Vergasova, L.P. The Crystal Structure of Allochalcoselite, $Cu^+Cu^{2+}{}_5PbO_2(SeO_3)_2Cl_5$, A Mineral With Well-Defined Cu^+ And Cu^{2+} Positions. *Can. Miner.* **2006**, *44*, 507–514. [CrossRef]

81. Burns, P.C.; Krivovichev, S.V.; Filatov, S.K. New Cu^{2+} coordination polyhedra in the crystal structure of burnsite, $KCdCu_7O_2(SeO_3)_2Cl_9$. *Can. Miner.* **2002**, *40*, 1587–1595. [CrossRef]
82. Shuvalov, R.R.; Vegasova, L.P.; Semenova, T.F.; Filatov, S.K.; Krivovichev, S.V.; Siidra, O.I.; Rudashevsky, N.S. Prewittite, $KPb_{1.5}Cu_6Zn(SeO_3)_2O_2Cl_{10}$, a new mineral from Tolbachik fumaroles, Kamchatka peninsula, Russia: Description and crystal structure. *Am. Miner.* **2013**, *98*, 463–469. [CrossRef]
83. Kovrugin, V.M.; Siidra, O.I.; Mentré, O.; Krivovichev, S.V. Structural variety of novel Pb and Bi selenites. *Acta Cryst.* **2013**, *A69*, s134. [CrossRef]
84. Kovrugin, V.M. Crystal Chemistry of Novel Oxide Compounds of Se4+ and Se6+ PhD Thesis Saint Petersburg 2015. Available online: https://disser.spbu.ru/files/phdspsu2015/Kovrugin.pdf (accessed on 3 April 2018).
85. Kovrugin, V.M.; Colmont, M.; Siidra, O.I.; Mentré, O.; Al-Shuray, A.; Gurzhiy, V.V.; Krivovichev, S.V. Oxocentered Cu (ii) lead selenite honeycomb lattices hosting Cu (i) Cl 2 groups obtained by chemical vapor transport reactions. *Chem. Commun.* **2015**, *51*, 9563–9566. [CrossRef] [PubMed]
86. Cao, X.-L.; Kong, F.; Hu, C.-L.; Xu, X.; Mao, J.-G. $Pb_4V_6O_{16}(SeO_3)_3(H_2O)$, $Pb_2VO_2(SeO_3)_2Cl$, and $PbVO_2(SeO_3)F$: New Lead(II)−Vanadium(V) Mixed-Metal Selenites Featuring Novel Anionic Skeletons. *Inorg. Chem.* **2014**, *53*, 8816–8824. [CrossRef] [PubMed]
87. Gemmi, M.; Campostrini, I.; Demartin, F.; Gorelik, T.E.; Gramaccioli, C.M. Structure of the new mineral sarrabusite, $Pb_5CuCl_4(SeO_3)_4$, solved by manual electrondiffraction tomography. *Acta Cryst.* **2012**, *B68*, 15–23. [CrossRef] [PubMed]
88. Vergasova, L.P.; Semenova, T.F.; Filatov, S.K.; Krivovichev, S.V.; Shuvalov, R.R.; Ananiev, V.V. Georgbokiite $Cu_5O_2(SeO_3)_2Cl_2$—A new mineral from volcanic sublimates. In *Doklady Earth Sciences*; Springer: Berlin/Heidelberg, Germany, 1999; Volume 364, pp. 527–531. (In Russian)
89. Semenova, T.F.; Rozhdestvenskaya, I.V.; Filatov, S.K.; Vergasova, L.P. Crystal Structure and Physical Properties of Sophiite, $Zn_2(SeO_3)Cl_2$, a New Mineral. *Miner. Mag.* **1992**, *56*, 241–245. [CrossRef]
90. Johnsson, M.; Törnroos, K.W. Zinc selenium oxochloride, b-$Zn_2(SeO_3)Cl_2$, a synthetic polymorph of the mineral sophiite. *Acta Cryst.* **2007**, *C63*, i34–i36. [CrossRef]
91. Akhrorov, A.Y.; Kuznetsova, E.S.; Aksenov, S.M.; Berdonosov, P.S.; Kuznetsov, A.N.; Dolgikh, V.A. Synthesis and crystal structure of $Fe[(Te_{1.5}Se_{0.5})O_5]Cl$, the first iron compound with selenate(IV) and tellurate(IV) groups. *Solid State Sci.* **2017**, *74*, 37–43. [CrossRef]
92. Pregelj, M.; Zaharko, O.; Zorko, A.; Kutnjak, Z.; Jeglič, P.; Brown, P.J.; Jagodič, M.; Jagličić, Z.; Berger, H.; Arčon, D. Spin Amplitude Modulation Driven Magnetoelectric Coupling in the New Multiferroic $FeTe_2O_5Br$. *Phys. Rev. Lett.* **2009**, *103*, 147202. [CrossRef] [PubMed]
93. Pregelj, M.; Zorko, A.; Zaharko, O.; Arčon, D.; Komelj, M.; Hillier, A.D.; Berger, H. Persistent Spin Dynamics Intrinsic to Amplitude-Modulated Long-Range Magnetic Order. *Phys. Rev. Lett.* **2012**, *109*, 227202. [CrossRef] [PubMed]
94. Zaharko, O.; Pregelj, M.; Arčon, D.; Brown, P.J.; Chernyshov, D.; Stuhr, U.; Berger, H. $FeTe_2O_5Br$ system: New ferroelectric with an incommensurate spin modulation. *J. Phys. Conf. Ser.* **2010**, *211*, 012002. [CrossRef]
95. Choi, K.-Y.; Choi, I.H.; Lemmens, P.; van Tol, J.; Berger, H. Magnetic, structural, and electronic properties of the multiferroic compound $FeTe_2O_5Br$ with geometrical frustration. *J. Phys. Condens. Matter* **2014**, *26*, 086001. [CrossRef] [PubMed]
96. Lafront, A.-M.; Bonvoisin, J.; Trombe, J.-C. Synthesis, Crystal Structure, and Magnetic Measurement of Two New Diselenites:$M_2(Se_2O_5)_3$ with M = Fe(III), Cr(III). *J. Solid State Chem.* **1996**, *122*, 130–138. [CrossRef]
97. Wildner, M. Crystal Structure of $Mn(II)Mn(III)_2O(SeO_3)_3$. *J. Solid State Chem.* **1994**, *113*, 252–256. [CrossRef]
98. Berdonosov, P.S.; Olenev, A.V.; Dolgikh, V.A. Lead (II) selenite halides $Pb_3(SeO_3)_2X_2$ (X = Br, I): Synthesis and crystal structure. *Crystallogr. Rep.* **2012**, *57*, 200–204. [CrossRef]

MDPI
St. Alban-Anlage 66
4052 Basel
Switzerland
Tel. +41 61 683 77 34
Fax +41 61 302 89 18
www.mdpi.com

Crystals Editorial Office
E-mail: crystals@mdpi.com
www.mdpi.com/journal/crystals

MDPI
St. Alban-Anlage 66
4052 Basel
Switzerland

Tel: +41 61 683 77 34
Fax: +41 61 302 89 18

www.mdpi.com

ISBN 978-3-03897-518-2